Direct Estimation of Strains at Carotid Artery Wall Using Autocorrelation of Ultrasound Images

A Thesis

SUBMITTED TO THE FACULTY OF THE

UNIVERSITY OF MINNESOTA

BY

Yasaman Adibi

IN PARTIAL FULLFILMENT OF THE REQUIREMENTS

FOR THE DEGREE OF

DOCTOR OF PHOLOSOPHY

NOVEMBER 1, 2015

Advisor: Professor Emad S. Ebbini

Dedication

To my mother and my sister for their unconditional love and support.

Abstract

Acute ischemic disorders such as myocardial infarction and stroke are the main cause of death in modern world. Therefore, methods to detect them early or evaluate their precursors would be of great importance. Change in arterial stiffness, or rigidity of the wall, is a very important risk factor in cardiovascular diseases. It is believed that stiffness abnormalities start to form before any apparent clinical indication of the disease. Having an efficient, noninvasive tool to measure arterial stiffness would be of great significance in prevention of arterial disorders such as atherosclerosis or determining their severity in patients.

Strain imaging is a promising tool for studying the characteristics of living tissue and has been around for over two decades. MR elastography (MRE) and ultrasound elastography are widely used on commercial scanners, but are far from reaching their full potential. The latter has a number of different implementations such as quasi-static, transient, shear wave, and acoustic radiation force impulse (ARFI). Most of these implementations rely on finding the displacement of tissue in 1D or 2D. In quasi-static elastography, spatial gradients of the axial displacement fields are computed to produce "elasticity maps", which are overlaid on anatomical B-mode images of the organ, e.g. breast. The quality of these maps depend on the displacement estimation method used and the measurement noise that could be amplified by gradient operators.

Displacement estimation plays key role in obtaining tissue elastic properties based on pulse-echo ultrasound. Speckle tracking is the most widely used technique for estimating displacement due to coherent nature of ultrasound. Recent advances of 2D speckle tracking

have enabled robust 2D displacement estimation with subsample resolution in both axial and lateral dimensions. Despite these advances, the need for filtered gradient operations for strain computation may limit the usefulness of strain mapping of fine tissue structures such as vessel walls.

In this research a new method for direct estimation of axial, lateral and shear strains in tissue is developed. This method takes advantage of local autocorrelation function and the relationship between autocorrelation and power spectral density of analytic radiofrequency (RF) signals. The method assumes sufficiently high frame rates to allow modeling of the frame-to-frame tissue displacement as an affine transformation.

In 2D analysis, this would be a Jacobian matrix of 4 elements each of them being one strain parameter. The theory is tested *in vivo* on posterior wall of common carotid artery of a healthy human subject, as well as *in vitro* for a vessel mimicking phantom. Results indicate better resolution and accuracy in all four strain parameters than correlation and gradient based techniques.

Besides strain, which is a determinant of stiffness of artery, there are other parameters that can independently contribute as a risk factor in cardiovascular diseases. In this research, pulse wave velocity (PWV) was measured and shown that, despite relatively small width of imaging plane and relatively low frame rates, PWV could still be derived from strain data with acceptable accuracy. Available pressure data also made it possible to measure wall shear rate (WSR) and wall shear stress (WSS), two indicators of deformation of flow and wall respectively.

Contents

Table of Figures

List of Tables

Chapter 1

Introduction

1.1 Motivation

Acute ischemic disorders such as myocardial infarction and stroke are the main cause of death in modern world [1]. Cardiovascular diseases (CVD) claim one life approximately every 40 seconds in the United States, which corresponds to 31.1% of all deaths [2]. According to the Centers for Disease Control and Prevention (CDC) statistics, heart disease, stroke and hypertension are among the leading causes of disability in the United States [2]. Among all CVDs, stroke has the highest mortality rate, killing almost 130,000 people in the United States each year [3].

Strokes are classified into two types, based on the damages to blood vessels. Ischemic stroke, which is the dominant type, is the result of occlusion in blood vessels, supplying brain oxygen due to thrombosis or atherosclerosis and incorporates about 87% of total strokes. The remaining 13% are hemorrhagic strokes, caused by rupture of weakened blood vessels, mainly aneurismal and arteriovenous vessels [4] [5].

1.2 Cardiovascular System

In order to survive, all body cells need oxygen and nutrients. They also need to remove their waste products before the poisonous byproducts destroy them. This function is effectively performed by an elegant cardiovascular system in human body. Heart muscle,

pumps about once every second and distributes oxygen bearing blood, via arteries in a large network. At the end of each heart cycle, the oxygen-less blood returns to the heart and the cycle repeats. Any blockage or occlusion in any part of vascular network can cause disturbance in blood circulation and affect the whole vascular system. In order for blood to flow, a pressure wave is generated by the heart and propagated through the entire arterial system. To allow the minimally attenuated propagation of the pulse wave, the vessel (arterial) walls are formed by unique elastic structure. The wall of arteries consists of three layers:

- **Intima**: the inner most layer, consisting of endothelial cells in direct contact with blood.
- **Media**: the mid-layer, containing smooth muscle cells (SMC). This layer, plays the key role in health and disease of the artery and formation of atherosclerotic plaques.
- **Adventitia**: the outermost layer, in direct contact with surrounding tissue, consisting mostly of collagenous fibers.

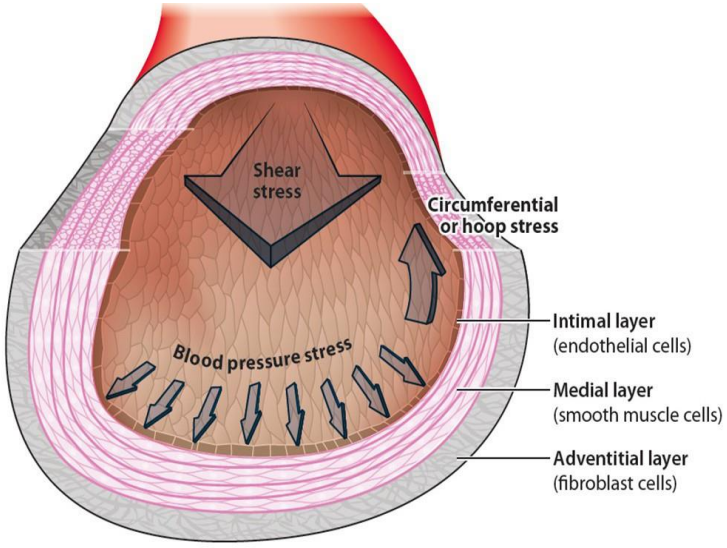

Figure (1.1) *three layers of Arterial Wall* [165]

Figure (1.1) shows different layers of an artery. Each layer consists of different cellular fibers.

1.3 Atherosclerosis

Atherosclerosis, is the process of hardening (increase in stiffness) and thickening of the wall of arteries and creation of plaques [6]. It is a systemic disease in the sense that although, it happens locally, affects the whole vascular system's function [7]. In fact, the change in arterial stiffness is a very important risk factor in cardiovascular diseases and is defined as change in rigidity of the wall of arteries. It is believed that arterial stiffening, starts long before any apparent clinical indication of the disease [8]. Atherosclerosis is known to form in regions of the vessel wall, where shear stress is lower than its nominal value, since wall stresses including tensile stress (i.e. the force along the direction of deformation), strongly effect hemodynamic environment. Subsequently, lower stress region represents lower blood flow and leads to accumulation of plaque forming material. Atherosclerosis is also associated with increase in blood pressure, which, increases loading on heart [9].

Atherosclerosis is a slowly progressing disease [10]. At the beginning of plaque formation, the intake of low density lipoprotein (LDL) at the wall increases [11]. This may lead to early onset of the disease, by formation of "fatty streaks", containing inflammatory cells, i.e. T-lymphocytes and macrophages [10]. The progression of this process, stimulates the attraction of smooth muscle cells, which add to inflammatory site. Therefore, a lesion is formed at that region, which results the thickening of wall. Based on components, plaques can be characterized as stable of vulnerable [11]. Vulnerable plaques are the cause of most fatal myocardial infarctions. They form a thin fibrous cap and large lipid content. This

renders them prone to rupture with the added risk of releasing emboli, which can occlude vessels downstream [12]. Figure (1.2), shows different stages of atherosclerosis and different plaque types.

Given the significance of stiffness in development of atherosclerosis, a robust noninvasive tool to measure arterial stiffness would be of great need in order to prevent or manage the disease [12].

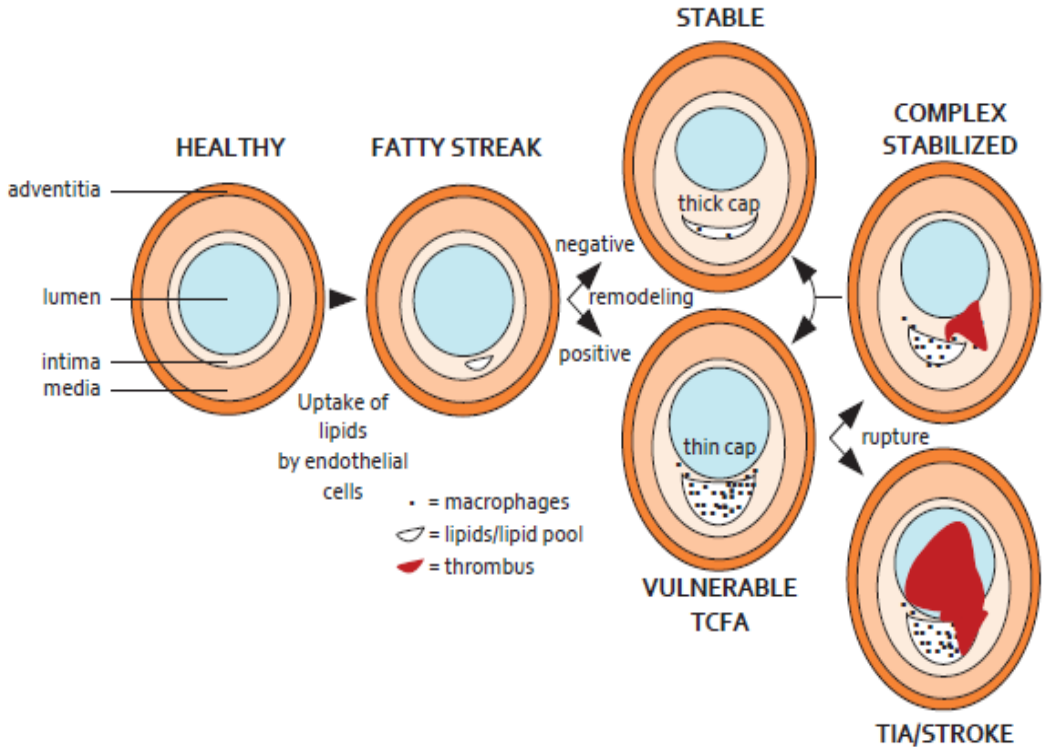

Figure (1.2) Overview of atherosclerosis progression and vulnerable plaque development. (Figure taken from *[176]*)
TCFA: Thin Cap Fibroatheroma TIA: Transient Ischemic Attack

1.4 Vascular Imaging

There are several invasive and noninvasive imaging modalities, used for visualizing the vascular system. These imaging modalities are capable of detecting abnormalities in the heart and vessels, such as different stages of atherosclerosis. In this section, we briefly review a few of them.

Computed Tomography (CT) angiography is a widely used imaging technique. In order to visualize the vascular system under ionizing radiation, a contrast agent (iodine based) is injected into blood stream. This imaging modality is capable of localizing the plaque and even determining the stage of disease [13]. Although CT is capable of determining the degree of calcification, it is not yet possible to determine the vulnerability of plaque with this imaging modality. Furthermore, to enhance the resolution, radiocontrast agents are injected into the blood stream. Although, the dosage of contrast agent follows certain restrictions, it can be potentially harmful to body due to its ionizing radiation effect [14].

Intravascular ultrasound (IVUS) is a catheter-based imaging technique in which the ultrasound probe is placed on the tip of a specialized catheter to provide cross sectional images (inner wall) of different vessels. Similar to CT it is capable of locating the plaque and determining the degree of stenosis. IVUS is especially used in regions where angiography cannot provide reliable results. However, this is an invasive imaging technique which may be considered as one of its disadvantages [15].

Magnetic Resonance Imaging (MRI) is also being widely used in imaging the cardiovascular system and atherosclerosis. Carotid artery plaques can be visualized using 1.5 to 3 T MRI. Some recent studies have shown that using high intensity field MRI of 7 T, the vulnerability of plaque can be measured as well. It is claimed that at this strength,

SNR is large enough to reveal the details of plaque composition. Despite MRI's capability to image carotid artery characteristics, imaging some deep arteries such as coronary arteries remains a challenge for this technique. Furthermore, MRI may not be cost effective as an imaging modality for frequent use [16] [17].

1.5 Medical Ultrasound

Ultrasound is an established and most widely used medical imaging modality. Its relative simplicity, portability, low operation cost, safety (no ionizing radiations needed) and feasibility of real-time data processing put it to advantage over many other imaging modalities such as CT and MRI [18].

Even though it was demonstrated in 1930s by Sokolov (1935, 1939) [19] [20], this imaging modality was not fully recognized until early fifties by Wild and Reid for their work on detecting breast tumors [20] [21] [22]. Since then tremendous advances in technology have made it possible to track much more sophisticated structures and the industry has evolved from static to real time imaging where all necessary data can be processed simultaneously and results are available to the user immediately.

Medical ultrasound devices typically work with frequencies above 1 MHz up to 50 MHz [23]. Higher central frequency of the device results higher lateral resolution and indirectly improves the axial resolution. However, this improvement in image quality, is obtained at the cost of lower penetration depth.

The principle of this imaging modality is based on transmitting and receiving acoustic waves by a transducer. Ultrasound is a coherent imaging modality, i.e. it works upon constructive and destructive interference of acoustic waves, scattered by tissue which cause

the granular appearance of images. The amount of reflection depends on acoustic impedance mismatch between different layers of tissue. Acoustic impedance can be defined in simple form as: $Z = \rho c$ where, ρ is the density of tissue and c is speed of sound in the medium. The impedance can change with frequency. Larger impedance mismatch between two media causes larger reflection. Reflections are seen as bright spots on ultrasound images.

What makes a specific ultrasound probe suitable for a certain application is usually the excitation frequency and the geometry of its elements within the aperture. In addition, there are different excitation schemes such as linear array and phased array modes. The former typically produces rectilinear image formats and is widely used in peripheral vascular imaging. The phased array format is used for small-aperture transducers such as transthoracic cardiac probes and produce sector image formats. Figure (1.3) shows typical probes used in medical applications.

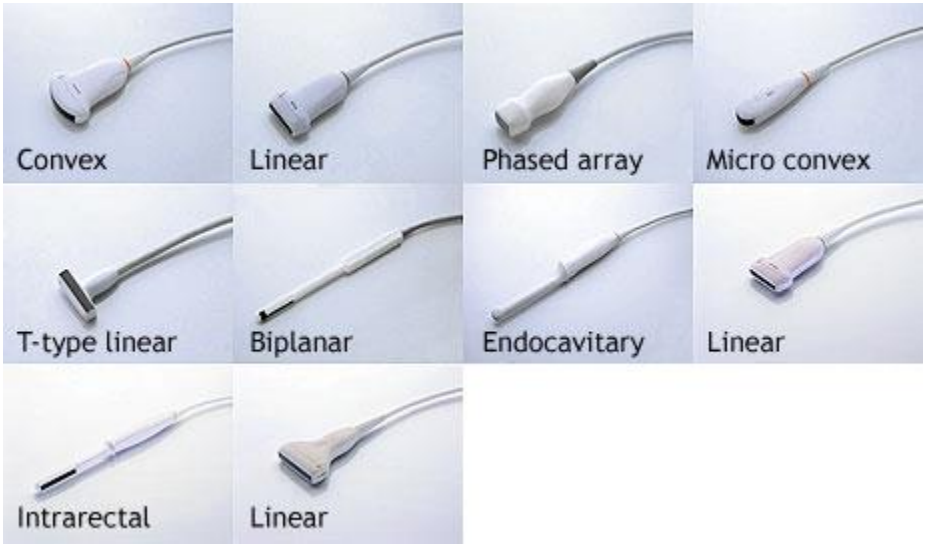

Figure (1.3) Most commonly used ultrasound probes (From Mindray Probes company) *[181]*

Several signal processing steps are performed on the raw received radio frequency (RF) data from transducer before the final output becomes available. These steps (very briefly) include:

(i) a band pass filter for suppressing low frequency artifacts and high frequency noise;

(ii) time gain compensation (TGC);

(iii) Hilbert transformation of raw data which adds virtual phase to it (I-Q demodulation); and

(iv) log compression of data, since the signal can have a large dynamic range in which case, small but varying values will not be visible in the image. Log compression will adjust the dynamic range and data will cover a larger range of values without losing smaller valued features.

The output is displayed in several different imaging modes. The simplest display form is called A-mode or Amplitude mode and consists of one single line of signal called A-line. A-line is displayed as a function of depth. Figure (1.4a) shows an example of carotid artery A-line image. Each A-line contains information of a single longitudinal location at different axial depths.

Carotid A-line demonstrates much higher amplitude at the walls of artery than inside the lumen and surrounding tissue, since acoustic impedance of connective tissue is known to be much higher than that of other tissues such as fat [24]. Vessel walls have much higher echogenicity relative to their surroundings [25]. Furthermore, due to high attenuation of sound wave in connective tissues, little signal can pass through them [26]. That explains why the amplitude of A-lines inside lumen is about 20dB lower than the surrounding walls.

B-mode or brightness mode produces a 2D image of adjacent A-lines presenting the intensity of received signal from each transducer element. Since simply assembling A-lines together will destroy the exact geometry of the features, to preserve the original geometry scan conversion must be applied [27]. Figure (1.4b) shows an example of B-mode image of carotid artery of a healthy human subject [28] [29].

In M-mode (motion mode) imaging, one single A-line is swept in time (repeated) at the same location and displayed as a function of depth and time. Figure (1.4c) shows an M-mode image of the same subject (carotid artery). Axial movement of upper and lower wall during three heart cycles, can be observed on this figure. Longitudinal movement however, cannot be seen due to lack of carrier and lower resolution in this direction.

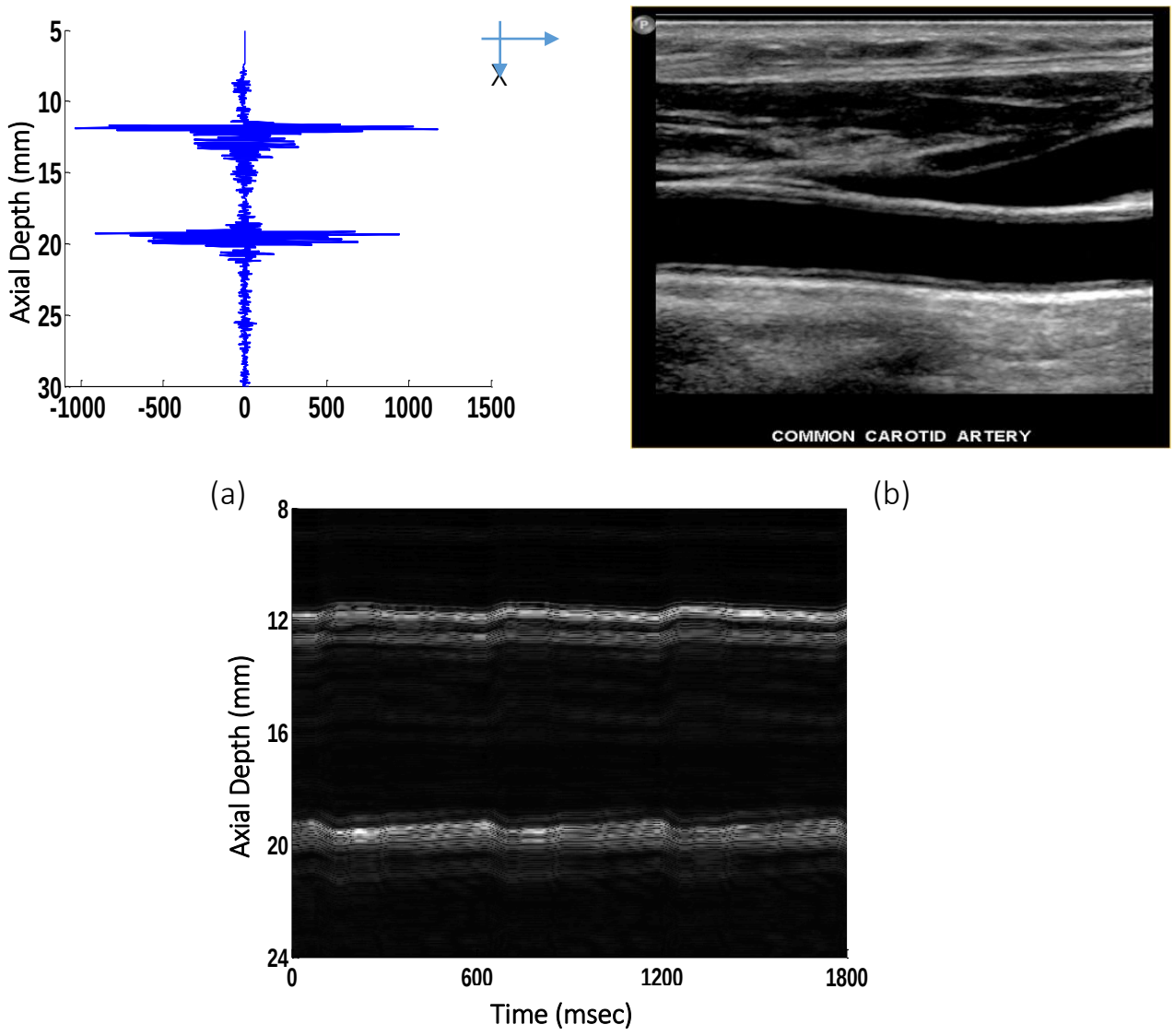

Figure (1.4) (a) A-Line image. (b) Longitudinal B-mode image [164] (c) M-mode image of Carotid Artery

1.6 Vascular Ultrasound

One of the early applications of medical ultrasound is in imaging large arteries in the arterial tree [30] [31] [32]. It is a practical tool for detecting abnormalities in the walls of large arteries such as carotid and femoral. Not only does ultrasound image the structure of the artery itself, it also captures any narrowing of the blood passage due to stenosis.

1.6.1 Doppler Ultrasound

In addition to imaging vessel walls, blood flow can also be measured using Doppler ultrasound techniques. Based on Doppler principle, the reflected signal from a moving target or source experiences a frequency shift, indicative of distance or relative velocity of the moving object. In case of stenosis, blood velocity can determine the severity of the blockage. There are several existing Doppler modes. The most commonly used are:

- **Color Doppler mode**: Mean component of central frequency is color-coded to visualize flow velocities and direction of flow. Basically, Doppler shifts are superimposed on a gray scale ultrasound. By convention red color shows the flow toward transducer while blue shows the opposite [33].

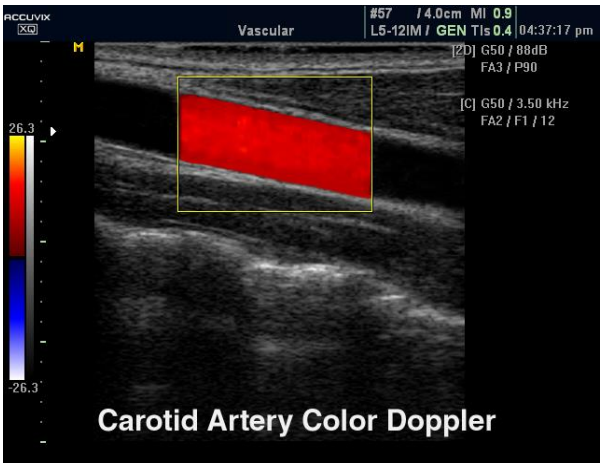

Figure (1.5) Color Flow Doppler of Carotid Artery. Red color shows the relative direction of blood flow to the transducer position (flowing toward the transducer) [29].

- **Power Doppler mode**: In this mode flow is color-coded based on power spectrum of Doppler signal. This Doppler mode is capable of detecting stenosis in the regions of vessel where flow is small. Sensitivity of this color mode is at least 3 times higher than conventional color Doppler (in terms of flow detection) [34].

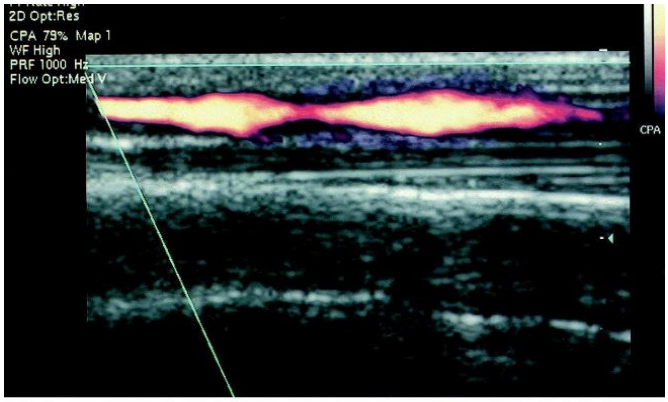

Figure (1.6): Longitudinal PD of a stenotic vein in hemodialysis fistula. (A) PD demonstrates an adequate visualization of the stenosis caused by intimal hyperplasia, as well as an accurate depiction of the residual intrastenotic lumen [172]

- **Pulsed Doppler**: In this Doppler mode, transducer acts as transmitter and receiver alternatively. It can work on very small segments (sample volumes) of the vessel, therefore can provide details in the imaging region. However, because of possibility of aliasing it is not able to detect very high velocities. This imaging mode can show the degree of impact of stenosis [35] [36].

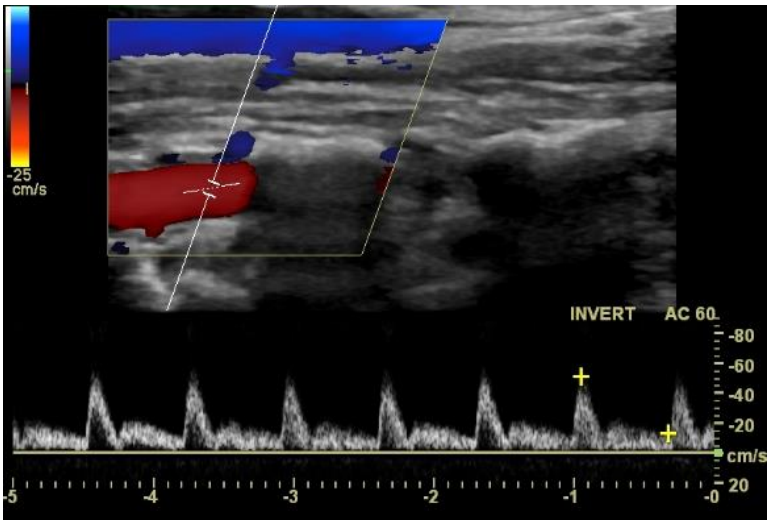

Figure (1.7) vertebral artery pulse wave Doppler. Note the direction of the flow in relation to the internal jugular vein (Image taken from [180])

1.6.2 Pulse Echo Technique

Pulse Echo ultrasound is the most widely used technique of imaging. It is the primary form of ultrasound imaging following the principles of radar. This technique became widely used in early 1970s. In pulse-echo (PE) ultrasound, short pulses (containing few cycles) are transmitted into the medium. Image is formed upon receiving the reflected wave by transmitting transducer. Specular reflection is due to impedance mismatch between different layers of tissue and is in part responsible in ultrasound image formation. The amount of reflection depends on the angle of incidence and impedance value. Small inhomogeneities in tissue, much smaller than the wavelength of ultrasound pulse, diffusely scatter echoes which are superimposed on the specular reflections to form the complete image [28].

1.6.3 Elasticity Measures

Measuring elastic parameters of the wall of arteries started with work of Arndt et al. in 1968 who measured the wall motion for human common carotid artery on A-mode ultrasound signals [37]. Since then, several methods have been proposed for measuring wall motion, which will be discussed in detail in chapter 2. Other than strain parameters which define elasticity of arterial wall, there are measures which can independently relate to stiffness (elastic characteristics) of the vessel. Each of these parameters can be independently used as an indicator of risk for arterial disorders such as atherosclerosis or degree of stenosis. A simple overview of these measures is as follows:

Global methods:

- **Pulse Pressure (PP)**: is the simplest measure of arterial stiffness. PP is the difference between systolic and diastolic pressures in one heart cycle. It is a representative of the

force that heart has to bear by each contraction and is proportional to stroke volume i.e. the amount of blood pumped out of left ventricle (LV) in each cycle. Therefore, any change in its normal value can be indicative of change of stiffness in arteries. As an example, increase in PP maybe caused by stiffness in aorta or other large arteries [38].

- **Pulse Wave Velocity (PWV)**: is the velocity of pressure wave propagating along the arterial tree caused by pumping of the heart. PWV is a measure of stiffness of arteries [39]. The gold standard for measuring PWV is finding the time delay for the foot of the wave to travel between femoral and carotid artery. However, this method provides a global measure. Arterial stiffness (atherosclerosis) causes an increase in PWV.
- **Augmentation Index (AIx)**: is calculated based on systolic aortic pressure [40] and is a measure of reflection of pulse wave and arterial stiffness. AIx is the "change in pressure after the first systolic notch to the peak aortic pressure" [41].

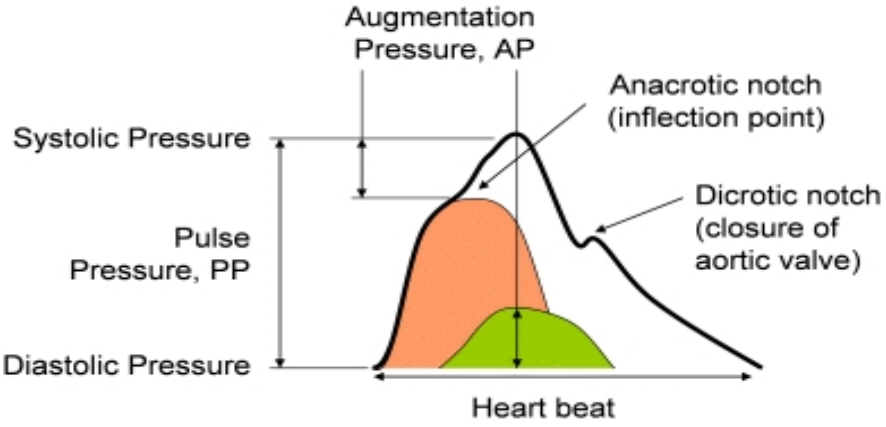

Figure (2.8) One method for calculating Augmentation Index *[182]*.

Local Methods:

- **Carotid Intima-Media thickness (cIMT)**: The thickness of intima + media in carotid artery is a measure to determine stiffness of the artery. Physicians determine the "age" of artery by measuring IMT. Any change in IMT can be associated with variations in stiffness. Increase in IMT is one of the signs of arterial stiffness. Subtle changes in thickness can be indicator of early onset of atherosclerosis [42].
- **Compliance**: is the ratio of volume change to change of pressure. In other words, it is the ability of vessel to expand and increase volume during increase of blood pressure. In arterial stiffness this ability decreases which results a decrease in diastolic pressure and increase in systolic pressure [43] [44].
- **Distensibility**: Distensibility Coefficient $DC = \frac{2\Delta d/d_s}{\Delta p}$ where Δd is the change in diameter, d_s is diameter during systole and Δp is the difference between average systolic and diastolic blood pressures. Similar to compliance the increase in distensibility also means increase in PWV and blood pressure [43] [45].
- **Stiffness index (β)**: $\beta = \ln(p_s/p_d)\frac{d_d}{\Delta d}$ where d_d is the diastolic diameter and Δd is the difference between systolic and diastolic diameter.
- **Young's Modulus (E)**: or elastic modulus shows material stiffness and is a measure of linear elasticity in solids. According to definition it is the ratio of stress (force per unit area) to strain in the same direction. For estimating Young's modulus knowledge of wall thickness is necessary. $E = \frac{d_d}{2h}.\frac{(p_s - p_d)}{(d_s - d_d)/d_d}$ where h is the wall thickness. p_s is the systolic and p_d is the diastolic pressure [46].

1.7 Elastography

Palpation is one of the earliest methods of diagnosing diseases has been around for more than three thousand years. Ebers papyrus from ancient Egypt reveals that palpation of pulse and abdomen were especially important in initial examination and diagnosis [47]. In modern medicine, palpation gained recognition in 1930s and became a tool in preliminary examinations [48] [49].

Large tumors or organ anomalies are stiffer than the surrounding tissue. It has been known for long that diseased tissue feels different under touch. The relative difference (stiffness) maybe recognizable by little pressure applied by hand. This method lacks the sensitivity in cases where the lesion is deep. It may also lack the specificity to distinguish between diseased and healthy tissue in the early stages of disease.

Being able to attribute values and quantities to stiffness (resistance to deformation) can significantly change the realm of prognosis of a large variety of disorders. Stiffness, along with several other mechanical properties of tissues (e.g. elastic moduli) are known to be independent risk indicators for several life threatening disorders [50] [51] [52].

Strain imaging or elastography is an imaging technique which maps tissue stiffness in all directions. However, the term *elastography* was first used in 1991 by Ophir et al. To demonstrate their quasi static method, they used 1D cross correlation-based technique to find axial strain in a foam block (phantom) and tissue *in vitro* [53]. In their experiment different strain values corresponded to levels of stiffness, e.g. low strain value was indicative of high stiffness in the region.

Several techniques have been developed to obtain elastography images and to improve the initial method. Ophir et al. used quasi-static elastography method, i.e. they applied a

controlled axial stress (external force) on the phantom and compared pre and post compression ultrasound images using cross correlation of A-lines in both frames. Figure (1.9) shows the result of cross correlation between pre and post compression signals. The displacement results were used to estimate local mechanical properties of the phantom.

In order to improve their method, Cespedes et al. tried subsample estimation to overcome the problem of decorrelation and data quantization [54]. Furthermore, in 1996 Varghese et al. came up with a method to reduce decorrelation noise in elastography, by temporal stretching (global stretching) of the post compression echo data to reduce errors between pre and post compression frames. In other words they built a strain filter [55] [56]. Later on, some groups (Alam 1998 and Srinivasan 2002) found algorithms to pick up the optimized local stretching factors to match with local tissue changes which allowed for reduction in strain noise [57] [58].

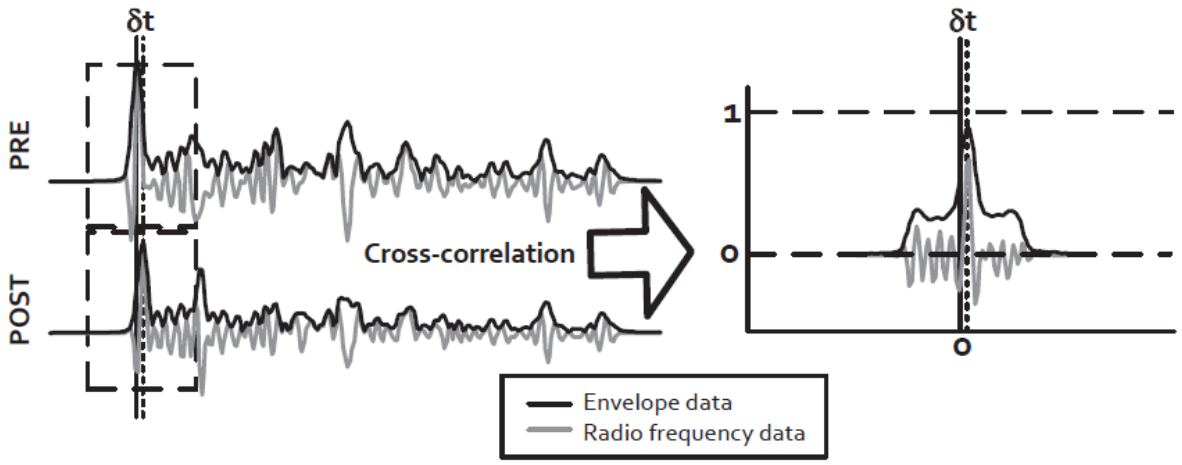

Figure (1.9) Cross Correlation of Pre and Post compression ultrasound signals (and their envelopes). Cross correlation reaches its maximum at the delay (displacement) instead of origin *[176]*.

Frequency domain analysis can be utilized as well as time domain analysis for obtaining similar results in elastography. Elastography deals with compression and expansion of tissue (in time/space domain). Applying Fourier transform and its scaling property, compression and expansion will be reversed. This property allows for cross correlation in spectral domain between pre and post deformed data, resulting the shift (displacement) between them [59] [60].

Several groups have already applied quasi-static elastogrpahy principles to estimate local properties of tissue types, including breast tissue, for early diagnosis of cancer using different approaches for solving the displacement problem [61] [62] [63].

There are several examples of using this method of elastography for detecting material moduli, of which we point out one of them here. Solving a system of linear equations for spatial derivatives of relative shear modulus, Sumi et al. (1995) obtained the relative shear modulus of soft tissue by integration [64]. They later improved their method using an iterative phase matching method for 2D displacement (1999) [65].

In quasi-static elastography, an external force has to be applied to the object to induce compression (stress/strain). However, compression doesn't always need to be applied externally. For example, Konofagou et al. (2007, 2008) made use of natural heart beat and the resulting pressure wave through the arterial tree to estimate local properties of myocardium and other parts of cardiovascular system [66] [67].

Another method for internal excitation is shear wave elastography (SWE) (originally proposed by Sarvazyan et al. [68]). In this method, shear waves are studied to assess

stiffness of tissue in different directions and get quantitative results. The higher the shear wave speed the higher the stiffness of tissue [69]. SWE is being clinically used for applications such as diagnosing liver cirrhosis. This noninvasive method of examining liver stiffness has already been given the brand name of "Fibroscan" [70] [71].

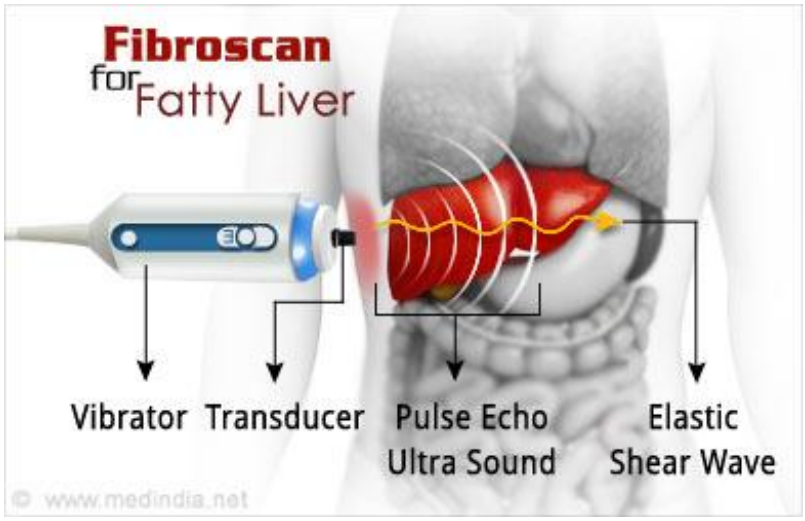

Figure (1.10) Schematic of FibroScan Probe. Figure is taken from *[177]*

Acoustic

radiation force impulse (ARFI) imaging is a special case of SWE in which, high intensity ultrasound pulses make localized displacement in tissue by transferring energy to it [72]. Elastic parameters in direction of the beam (axial direction) are measured in this method. ARFI is capable of producing a qualitative map of relative differences in stiffness in different regions

For *in vivo* imaging and displacement tracking, internal excitations are preferable to external ones because there is not a lot of control on the movement of the organ inside the body. Regardless of method or imaging modality used in elastography, basic steps are common in all of them:

- A mechanical force (internal or external) is applied to the tissue; Imaging is done pre and post compression;
- Displacements (1D, 2D or 3D) are estimated, using different methods.
- Elasticity related parameters are computed from displacements.

In most elastography methods, finding displacement between non-deformed and deformed tissue plays the key role in finding elastic properties.

Any elastic quantities are then, result of some operation on displacements. Normal and shear strains are the result of spatial derivatives of axial and longitudinal displacements. Gradient is known to be a noise amplifying operator [73] [74]. Large noise can completely mask small values of strain and degrade the accuracy of estimation significantly. Besides, change in strain values at the early stages of abnormality is not large and in order to be able to recognize the small changes an accurate estimation method is necessary.

1.8 Vascular Elastography

Elastography is widely used in determining vessel wall properties and diagnosing disorders such as atherosclerosis. The principles of elastography apply to obtain any abnormality (stiffness) on the wall of arteries or veins. Furthermore, ultrasound imaging modes have been in use in vascular elastography to detect abnormalities in the vessels. The use of ultrasound for detection of elastic characteristics of vascular system dates back to 1970s. During this time, elastic modulus of aorta was detected using a catheter based ultrasound system [75]. Intravascular ultrasound (IVUS) was then used to visualize inside the lumen and endothelial cells to find vulnerable plaques of coronary artery [76].

However, noninvasive application of ultrasound for vascular elastography started in 1980s. In 1985 Hoeks et al. used transcutaneous Doppler to measure diameter of carotid artery [77].

Dutta et al. (2013) used noninvasive ultrasound on engineered wall structures to measure Young's modulus, which correlated well with direct mechanical testing. They used a displacement tracking method to find the displacements. Therefore, mechanical properties of the engineered tissue were estimated. This method is yet to be tested *in vivo* [78].

Shear Wave Elastography is mainly used for elasticity imaging in organs like liver. More recently, however, studies to demonstarte feasibility of this method in diagnosis of stiffness of arteries have been published. The first group working on feasibility study were Coude et al. who showed the use of SWE in a vessel mimicking phantom and *in vivo*. According to their conclusion it is possible to use this method in clinical applications involving arterial stiffness. It would be especially efficient in detecting vulnerable plaques [79]. In 2013 Balahonova et al. used SWE to investigate the elastic properties of carotid arterial wall. Their method showed poor reproducibility [80]. However, in 2014 Ramnarine et al. showed its feasibility and potential for clinical applications. They measured Young's modulus on the vessel wall and in atherosclerotic plaque [81].

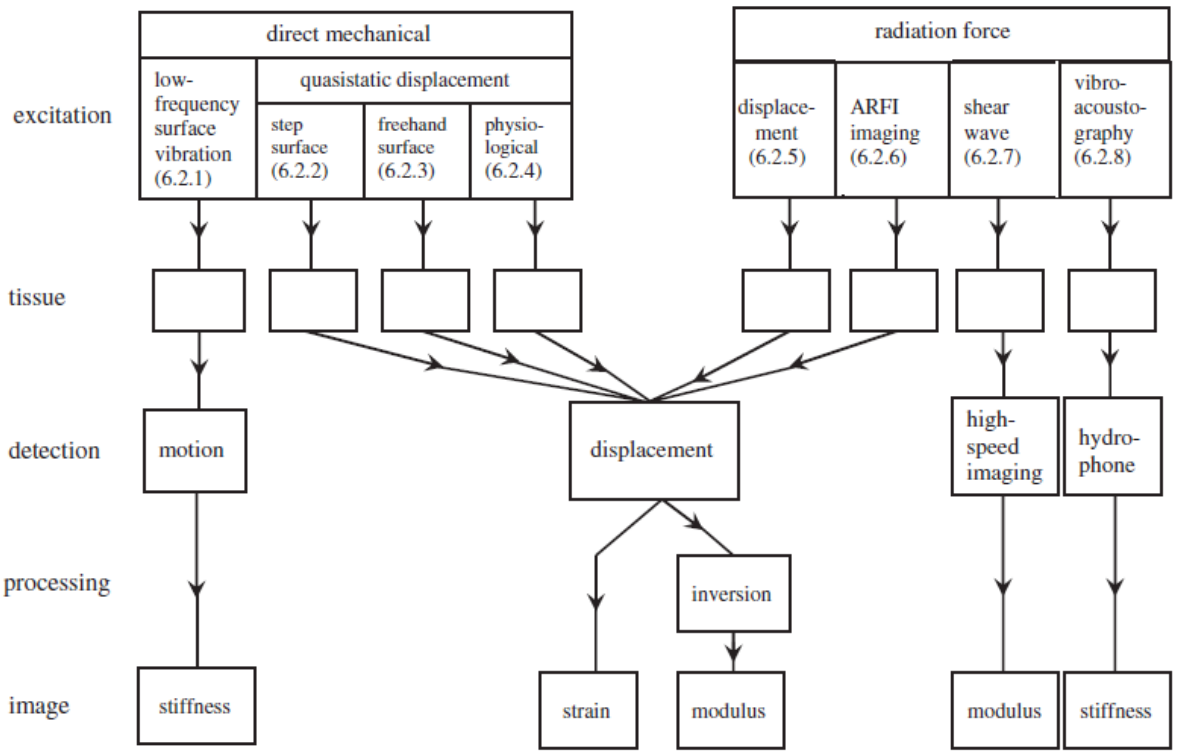

Figure (1.11) Different Elastography approaches, which includes the methods of excitation either mechanical or by radiation, external or internal. Figure is taken from *[49]*.

1.9 Contributions of This Research

In this dissertation, we investigate a new method to directly estimate strain parameters of the walls of carotid artery. Although the target is carotid artery wall, the application of our developed method can be generalized to different biological tissues and therefore to find tissue malignancies such as breast tumors.

B-mode imaging for carotid artery has been around for a few decades and is used as a diagnostic tool for atherosclerotic plaques [30] [31]. Since ultrasound image is formed from a combination of scatterings due to small inhomogeneities in tissue and specular reflection of echoes from interaction of waves at the surface of tissue, any change in elastic properties of the tissue should be observable [28]. However, due to presence of known artifacts in ultrasound images some inhomogeneities may not be clearly visible and some might be accounted for as artifacts [32]. Consequently, although B-mode images are commonly used to estimate the extent of plaques within the artery, similar to any other existing imaging modality, the vulnerability of plaques cannot be determined form them.

In more recent years contrast enhanced ultrasound and other advances in hardware have made it possible to provide better quality images in which the vascular network related to plaques can also be visualized.

Nevertheless, knowledge of stiffness of a plaque accurately will be extremely helpful in proper and efficient treatment. Normal and shear strains at the arterial wall determine the local stiffness but estimating the stiffness is not limited to strains.

All studies regarding strains of the arterial wall have assumed equal shear strains in axial and lateral directions based on incompressibility of tissue and estimated lateral shear for both parameters. However, tissue structure is very complicated and therefore not fully

incompressible. Vessel walls are also known to have anisotropic elastic properties. In this study we have been able to estimate axial and lateral shear strains separately without the need to invoke the incompressibility condition in the optimization problem. The resulting values for two strains are not the same. Therefore, estimating them separately will yield a more realistic view of the deformations occurring at a segment of vessel wall. Furthermore, studying axial (vertical) shear strain may enlighten new aspects of stiffness measurement.

Our 2D measurements have resulted pointwise information on strains. In other words, we have estimated local deformations at small segments of vessel walls as small as 0.29 mm laterally and 0.019 mm axially.

Small changes in stiffness at the walls of arteries can be a strong indicator for the onset of cardiovascular disorders. However, limited resolution of imaging modalities do not allow for detection of small changes. We have been able to detect strains as small as 0.1% with good accuracy without any further smoothing or interpolation of data. This accuracy has been achieved in all strain components.

Localization is another feature of this method. Relatively small kernel size (0.81mm x 0.87 mm in axial and lateral directions respectively) makes it possible to capture small changes or deformations and therefore, achieve subpixel resolution.

The principles used for the algorithm are based on a simple linear transformation between two autocorrelation functions. The simplicity of algorithm makes it possible to avoid the costly computations and facilitates the use of method in real time systems.

Other measures such as intima-media thickness (IMT), pulse wave velocity (PWV), arterial distensibility and β-stiffness are also among parameters expressing the stiffness.

PWV is a reliable measure for the risk factor in cardiovascular diseases. Velocity measurement is typically done by computing the time it takes for the pressure wave to travel from one point of the arterial wall to the other. These two points are usually located on common carotid and femoral artery. Among simplifying assumptions for computing velocity, one is that arterial tree is straight along the body which is not true in reality [82]. We show that mean PWV can be computed from strain parameters without the need for two separate measurements. Furthermore, localization of this method can also provide the ability to measure PWV locally. Small changes in PWV along small segments of the arterial wall can be a strong marker of changes in homogeneity and therefore the possibility of atherosclerosis.

1.10 Organization of This Thesis

This dissertation consists of six chapters. A general overview of medical ultrasound accompanied by a brief history of evolution of techniques in the area of carotid artery elastography was presented in this chapter. Our contributions were also pointed out.

Chapter 2 overviews displacement tracking (speckle tracking) principles and its existing techniques for carotid artery walls and generally for soft tissue. Speckle tracking as the most widely used technique for finding displacement is described in details; different mathematical concepts involved in the technique are explained and cross correlation issues are pointed out.

Chapter 3 introduces our new method. Mathematical theories supporting the method are stated and step by step algorithm demonstrated in detail. The novelty of method is discussed and its advantages over existing techniques for estimating strain parameters are

pointed out. Mathematical basics of this method such as affine transformation and duality between spatial cross correlation function and power spectral density through the Fourier transform is illustrated. Some other properties of Fourier transform used in the method are also explained.

In chapter 4 we provide the *in vivo* and *in vitro* experiment setups and demonstrate different stages of experiments in detail. The new method's achievement is illustrated through discussing the results.

In chapter 5 a few elasticity related parameters, used in characterizing the risk factors for cardiovascular diseases are introduced. These factors include pulse wave velocity (PWV), wall shear rate (WSR) and wall shear stress (WSS).

Chapter 6 concludes the presented research and suggests future potentials for improvement and applications of our introduced method.

Chapter 2

Speckle Tracking

2.1 Introduction

It was pointed out in chapter 1 that Ophir et.al (1991) were the first group to use elastography to estimate elastic properties of a foam block phantom [53]. The three general steps of elastography were also briefly overviewed in section 1.3. In this research we investigated a new method in which strain parameters were not computed by derivatives of displacements but directly based on characteristics of autocorrelation function. However, displacement tracking still remains the most widely used method in motion related medical ultrasound applications especially those involving elastography.

Other than strain imaging, displacement tracking is utilized in many other applications such as studying the muscle activity or functional activities of body [83] [84]. It is also used in therapeutic ultrasound for the purpose of imaging the temperature [85] [86] [87].

Since most existing strain imaging techniques are based on frame to frame displacement of scatterers, in this chapter we will focus on displacement tracking methods using ultrasound. The difference in strain estimation methods is usually a consequence of difference in techniques used for displacement tracking. In this thesis the terms “speckle tracking” and “displacement tracking” are used as synonymous and will be referred to as

one or other for convenience. However, displacement tracking is a very general term used in all fields of engineering and science. Whereas, speckle tracking relates to imaging modalities (coherent) in which speckle pattern is produced.

Before starting the discussion of displacement tracking we will first briefly explain the nature of speckle and how it can be used in imaging applications. We will then review principles of speckle tracking methods in detail.

2.2 Speckle

Ultrasound images are formed by constructive and destructive interference of reflecting waves from different surfaces [28] and tend to have a granular appearance. Since tissue doesn't have a flat surface, wave can be reflected in all directions. However, ultrasound wavelength (which is in the order of 10^{-4} meters or tenth of millimeters) is much larger than the size of those reflecting structures (scatterers). These surface structures are the origin of speckles therefore, the granular appearance of ultrasound image is called speckle pattern. The granules usually are equal in size to the resolution of transducer in both dimensions [88] [89]. In other words, speckle is an inherent artifact of ultrasound images [90]. Speckle patterns in the imaging objects are quite stable provided there are no large deformations, i.e. although they seem to have a random distribution, they show identical behavior in repeated ultrasound imaging of the same object at the same physical and transducer conditions. Scatterers despite of being distributed randomly follow a certain statistical distribution. If there are large number of scatterers in the medium they will have a Rayleigh distribution [91]. In this situation speckles are called fully developed. Besides

that, shape of speckle is determined by the point spread function (PSF) of ultrasound system.

$$P(A) = \frac{A}{\varphi} \exp\left(-\frac{A^2}{2\varphi}\right) \qquad (2.1)$$

Equation (2.1) shows the Rayleigh distribution where A is the amplitude and φ is a constant [89].

In several ultrasound applications the effort is to eliminate speckles as they are considered as noise in the image. They can mask low amplitude features. However, since speckle patterns follow the tissue motion precisely, their movement from frame to frame can be detected and considered as displacement or deformation of tissue locally [92] [93] [94]. Therefore, existence of suitable amount of speckles in the image will be beneficial.

2.3 Speckle Tracking

The most widely used displacement detection method in coherent imaging modalities is speckle tracking. During the past two decades, numerous speckle tracking methods have been proposed and put to use in different applications. The idea of using speckles in ultrasound images for tracking purposes was first introduced by Robinson et al. (1982) [95] and later followed by Akiyama et al. (1986) [96] and Trahey et al. (1987) [97]. These methods can be generally classified in two groups: registration based methods (non-rigid registration) and block matching methods [98].

Registration based methods use image warping techniques. Basis functions such as B-splines are applied to parametrize the deformation field. Usually a regularization step

follows at the end of computations to optimize the cost function [99]. These methods are typically used to estimate motion and strain in myocardium.

In 2001 Ledesma-Carbayo et al. eliminated the need for image segmentation by using a global pixel-based matching criterion. They validated their method on simulated and in vivo data of healthy and pathological volunteers [100]. Utilizing local phase information in addition to intensity of ultrasound images Woo et al. (2009) found deformation in synthetic data as well as *in vivo* cardiac data of human and mouse by non-rigid registration. This method showed high resolution and SNR [101].

In block matching methods similar local image blocks are detected in a frame sequence. Speckle tracking (block matching) methods are robust and stable to the degree that are already being used in several commercial ultrasound devices. As an example EcoPAC software developed by GE Healthcare is capable of detecting a full sequence of one cycle of myocardial motion in about 5 to 10 seconds among other tasks. It can detect motion within a predefined region using speckle tracking [102] [103] [104].

Among block matching methods those based on cross correlation are the most common. Early on, during the development of these methods 1D cross correlation would provide displacement in axial (parallel to beam) direction [105] [106] [107]. Later on, advances in technology made higher frame rate imaging possible [108] [109]. This made lateral motion (perpendicular to the beam) detection possible. Therefore, 2D cross correlation would yield both displacements.

Two image frames are divided into small windows. Using cross correlation, the most relevant window in the post deformed frame will be detected. If motion is only comprised

of small lateral and axial movements a search algorithm should be able to find the corresponding window in the second frame. By sliding one window against the other one, cross correlation is computed. It will reach its maximum when all similar features overlap. The amount of axial and lateral lags in peak of cross correlation will determine the displacement [110]. Available methods are capable of detecting displacements with subsample resolution.

2.4 Cross Correlation

Cross correlation is a similarity measure used in almost all fields of science mainly for finding smaller features in a large feature.

Ultrasound has vastly taken advantage of this measure in detection of displacement between image frames. In case of full similarity between two frames the peak of cross correlation will be at the origin and the function would be an autocorrelation. However, if there are displacements between features of two images the peak will also shift equivalent to the amount of shift between two images. In ultrasound applications it is preferred to use normalized cross correlation.

Normalized cross correlation in 2D can be generally shown as:

$$CC = \frac{\sum_i \sum_j f_1(x,z) f_2^*(x-i, z-j)}{\sqrt{\sum_i \sum_j f_1(x,z) f_1^*(x-i, z-j)} \sqrt{\sum_i \sum_j f_2(x,z) f_2^*(x-i, z-j)}},$$

$$i \in \left[-\frac{w_x}{2} \frac{w_x}{2}\right], j \in [-\frac{w_z}{2}, \frac{w_z}{2}] \qquad (2,1)$$

Where w_x and w_z are the lengths of kernels in lateral and axial directions respectively. f_1 and f_2 are the pre and post deformation frames. Also * shows the complex conjugate of the

frame. This is a complex cross correlation since RF data is already Hilbert transformed to introduce phase to real values. Choice of kernel size is very important. The larger the correlation widow the higher the precision of estimated displacements. However, as the kernel size increases the spatial resolution will be degraded. Meanwhile, large time lag between frames will cause decorrelation, i.e. the same speckle pattern cannot be captured in second frame. Therefore, images at highest possible frame rate are desired.

One major application of cross correlation based speckle tracking is to measure wall motion in arteries. Blood flow and pressure wave along the arterial tree cause deformations along the wall of arteries. As a simplifying assumption these deformations can be considered as a combination of axial and lateral displacements on the wall.

Theoretically maximum value for cross correlation should reach 1. So displacement tracking would be the task of finding the axial and lateral lags at which correlation is 1. However, maximum value cross correlation is not always fixed at 1. Sampling the data (quantization) is one reason. Maximum may be lying between two pixels, in which case to find it, interpolation would be necessary. Furthermore, as mentioned large time lags or large displacements can also cause decorrelation. Largest displacements occur almost at the beginning of systole where vessel wall is going under largest stress. This can cause decorrelation between two frames. Therefore, at the same time instances maximum cross correlation would drop from its nominal value. Figure (2.1) shows the changes in maximum cross correlation with diameter during 3 heart cycles.

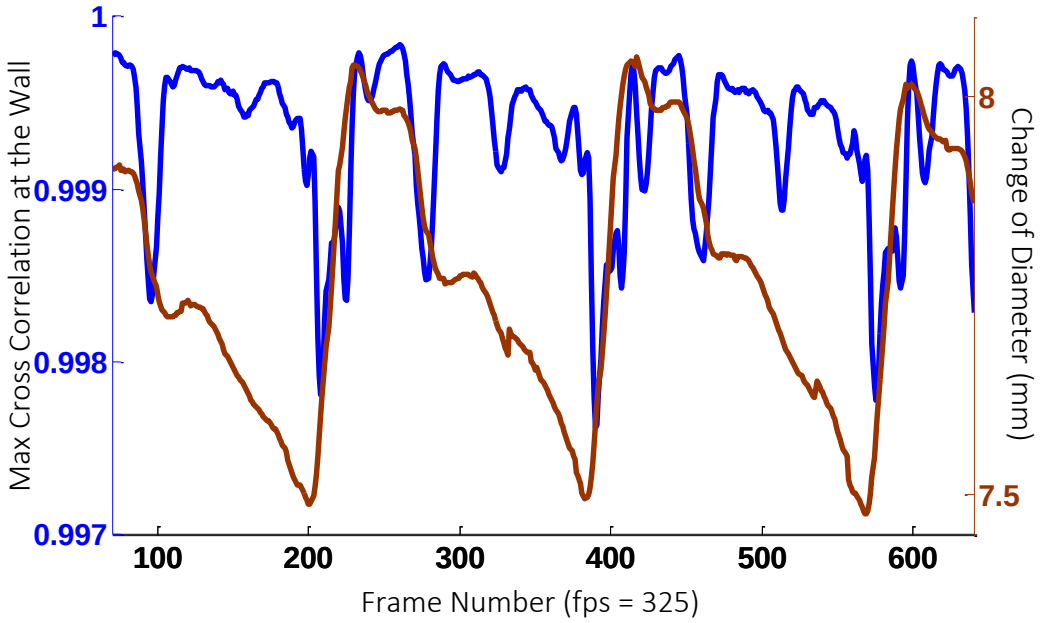

Figure (2.1) Variation of Max value for cross correlation and Diameter at the wall of Carotid Artery during three heart cycles

Meanwhile, large displacement at the wall indicates large strain. We hypothesize that largest strains also occur approximately at the same time (during systolic blood pressure rise) during the heart cycle. This means that at largest strain values we expect the largest drops in maximum cross correlation. Figure (2.2) shows the proof of consistency of strain results with maximum correlation. All strain parameters show the largest rise around beginning of pressure rise in systole.

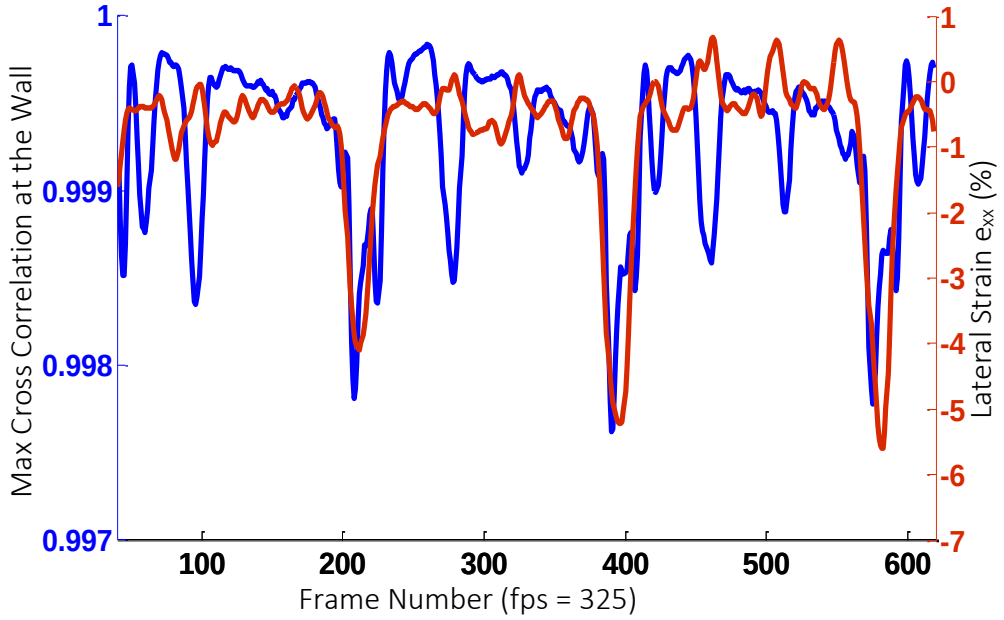

Figure (2.2) a) Variation of Max value for cross correlation and Lateral Strain at the Wall of Carotid Artery

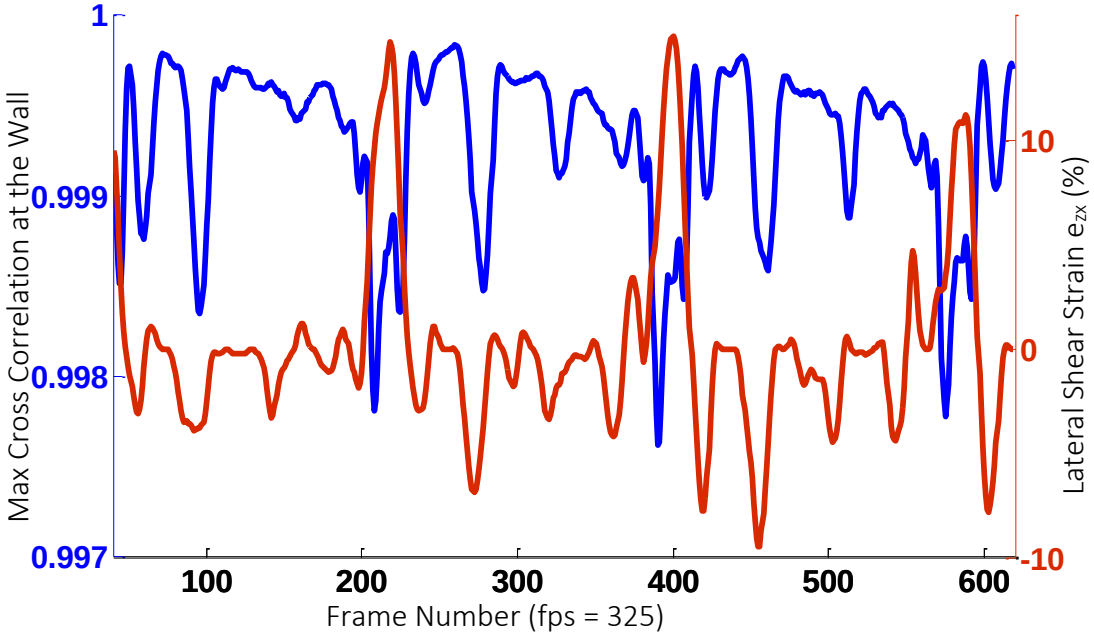

Figure (2.2) c) Variation of Max value for cross correlation and Lateral Shear Strain at the Wall of Carotid Artery

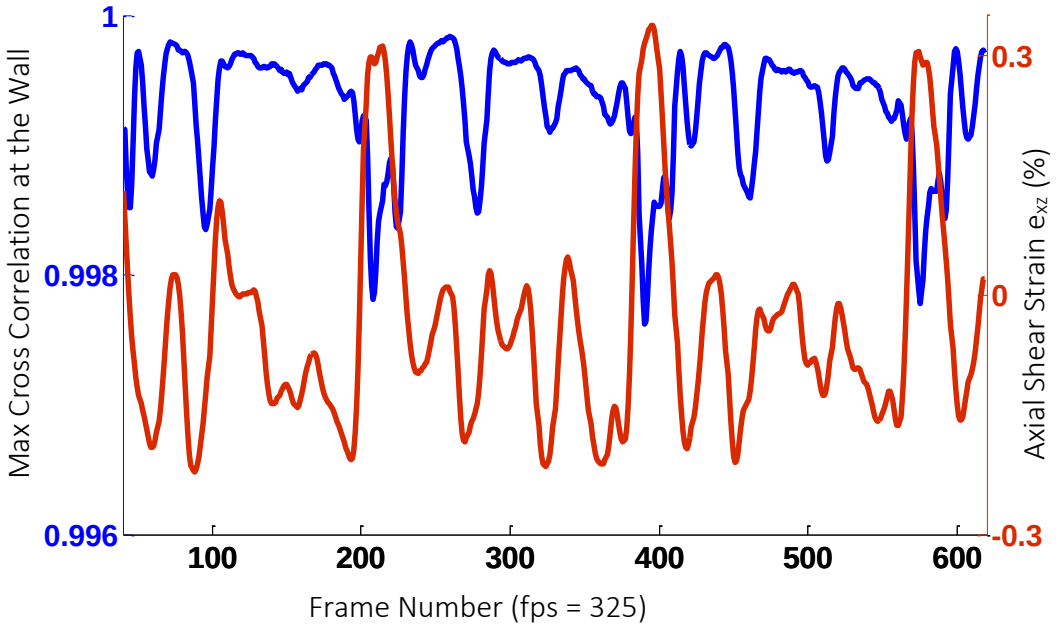

Figure (2.2) b) Variation of Max value for cross correlation and Axial Shear Strain at the Wall of Carotid Artery

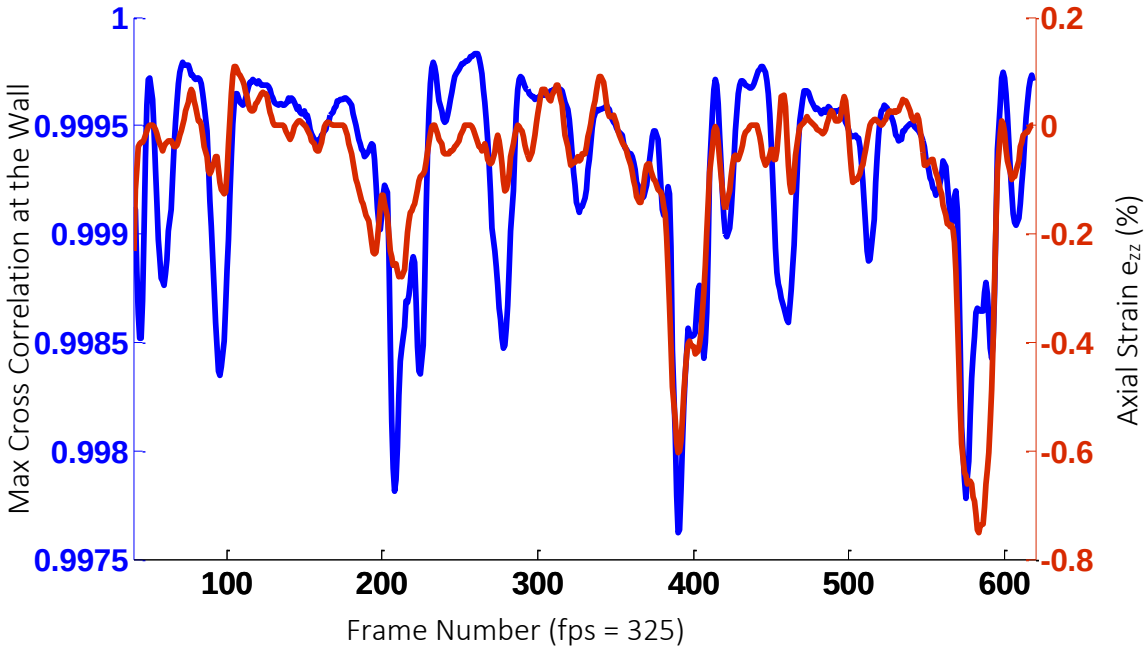

Figure (2.2) d) Variation of Max value for cross correlation and Axial Strain at the Wall of Carotid Artery

Chapter 3

Direct Strain Estimation

3.1 Introduction

So far, we have reviewed displacement tracking techniques using ultrasound and other imaging modalities and explained elastography briefly along with existing methods of estimating strain parameters. In this chapter we focus on our newly developed method for estimating different strain parameters on common carotid artery wall. As mentioned before this method can be generalized to different living tissue types and is not limited to carotid artery. Previously, it was shown that most elastography techniques rely on finding displacements through cross correlation based speckle tracking methods and derivatives of displacements for strain parameters. It was pointed out that major drawback of this type of estimations was the noise amplifying nature of gradient operator in that, it could mask small strains and show unreal fluctuations.

In this chapter first we review the mathematical theories and facts governing the formulation of our method. Then in section 3.3 we demonstrate the new algorithm and discuss it in detail.

3.2 Mathematical Components of the Problem

3.2.1 Affine Transformation

We claim that strain parameters in a tissue region can be estimated as parameters of an affine transformation. Therefore, in this section we will define affine transformation and demonstrate its role in our method. All our discussions will be in 2 dimensional space since we have been working with 2D ultrasound images. Nevertheless, this discussion can be generalized to third dimension.

Simplest form of image transformation is a linear translation, for example in Cartesian coordinates let $\Delta = [\Delta x \quad \Delta z]^T \in \mathbb{R}^2$ be the translation vector, which takes point 1 with coordinates $\vec{X}_1 = \begin{pmatrix} x_1 \\ z_1 \end{pmatrix}$ to point 2 located at $\vec{X}_2 = \begin{pmatrix} x_2 \\ z_2 \end{pmatrix}$ we will have: $\vec{X}_2 = \vec{X}_1 + T\Delta \; where \; T = \begin{bmatrix} 1 & 0 \\ 0 & 1 \end{bmatrix}$ In this transformation simply a displacement is added to initial position of the point. However, any complex motion such as tissue motion is comprised of different transformations and translation is just one of them. Tissue not only is displaced but it also deforms, i.e. it scales, shears and rotates. One of the advantages of Cartesian coordinates is that different transformations can be cascaded into one single transformation. Therefore in 2D plane all motion changes can come down to a 2x2 transformation matrix called affine transformation [111] [112]. In general, an affine transformation can be represented as a linear mapping accompanied by a translation vector. In other words:

$$\vec{X}_2 = \begin{bmatrix} 1 & 0 \\ 0 & 1 \end{bmatrix} \vec{X}_1 + \begin{bmatrix} e_{11} & e_{12} \\ e_{21} & e_{22} \end{bmatrix} \vec{X}_1 + \vec{\Delta} \qquad (3.1)$$

$$\vec{X}_2 = \begin{bmatrix} e_{11}+1 & e_{12} \\ e_{21} & e_{22}+1 \end{bmatrix} \vec{X}_1 + \vec{\Delta} \qquad (3.2)$$

Where $T = \begin{bmatrix} e_{11}+1 & e_{12} \\ e_{21} & e_{22}+1 \end{bmatrix}$ is the transformation matrix.

It should be noted that above transformation and translation can be written in one matrix but for our purpose this notation is more suitable.

Affine transformations are widely used in different imaging modalities to compare different features in images. One of the properties of linear affine transformation is that it is invertible and the inverse matrix exists, i.e. det(A) ≠0. This is an advantage since singularities can cause problems in computer programs such as MATLAB which routinely use inverse of matrices for different transformation operations. A few other properties of affine transformations are as follows [113]:

- Lines are preserved after transformation i.e. they will remain as lines.
- Parallel lines stay parallel.
- The ratios of parallel lines are preserved.

The ratio of areas in two images are preserved.

In the next sections we will demonstrate how affine transformation components can be related to strain parameters for elastic tissue materials.

3.2.2 Affine Transformation and Strain

According to definition, engineering strain is the change in length per unit of original length.

[114]

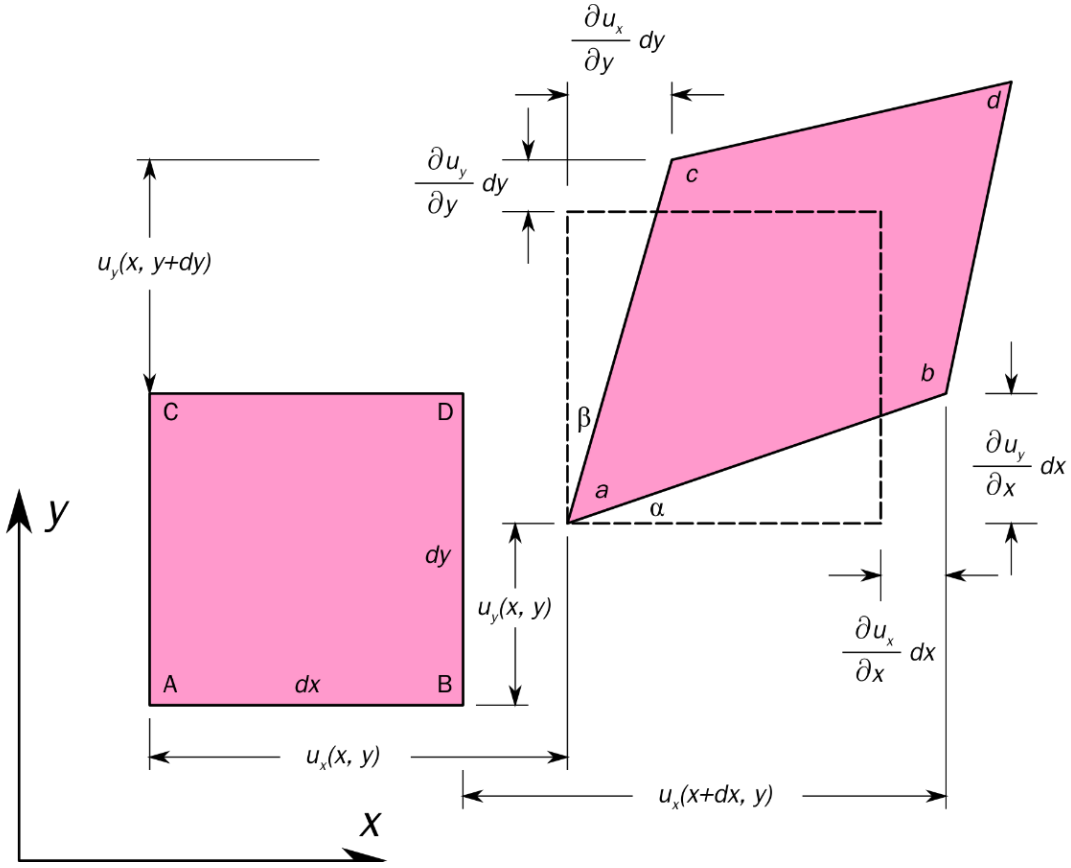

Figure (3.1) Four different strains in a 2D image (Lateral Strain, Axial Shear Strain, Lateral Shear Strain, Axial Strain)

In figure (3.1) the pink square is first translated to dashed square. u_x and u_y are displacements in x and y directions respectively. Normal and shear strains are then applied on the translated square. So according to figure we will have:

$$du_x = \frac{\partial u_x}{\partial x} dx \qquad (3.3\_a)$$

$$du_y = \frac{\partial u_y}{\partial x} dx \qquad (3.3\_b)$$

$$du_x = \frac{\partial u_x}{\partial y} dy \qquad (3.3\_c)$$

$$du_y = \frac{\partial u_y}{\partial y} dy \qquad (3\_d)$$

Where equations (3.3_a) to (3.3_d) show different strain parameters, e.g. (3.3_a) is the ratio of differential change of length (displacement) in lateral direction to unit length in the same direction and is called lateral strain or (3.3_c) shows the amount of differential change in lateral displacement for unit increase in axial length and is called lateral shear strain.

Now, rewriting equation (3.2) we will have:

$$\vec{X}_2 - \vec{\Delta} = \begin{bmatrix} e_{11}+1 & e_{12} \\ e_{21} & e_{22}+1 \end{bmatrix} \vec{X}_1 \rightarrow \begin{bmatrix} x_2 - \Delta x \\ y_2 - \Delta y \end{bmatrix} = \begin{bmatrix} e_{11}+1 & e_{12} \\ e_{21} & e_{22}+1 \end{bmatrix} \begin{bmatrix} x_1 \\ y_1 \end{bmatrix}$$

After matrix multiplication and manipulation, we will have:

$$x_2 - (x_1 + \Delta x) = e_{xx} x_1 + e_{xy} y_1 \qquad (3.4\text{-a})$$

$$y_2 - (y_1 + \Delta y) = e_{yx} x_1 + e_{yy} y_1 \qquad (3.4\text{-b})$$

The above equations show how this transformation works as a Jacobian matrix, mapping one coordinate to other. In other words, it represents local deformation. Number subscripts are also replaced with coordinates to show they are strains in different directions. It is known that if a function is differentiable at a point and its neighborhood, Jacobian matrix would be the best linear approximation of function in that neighborhood [115] [116].

Assuming a 2D motion and no rotation, two important conclusions can be deduced from the last two equations. First, axial and lateral motions are not independent of each other and there are parameters relating displacements in both directions. Therefore, motion tracking and deformation in two directions cannot be dealt with as two separable 1D problems otherwise the accuracy of computations will degrade. Second conclusion is that e_{xx}, e_{xy}, e_{yx} and e_{yy} are ratios of displacements to the original lengths and therefore would be the same as strain parameters in equation (3.3).

3.2.3 Autocorrelation and Deformation

Autocorrelation can be thought of as a measure of local uniformity of a function in time or space. In other words, it is a measure of similarity of observations as a function of spacing between them (either a time or space lag). In order to comply with the rest of notations let's assume $s(x, z, t_0)$ is the analytic received ultrasound echo signal at spatial coordinates x and z representing the lateral and axial directions at time t_0. It is assumed that the signal is obtained from a linear array and therefore spatial invariant. According to definition, power spectral density (autospectrum) function of this signal in spatial frequency domain would be:

$$\Gamma_{11}(k_x, k_z) = S(k_x, k_z, t_0)S^*(k_x, k_z, t_0) \qquad (3.5)$$

Where $\boldsymbol{k} = [k_x\ k_z]'$ is spatial frequency vector (rad/m) in x and z directions respectively and * denotes complex conjugate of the specified function. Mapping autospectrum of deformed signal into spatial domain, the autocorrelation function at a given region of interest (ROI) will be obtained.

$$\gamma_{11}(lx, lz) = \frac{1}{4\pi^2}\iint_{-\infty}^{\infty} \Gamma_{11}(k_x, k_z) e^{j(k_x l_x + k_z l_z)} dk_x$$
$$= \frac{1}{4\pi^2}\iint_{-\infty}^{\infty} S(\boldsymbol{k}, t_0) S^*(\boldsymbol{k}, t_0) e^{j\boldsymbol{k}'.\boldsymbol{l}}\, d\boldsymbol{k} \qquad (3.6)$$

l_x, l_z are the lags in lateral and axial directions respectively. If motion is comprised of a simple translation $(\Delta x\,, \Delta z)$ in lateral and axial directions, the signal at time t_1 will be the displaced version of signal at time t_0. In other words: $s(x, z, t_1) = s(x - \Delta x, z - \Delta z, t_0)$. In spatial frequency domain translations will be transformed to phase lags imposed on the system. Displacements Δx and Δz are found based on the 2D phase coupled speckle tracking complex correlation based algorithm explained in previous chapter [112].

At this stage we enter deformation in the picture and study its mathematical effects on autospectrum and autocorrelation of the signal. Due to linear nature of affine transformations, displacement and deformation can be dealt with separately. In other words, without loss of generality we assume the only transformation between signals at times t_0 and t_1 is a deformation of this form: $T = \begin{bmatrix} 1 + e_{xx} & e_{xz} \\ e_{zx} & 1 + e_{zz} \end{bmatrix}$

Where T is the deformation matrix and as it was noted in section 3.2.2 e_{xx}, e_{xz}, e_{zx}, and e_{zz} are different stain parameters.

It will be shown that local autocorrelation function of echo data contains information on power spectral density. Evolution of shape of autocorrelation consequently describes faithfully the deformation of original echo data.

In order to make the necessary changes, here we take advantage of scaling property of Fourier transform. As a reminder of Fourier scaling property, in one dimension we have:

$$F\{g(ax)\} = \frac{G(\frac{k_x}{a})}{|a|} \quad a \neq 0$$

Here k_x denotes the spatial frequency. The same property would also work in vector (multidimensional) space, except inverse of the transformation factor would be equivalent to division in 1D case. Therefore, *T* must be an invertible matrix. In other words:

$$\boldsymbol{X}_2 = T\,\boldsymbol{X}_1$$

$$F\{s(\boldsymbol{X}_2)\} = F\{s(T\boldsymbol{X}_1)\} = S((T'^{-1}\boldsymbol{k})/|T|$$

(**Bold** characters denote vectors)

Having equation (3.2) and based on scaling property of Fourier transform [117], the 2D spatial Fourier transform of received signal at time t_1, $s(x, z, t1)$ would be as follows [118]:

$$S(\boldsymbol{k}, t_1) = S(T'^{-1}\boldsymbol{k}, t_0)/|T| \tag{3.7}$$

$$\Gamma_{22}(k_x, k_z) = S(T'^{-1}\boldsymbol{k}, t_0)S^*(T'^{-1}\boldsymbol{k}, t_0)/|T|^2 \tag{3.8}$$

Equation (3.8) shows the autospectrum of the deformed signal $s(x, z, t1)$. Now we will formulate autocorrelation of deformed signal in the region of interest (ROI) based on above equations:

$$\gamma_{22}(lx, lz) = \frac{1}{4\pi^2}\iint_{-\infty}^{\infty}\Gamma_{22}(k_x, k_z)e^{j(k_x l_x + k_z l_z)}dk_x$$

$$= \frac{1}{4\pi^2}\iint_{-\infty}^{\infty} S(T'^{-1}\boldsymbol{k}, t_0)S^*(T'^{-1}\boldsymbol{k}, t_0)/|T|^2 e^{j\boldsymbol{k}'.\boldsymbol{l}}\,d\boldsymbol{k} \tag{3.9}$$

$$T'^{-1}\boldsymbol{k} = \frac{1}{|T|}\begin{bmatrix} 1+e_{xx} & e_{xz} \\ e_{zx} & 1+e_{zz} \end{bmatrix}[k_x\ k_z]' = [m_x\ m_z] \tag{3.10}$$

Change of variables will yield:

$$T'.\boldsymbol{m} = \boldsymbol{k} \rightarrow \boldsymbol{m} = T'^{-1}\boldsymbol{k}$$

$$\gamma_{22}(lx, lz) = \frac{1}{4\pi^2}\iint_{-\infty}^{\infty}\frac{1}{|T|^2}|S(\boldsymbol{m}, t_0)|^2 e^{j\boldsymbol{m}'.(T\boldsymbol{l})}d(T'\boldsymbol{m})$$

Knowing that $d(T'\boldsymbol{m}) = |T|d\boldsymbol{m}$ the result will be:

$$\gamma_{22}(\boldsymbol{l}) = \frac{1}{4\pi^2}\iint_{-\infty}^{\infty}\frac{1}{|T|^2}|S(\boldsymbol{m}, t_0)|^2 e^{j\boldsymbol{m}'.(T\boldsymbol{l})}|T|d(\boldsymbol{m}) = \frac{1}{|T|}\gamma_{11}(T\boldsymbol{l}) \quad (3.11)$$

Where $\boldsymbol{l} = [l_x\ l_z]'$ are the lags in lateral and axial directions respectively. Therefore, given the autocorrelation functions of pre-and-post deformation ROIs the transformation matrix can be obtained. Elements of this transformation matrix are the deformations (strains) in different directions. For this application displacements Δx and Δz are found prior to estimation of transformation matrix. Using the Lagrangian coordinates instead of Eulerian coordinates has the advantage of not having to shift the ROI, but simply placing the window at location of displaced speckle in second frame and then computing the transformation matrix using the above formula.

3.3 Direct Strain Estimation Algorithm

Mathematical principles of the new method were reviewed in previous sections. These principles were based on deformation estimation of local auto-correlation maps separated

at a time interval, $m\Delta t$, where Δt is the sample interval per each RF frame and m is a positive integer. In this section we will elaborate on the algorithm and its implementations which allow us to achieve direct measurement of local deformations of vascular wall. The steps of this algorithm are based on the properties of 2D local correlation (both cross correlation and autocorrelation) of the ROI going under deformation. As shown in previous section, the spatial spectra of a locally deformed ROI contains the phase distortion information when compared to pre-deformed ROI [119]. The analytic nature of ultrasound signal allows the visualization of deformation. Although these phase distortions are clearly present in the spectra, they are difficult to extract directly from the spectral distribution, especially in the presence of scattering noise. The power spectral density distribution, on the other hand, normalized by the total energy density, is less sensitive to signal noise, and consequently the algorithm based on the same principle is expected to be more robust. We will show in the later section that extracting the strain matrix, T, can be equivalently performed in the spatial instead of the spectrum domain. As a matter of fact, the deformation analysis performed over the auto-correlation maps is more straight forward and easy to be implemented. In the following, we will first describe the algorithm and discuss the implementations. Strains at the lower wall of carotid artery of a healthy subject will be estimated. Lower wall is picked for carotid artery and phantom because of less reflections and reverberations comparing to the upper wall and therefore less artifacts and higher accuracy.

3.3.1 Description of Direct Strain Estimation Algorithm

As elucidated in flow chart (Figure 3.2), the algorithm contains the following steps.

S1: Data acquisition

A sequence of RF ultrasound images were recorded using LA14-5, 128 element, linear array operating at a central frequency of 7.5MHz with the sampling frequency of 40 MHz. The recording resulted RF frames of 38.9×14.5 mm (the former being the axial). The spatial resolutions of each RF image was 18.75 μm in the axial and 0.29 mm in the lateral direction. Frame rate was set at 325 fps (frames per second). The RF sequence was sufficiently long to include several cardiac cycles.

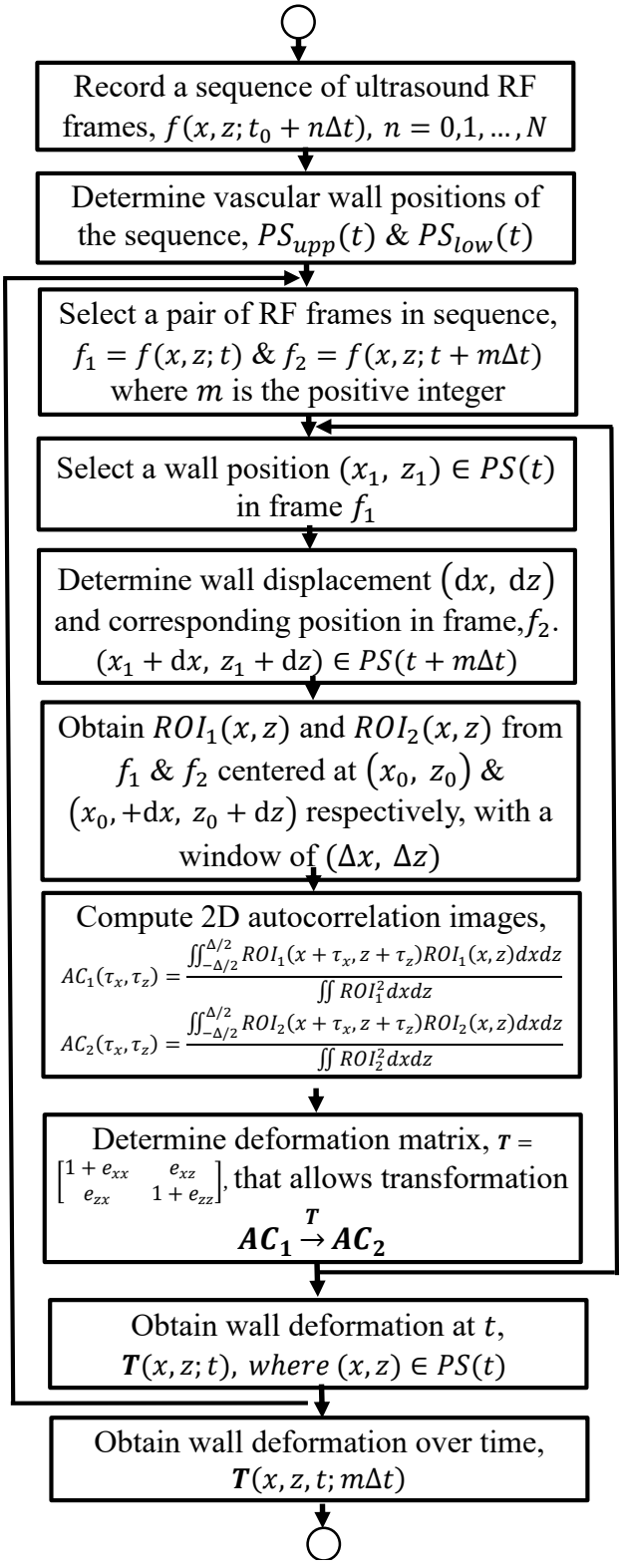

Figure (3.2) Flow diagram of the developed strain estimation algorithm.

S2: Determine kinematics of vascular walls

Since the deformations including shear and rotation are defined in the Lagrangian frame of reference, the translational motion of the vascular vessel wall must be removed first before our proposed algorithm can be applied. To determine the kinematics, the locations of the wall, $PS_{upp}(t)$ & $PS_{low}(t)$, where PS denotes a list of wall positions, (x, z), subscript "upp" and "low" suggest the upper and lower wall respectively, must be accurately obtained. Subsequently, the displacement of the wall can be extracted. If the displacements are small enough the order in which translation and transformation are applied will not be important. However, in case of large displacements or deformation the translation must be dealt with before transformation to make sure the correct Lagrangian reference is chosen.

S2.1. Determine initial wall positions at time t_0:

To obtain the kinematics of wall over the time, one needs to first extract the initial positions of wall. As pointed out in Chapter 1, B-mode ultrasound images (shown in Figure (1.4b)) produce high intensity of echo at the vessel walls due to the discontinuity of impedance at the interface of vessel wall and blood. The change in intensity at the impedance discontinuity is about 20 dB, i.e. intensity at the wall is higher than either the surrounding tissue or the blood. In the ultrasound image this intensity difference shows as two brighter regions at the wall area. It should be reminded here that wall itself is made of three different layers as described in chapter 1 (section 1.2). Intima, the inner most layer would appear as a white line. The mid-layer or media due to its smooth muscle cell (SMC) is echolucent (transmitting ultrasound waves), therefore appears as a dark region between intima and adventitia [120]. Adventitia, the outer most layer also appears as a bright region, more reflective than intima. In this manner, the regions above the upper white line and below the

lower one (referring to adventitia) are tissue surrounding the vessel and the region between two inner white lines (intima) is blood. Note that it is the discontinuity in impedance that marks the boundary of vessel and blood. Hence, this intensity variation along the axial direction could be used to determine the boundary. As demonstrated in Figure (3.3), the magnitude of an A-line signal (purple line) obtained from ultrasound images shows two groups of high intensity spikes centered around 500 and 1000, corresponding to the depth of 9.375 and 18.75 mm, i.e. upper and lower wall respectively. As one also observes, the intensity profile in axial direction is noisy. A simple edge detection algorithm cannot provide smooth wall profiles. To remove the noise in the intensity profile, envelope analysis was applied as shown in Figure (3.3), e.g. an upper envelop profile connects the local maximum points and a lower envelop connects the local minimum points. To adequately remove the noise, the multi-pass envelop analysis was applied. This multi-pass analysis combines adjacent local maxima to nearby maxima with larger values, e.g. red symbols obtained by three pass analysis contains less peaks than the blue line by two-pass analysis. It is also observed that the locations of the peaks with large value are clearly preserved. So the locations of upper and lower wall boundaries are determined as highest two peaks. In the example (Figure (3.3)), the positions are at $z = 600$ and $z = 1010$ pixels depth (11.25 and 18.94 mm in axial direction) for the upper and lower wall at given lateral position $x = 1$. Although the analysis is accurate and robust, false location can be obtained when the contrast at the boundary is low. To prevent the erroneous identification of wall position, all detected wall positions were also verified manually. The sample result is shown in Figure (3.4). Linear regression was then applied to detected points. Although the vessel wall is not completely linear in our specific ultrasound sequence it followed the

linear model with a good accuracy. A comparison then was made between detected points using both methods and no significant difference was observed. Note that the detected upper wall is on the boundary between the adventitia and surrounding tissue and the lower wall on the intima side. This observation can be easily explained by the high reflectivity as the ultrasound beam crossing from lower impedance region to the higher impedance area.

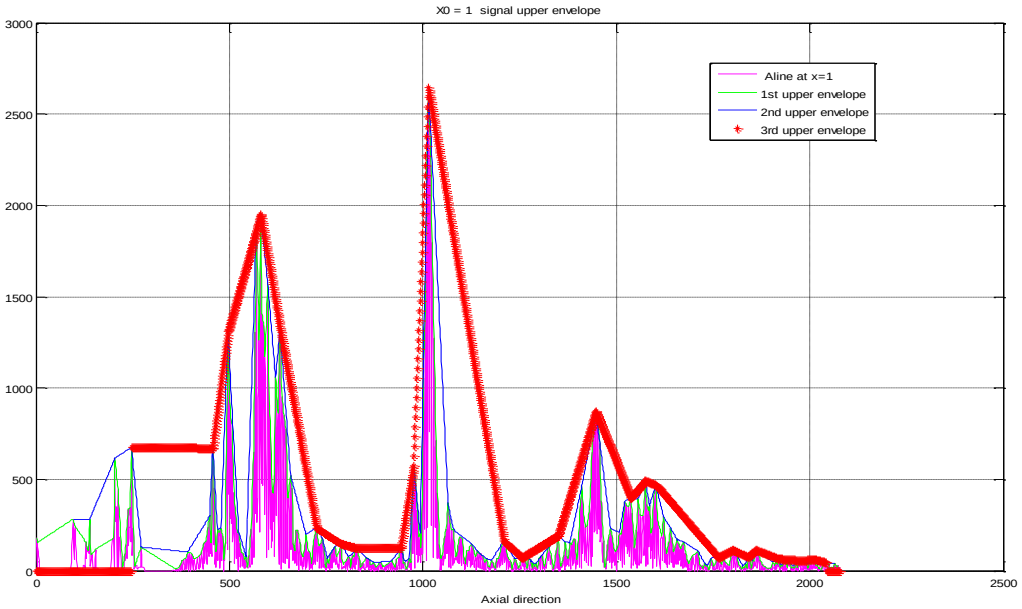

Figure (3.3): Wall detection algorithm using envelope analysis of RF profiles at the lateral position along the axial direction.

S2.2 Tracking wall motion over time:

Once the initial coordinates of the upper and lower wall, $PS_{upp}(t_0)$ and $PS_{low}(t_0)$, are obtained, the displacement of the wall, $dx[PS(t_0), t]$ and $dz[PS(t_0), t]$, at the subsequent frames, are determined with subsample accuracy using 2D phase coupled speckle tracking algorithm [112]. Accumulation of the displacements of each frame results the location of the walls in the next frame. In other words, the wall positions can then be computed as $PS(t) = PS(t_0) + [dx, dz]$. The tracking procedure replaces the initial wall positions at t_0

with the current positions at t and repeats the abovementioned procedure until the entire sequence of RF frames is processed.

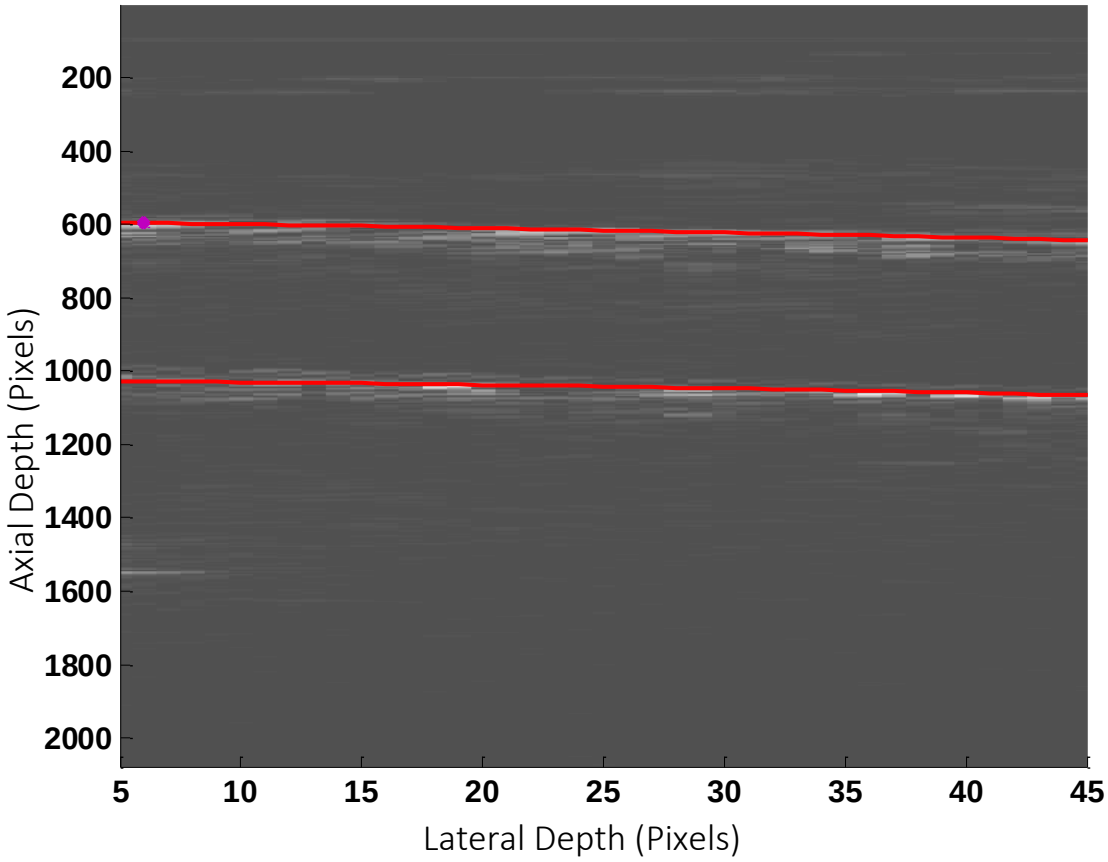

Figure (3.4) Upper and Lower wall Positions for a single frame (frame 224) of Ultrasound sequence

S3 Select a pair of RF frames within the sequence for strain parameter analysis:

To perform deformation analysis, a pair of RF frames separated by short time lapse, $m\Delta t$, were picked, where m is the positive integer indicating the number of frames and Δt is the time lapse between two consecutive frames. For brevity, we denote these two frames as

$$f_1 = f(x, z; t)$$

$$f_2 = f(x, z; t + m\Delta t).$$

(12)

It is worthwhile to discuss the proper selection of m greater than the conventional value $m = 1$, i.e. two consecutive frames. Since the frame rate was chosen to be 325 frames/sec, proper selection of time separation would optimize the measurement accuracy and reduce the measurement uncertainty.

S4. Select a position, $(x_1,\ z_1) \in PS(t)$ in frame f_1:

The position will be used as the center of Region Of Interest (ROI) to local strain analysis.

S5. Determine the corresponding position $(x_2,\ z_2)$, in f_2 to the position, $(x_1,\ z_1) \in PS(t)$ in frame f_1:

As discussed before, strain tensor,

$$T = \begin{bmatrix} 1 + e_{xx} & e_{zx} \\ e_{xz} & 1 + e_{zz} \end{bmatrix},$$

where T is the strain tensor, $e_{xx} = \frac{du}{dx}$, $e_{zz} = \frac{dw}{dz}$, $e_{xz} = \frac{dw}{dx}$ and $e_{zx} = \frac{du}{dz}$, needs to be measured in the Lagrangian frame of reference, i.e. analysis must be performed over two same tissues or ROIs at f_1 and f_2. The symbols, du and dw, denote the deformation in the x and z direction, respectively. To extract the corresponding ROI in f_2 to that in f_1, one has to find the corresponding position by obtaining the accumulative displacements as iterative equation (13).

$$dx = \sum_{i=1}^{m} dx\left(x^i, z^i; t + i\Delta t\right), dz = \sum_{i=1}^{m} dz\left(x^i, z^i; t + i\Delta t\right),$$

$$x^i = x^{i-1} + dx\left(x^i, z^i; t + i\Delta t\right), z^i = z^{i-1} + dz\left(x^i, z^i; t + i\Delta t\right) \quad (13)$$

where $x^0 = x_1$ and $z^0 = z_1$. The corresponding position can be determined as

$$x_2 = x_1 + dx$$

$$z_2 = z_1 + dz$$

Note that the formula for determining accumulative displacement is generic and capable of handling multiple frame separation (i.e. m > 1).

S5. Obtain ROIs of f_1 and f_2:

ROIs from f_1 and f_2 are obtained using the following expression,

$$ROI_1(x_r, z_r) = f_1(x_r + x_1, z_r + z_1),$$

$$ROI_2(x_r, z_r) = f_2(x_r + x_2, z_r + z_2)$$

where $-\frac{w_x}{2} \leq x_r \leq \frac{w_x}{2}$, and $-\frac{w_z}{2} \leq z_r \leq \frac{w_z}{2}$. w_x and w_z are the size of the ROI window (kernel size). Kernel size of the window was chosen to be 43×3 pixels (or $1.45mm \times 0.8063mm$) in axial and lateral directions respectively with a 50% overlap in lateral direction and no overlap in axial direction. Relatively large windows with smaller overlap in lateral and no overlap in axial direction is picked to have more available correlation space. Sample ROIs are shown in Fig. 3.5 and marked as blue box.

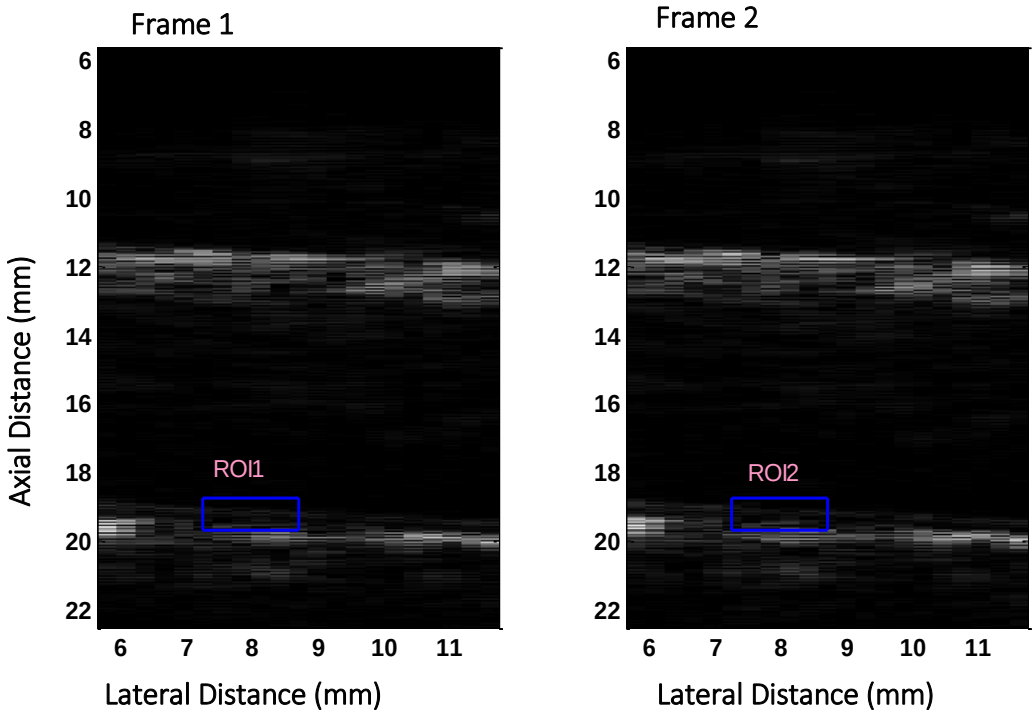

Figure (3.5): Regions of Interest (ROI) on the lower wall of carotid artery. ROIs are not drawn to scale.

S6. Compute autocorrelation function of ROIs:

Autocorrelation maps of ROIs are computed as the following.

$$AC_1(\tau_x,\tau_z)=\frac{\iint_{-w/2}^{w/2} ROI_1(x+\tau_x,z+\tau_z)ROI_1(x,z)dxdz}{\iint ROI_1^2 dxdz} \quad (14)$$

$$AC_2(\tau_x,\tau_z)=\frac{\iint_{-w/2}^{w/2} ROI_2(x+\tau_x,z+\tau_z)ROI_2(x,z)dxdz}{\iint ROI_2^2 dxdz} \quad (15)$$

Figure (3.6) shows the autocorrelation maps of ROIs shown in figure (3.5).

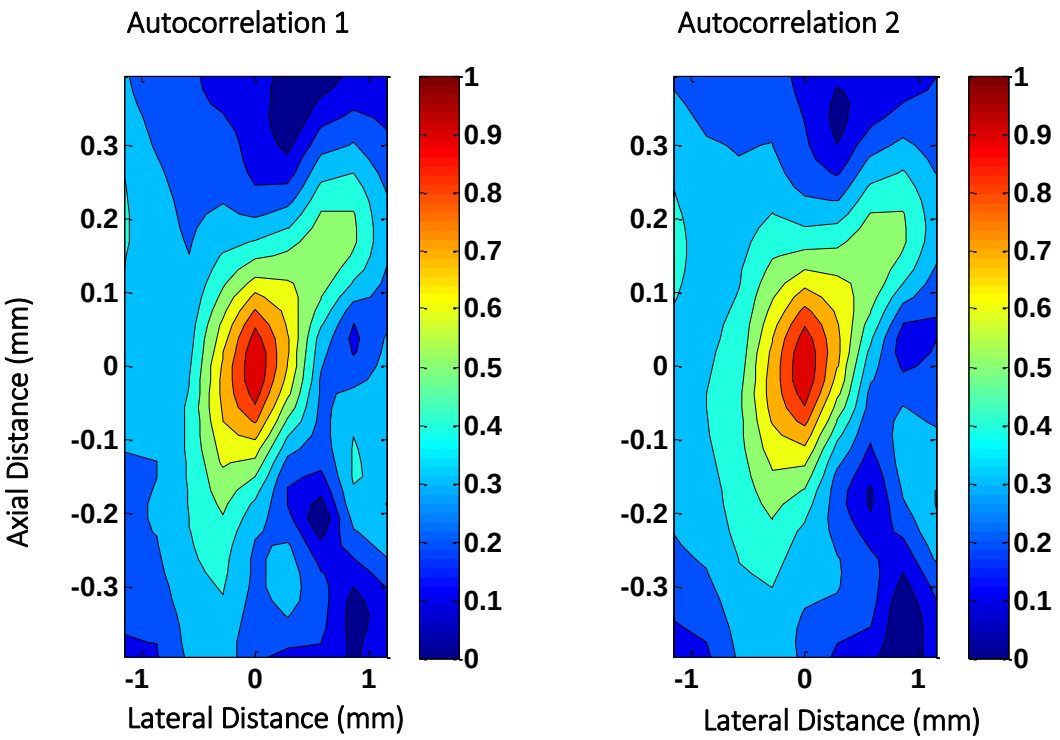

Figure (3.6) Autocorrelation of non-deformed (left) and deformed image (right)

The peak of all autocorrelation images is located at the center and has a value of 1(according to definition of autocorrelation). If the surroundings of peak are flat, comparison between two autocorrelation images will not yield much in terms of elements of transformation. Therefore, larger autocorrelation image would mean more available points to compare between two frames. Therefore the higher accuracy will be achieved at the expense of more computational cost [121] [122].

S7. Compute strain tensor, $\boldsymbol{T(x_1, z_1, t)}$:

Figure (3.6) show that the deformation information is contained in the autocorrelation maps. According to equation (3.11), autocorrelation of 2nd window (AC_2) is equal to the scaled autocorrelation of the 1st window (AC_1) multiplied by the inverse of the determinant

of the transformation. During this step of the algorithm, interpolation was avoided in both directions in autocorrelations since it proved to degrade the accuracy of parameter estimation.

An iterative scheme was applied to find the best transformation satisfying equation (3.11). To speed up iterations, parallel processing toolbox from MATLAB was used. 8 worker nodes worked simultaneously and computed different possible combinations for transformation elements. Furthermore, 4 matrix elements were updated in two separate but simultaneous "parfor" loops. In each loop two elements (either diagonal or off diagonal) were updated while the other two were fixed at previous iteration values. In order to make necessary changes for transforming autocorrelation function its grid was converted according to inverse of the intended transformation matrix and then interpolated with the new grid. This approach avoided scaling of the autocorrelation function and only changed the grid coordinates. The cost function to be minimized was the sum of difference between each coefficient of the non-deformed and deformed autocorrelation matrix.

S8. Repeat step S4-S7 by processing different wall positions until the entire wall positions are processed

S9. Repeat Step S3-S8 by selecting different pairs until the entire sequence is processed.

Chapter 4

In vitro and *in vivo* Results

4.1 Introduction

In previous chapters we gave a general overview of evolution of displacement tracking and elastography methods using different imaging modalities with an emphasis on ultrasound imaging of vessel walls. Furthermore, we introduced our new method, outlined the mathematics governing the formulation and went through the steps of the algorithm. We demonstrated how the method takes advantage of properties of Fourier transform and local autocorrelation function to directly estimate normal and shear strains. In order to validate the new direct strain estimation method, we conducted some experiments and applied the new direct strain estimation to *in vitro* and *in vivo* ultrasound data. Results from vessel mimicking phantom experiment, elastography phantom data and *in vivo* carotid artery were all in compliance with theoretical expectations with high accuracy. In this chapter we demonstrate the setup of our experiments and data acquisition procedure. The steps of data processing and direct strain estimation will be addressed through figures, mathematical expressions and descriptions. Finally, the results will be discussed.

4.2 Vessel Mimicking Phantom Experiment

4.2.1 Experiment Setup

Flow through a 4 mm vessel mimicking flow phantom (ATS Model 524) was imaged longitudinally using a commercial ultrasound scanner with research mode capabilities

(Sonix RP, Ultrasonix, BC, Canada). Linear array LA14_5 probe was used for this experiment. RF beamformed data collection was synchronized with pressure sensors at both ends of the vessel mimicking phantom for purpose of collecting inlet and outlet flow pressure. A flow sensor was also installed at the inlet of flow phantom to collect flow data. However, due to large difference between response times of our system and the sensor (sensor's response time was about 1 min) its output was not used in our analyses. Experiment set up is shown in figure (4.1). Roller pump (Cole-Parmer MasterfFex) was set to a speed reasonably close to that of blood in human carotid artery (e.g. 360 ml/min [123]). The ideal flow type for this experiment would be a pulsatile flow resembling the pressure induced blood flow in arteries. The sinusoidal flow produced by roller pump however, can be considered close enough to mimic pulsatile flow of blood in artery. An Arduino microcontroller synchronized the sensors and ultrasound system trigger. Collected data from the ultrasound machine and pressure sensors were saved on a PC through a terminal. In order to mimic blood, celluloid microspheres were added to water to act as linear scatterers.

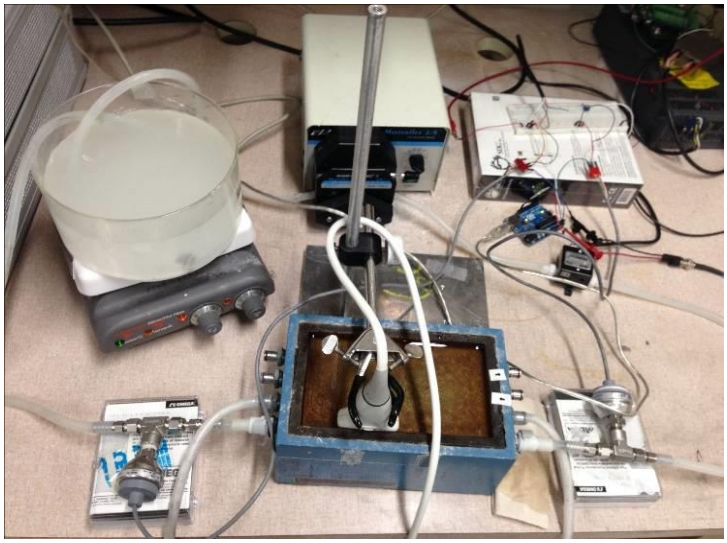

Figure (4.1) Flow phantom experiment setup. A roller pump produces sinusoidal flow. Pressure sensors are placed at the inlet and outlet of phantom.

4.2.2 Data Acquisition

A home developed program [124] was loaded on Sonix RP (Ultasonix, Canada) scanner to be used with LA14-5/38 linear array probe at center frequency of 7.5 MHz and frame rate of 448 frames per second to provide high frame rate M2D pulse-echo data [125]. Collected data was processed offline on a PC using MATLAB software. Ultrasound probe was positioned parallel to channel axis to provide longitudinal images of the phantom. In order to induce disturbance in flow, roller pump was switched off and on quickly during data collection. Imaging continued until system reached steady state. Inlet and outlet pressure data was collected by means of two pressure sensors.

4.2.3 *In vitro* Results and Discussion

Strain parameters at posterior wall of vessel mimicking phantom were estimated using two methods. First, lateral and axial displacements were estimated using 2D phase coupled speckle tracking [14]. Strain parameters were computed by taking spatial gradients of displacements in both directions.

Then we used the new proposed method to directly estimate strain parameters as a linear affine transformation matrix. Figure (4.2) shows a comparison between strains obtained by both methods. They both follow same pattern and are mostly in phase. The rise and fall of diameter is intended to mimic the change of diameter in blood vessel during systole and diastole. Strain values follow diameter waveform with some phase difference.

Figure (4.2) shows estimated strains by both methods. Both methods show the same pattern of change and are in phase for the most part of the heart cycle. For all four strains it is shown that directly estimated parameters from equation (3.2) are less noisy than those

using gradient of displacements. These observations are backed by mathematical theories since it is known that gradient is a noise amplifying operator [126]. Furthermore, values of S_{xx} and S_{zx} (gradient driven lateral and lateral shear strain) are comparably smaller than those of e_{xx} and e_{zx} (from direct estimation) respectively. Large lateral velocity of flow suggests relatively large values of lateral strains. In fact, lateral resolution is very poor a result of lack of signal carrier [112]. Therefore, accuracy of displacement estimation in axial and lateral direction isn't the same. Displacement accuracy is much less in lateral

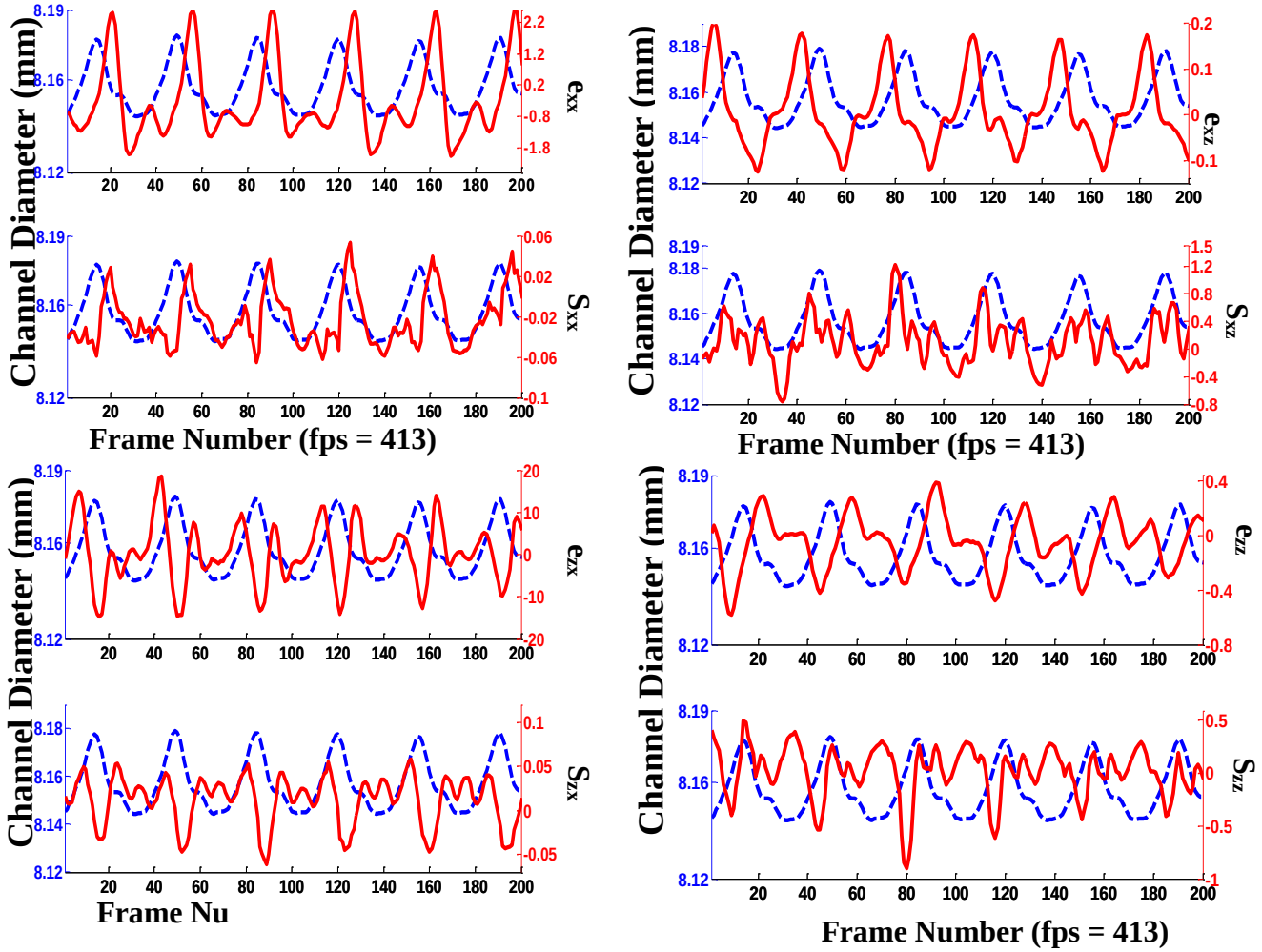

Figure (4.2) Lateral strain (Top Left), Axial Shear Strain (Top Right), Lateral Shear Strain (Bottom Left), Axial Strain (Bottom Right) Blue dotted lines show channel diameter during 6 cycles. In each section strain parameter based on affine transformation (above) and parameters based on 2D speckle tracking (below) are shown.

direction and derivative operator will degrade the estimation accuracy even further, hence the small values for lateral and lateral shear strains.

4.3 Elastography Phantom experiment and results

4.3.1 Setup and Data Acquisition

Using a gelatin phantom Sridhar et.al [127] designed a compress-hold-release experiment to study viscoelasticity using ultrasound. The RF data for this experiment is available online [128]. Using this dataset (first sequence of data) we were able to validate the new method qualitatively. The details of experiment and data acquisition specifications are explained in [127]. In this compress-hold-release experiment RF data is acquired pre, post and during compression with a frame rate of 4 frames per second. A fast ramp stress is applied at the direction of the ultrasound beam. This experiment was initially designed to detect viscoelastic characteristics of the phantom material such as relaxation and retardation which asked for long duration data collection. However, only elastic behavior of the phantom was in our interest since elastic solids never relax. Therefore, we processed the first few seconds of ultrasound data when the ramp stress was applied. Figure (4.3.a) shows the setup of experiment. 2D phase-coupled speckle tracking algorithm [112] was applied to data to find axial and lateral displacements. Gradients of displacement data in different directions produced strain parameters. Strain parameters were also estimated using our proposed algorithm to validate our method.

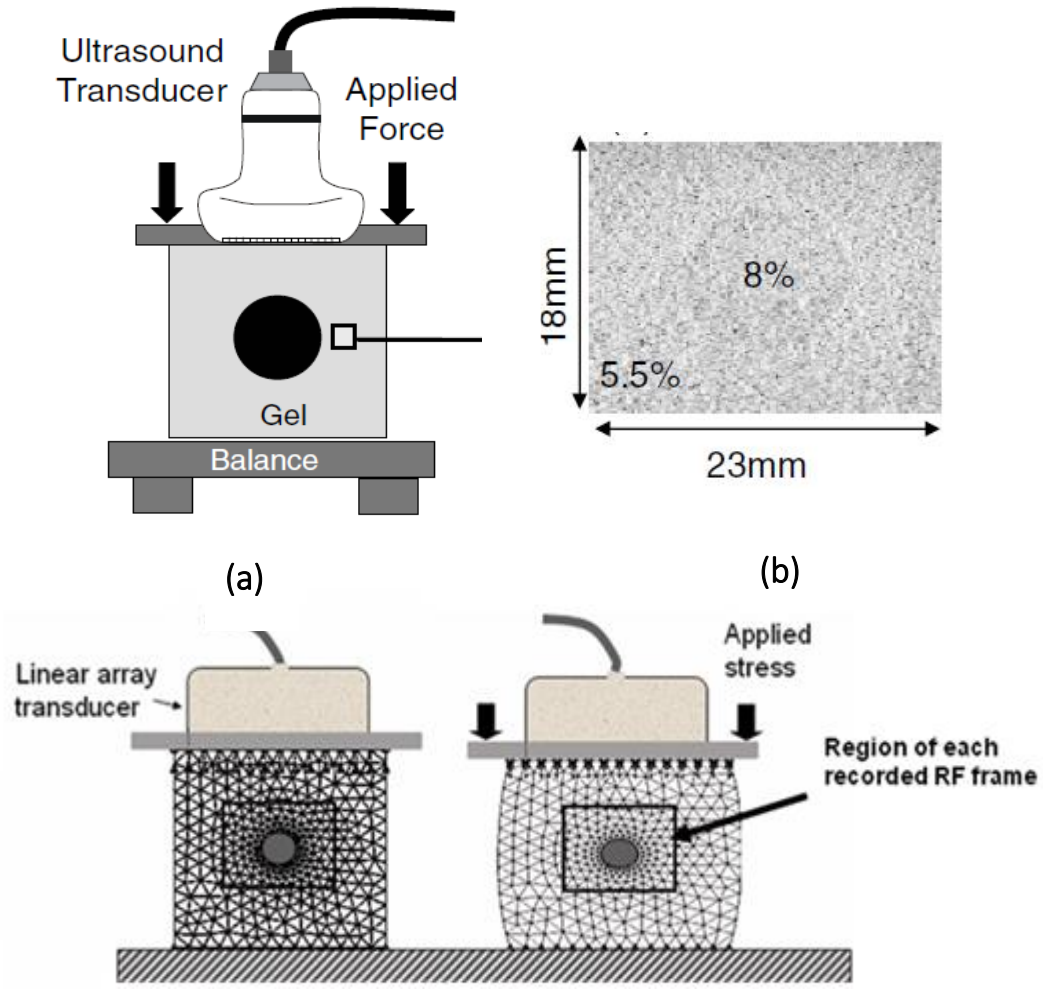

Figure (4.3) Schematic figure of elastography experiment setup (a) B-mode image of phantom (b) schematic of phantom before and after application of stress (Taken from [5] and [6])

4.3.2 Results and Discussion

Figure (4.4) shows axial and lateral displacements at two regions on the right and left half of the phantom.

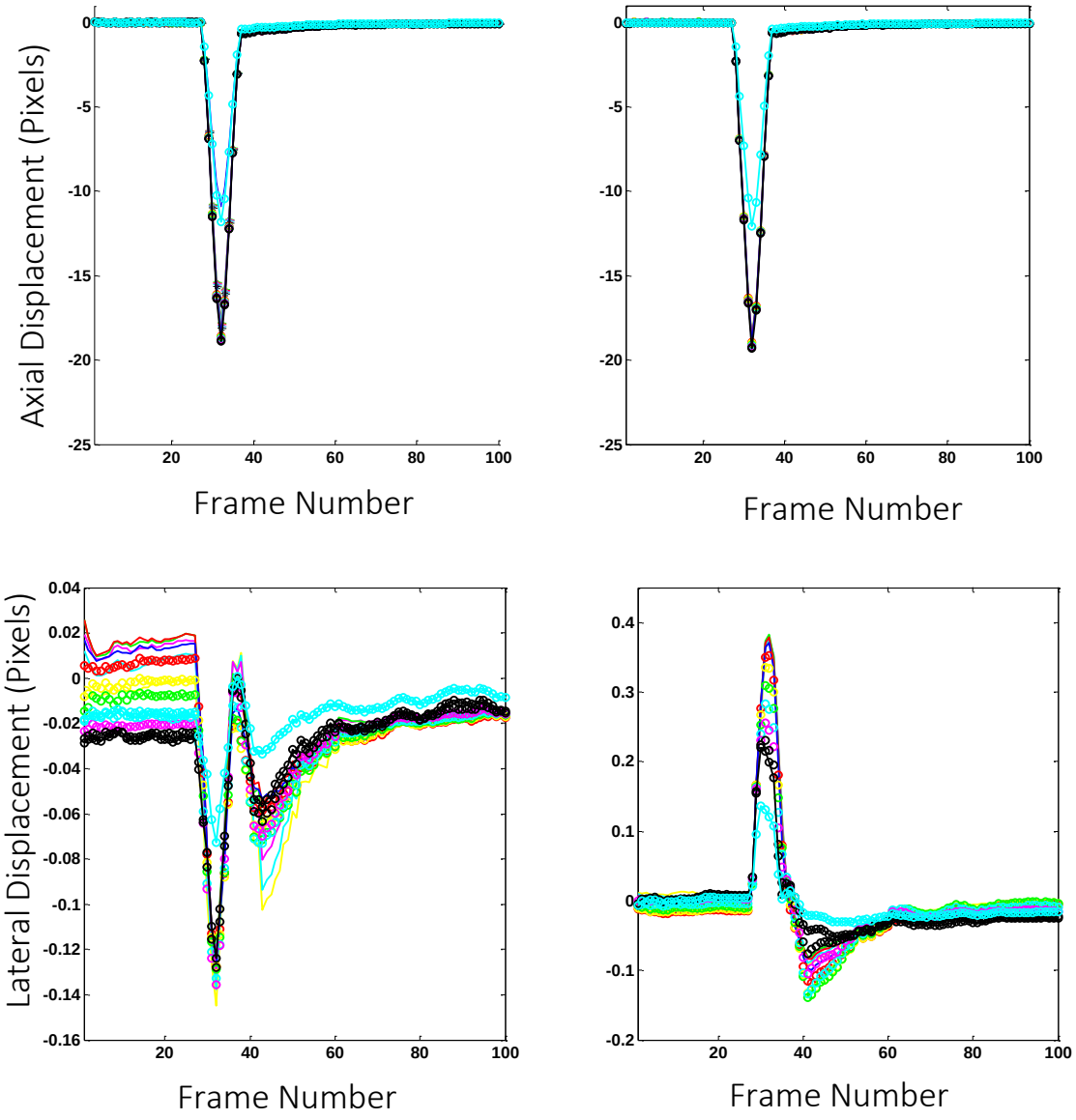

Figure (4.4) Axial (top) and lateral (bottom) displacements of on region at the left half (left) and one region in the right half (right) of the elastography phantom.

Schematics of the setup and simulation of experiment in figre (4.3) show symmetric uniform stress being applied to to surface of the phantom. Therefore, axial displacement is expected to be distribured uniformly in the phantom materail. Figure (4.4) confirms the uniformity of applied stress because axial displacements follow exactly the same pattern and almost similar values in both sections of the phantom. The sudden change in displacement is associated with the incidence of applying the ramp stress along the top surfac of phantom. Meanwhile the assumption of incompressibility (or conservation of ealstic body volume) implies no volume change in the phantom material due to stress [129]. Therefore when the material is pushed down axially, it will bulge out from both sides (laterally). In other words, lateral displacements in right and left half of the phantom would be in opposite directions. This can be clearly seen in figure (4.4) (bottom).

Strains were computed using the spatial gradients of estimated displacements and dierct strain estimation method. Reuslts are shown in figure (4.5).

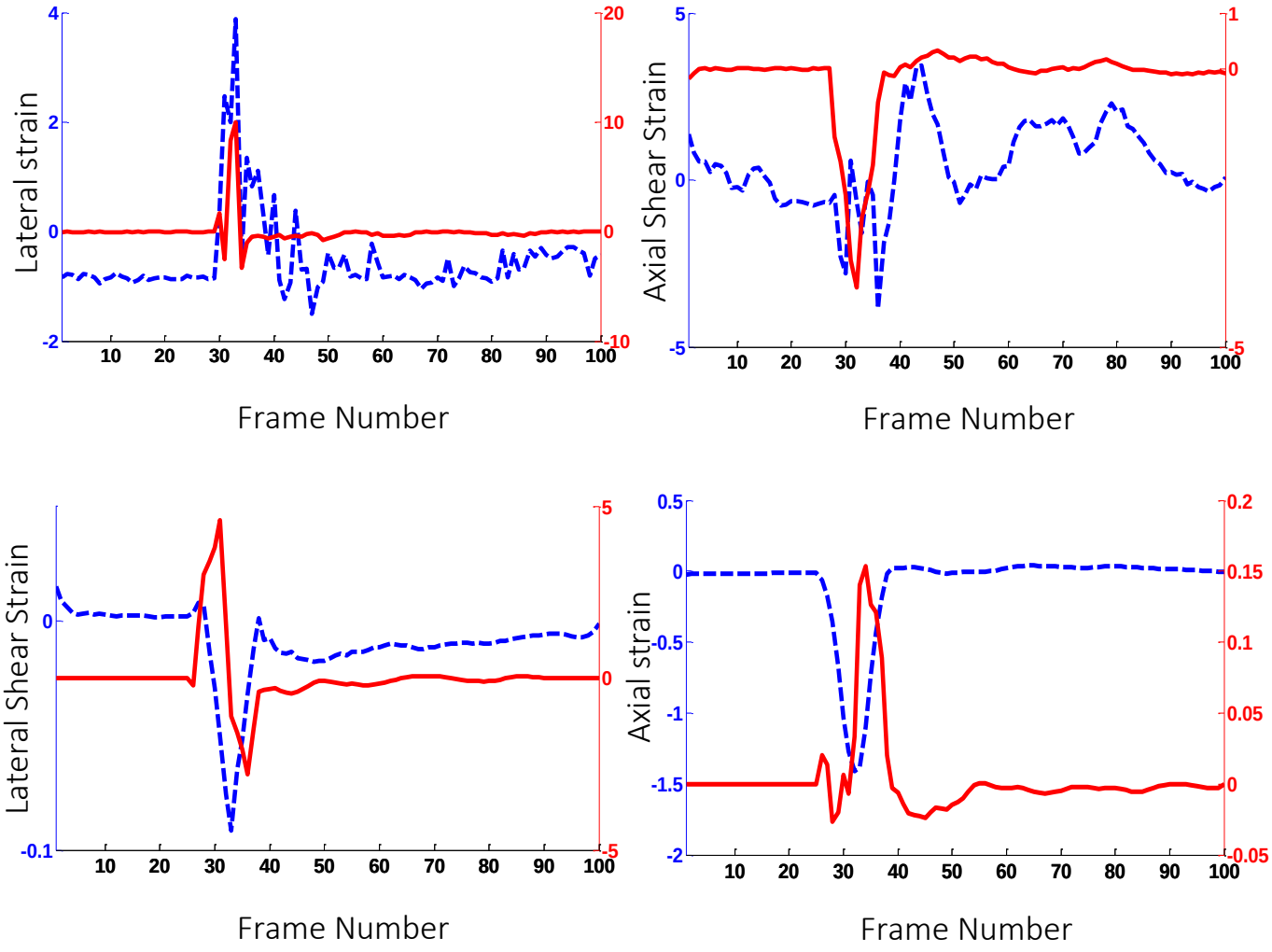

Figure (4.5) Strain parameters for one region of the phantom: Lateral Strain (Top Left), Axial Shear Strain (Top Right), Lateral Shear strain (Bottom Left) and Axial Strain (Bottom Right). Blue curves are gradient based strains and Red ones indicate affine transformation parameters.

Strains from both methods are in general agreement and comply with each other. Displacement and strain profiles show that changes start to happen around frame 30. Imaging is done at a frame rate of 4 fps, therefore, the impact of stress is visible approxiamtely 7.5 seconds after start of imaging. In the original experiment external stress remains constant for a duration of time to study creep characteristics of gelatin phantom. However, we are interested in detecting elastic parameters. Elastic properties of this viscoelastic material prievails only at the start of force application and tapers off quickly [130].

4.4 *In vivo* Measurement Experiment

Ultrasound data from common carotid artery of a healthy volunteer was collected in supine position using LA14-5 probe at 325 frames per second. The subject was asked to hold her breath during data collection. Similar to *in vitro* experiments ultrasound data was stored and processed offline using MATLAB software. Displacement and velocity profiles were estimated using 2D phase coupled speckle tracking. Relatively small correlation kernel size of 0.87 mm by 0.806 mm (3 x 43 pixels) in lateral and axial directions were picked in the region of interest (ROI). The purpose of small lateral size was to capture small displacements, since the pitch of linear array is around 290 μm, much larger than speckle size causing low lateral resolution. Strain parameters of posterior wall were estimated using 2D phase coupled speckle tracking and direct estimation method. Same kernel size was picked for autocorrelation windows in direct estimation. No interpolation was done in either direction in original data or after autocorrelation to make the analysis more accurate,

in spite of small deformation values. In fact, interpolation of factor 10 in the lateral direction proved to make the results noisier.

4.4.2 *In vivo* Results and Discussion

Similar to *in vitro* results, strain parameters of the posterior wall of artery are shown in figure (4.6) using two methods. ROI was chosen on the lower wall since the effect of reverberation decreases with depth, therefore there would be less shadow and artifact than on the upper wall area.

Figure (4.6.a) top left, shows lateral strain (e_{xx}) of the lower wall of carotid artery and diameter waveform for 3 heart cycles. Change of diameter shows the contraction and expansion along vessel wall (perpendicular to the beam) in different sections of the heart cycle. Observations on lateral strain show negative slope at the beginning of systole followed by sign change in the later part of systole. Exactly at the start of systole the negative strain starts to increase, indicating contraction in longitudinal segments of arterial wall. It was shown in chapter two that largest drop in maximum cross correlation also occurs at time of sign change (at negative peak of lateral strain). This might be due to pulse wave propagation (which will be discussed in detail in next chapter) and large volume of blood flow at the beginning of systole. Contraction is followed by an extension starting at the inflation point of diameter of the artery. Longitudinal extension continues until the slope of diameter changes sign and diastole phase starts (the second drop in maximum cross correlation). The maximum extension is about 0.8% and the maximum contraction is about -4.4%, which shows good agreement with previously reported values by Ahlgren and Lindstrom group [131].

Shortly before beginning of systole axial shear strain (e_{xz}) rises from its minimum to maximum value and during systole decreases with a negative slope. At the beginning of diastole, it reaches another local minimum.

Longitudinal shear strain (e_{zx}) shows a positive increase shortly before the beginning of systole (similar to the time lead of other parameters) followed by a decrease.

The positive and negative slopes of shear strain (e_{zx}) occur at the same locations as the first antegrade and retrograde longitudinal movements on the wall shown in [131]. Peaks of the strain curve show large values (5% and -7%) indicating difference between longitudinal movement of different layers in intima-media and adventitia complex of the artery wall (sliding of different layers on each other).

It should be pointed out at this stage that different strains are driven by different factors, i.e. change in any of four strain parameters is dependent upon different factors. As an example, radial and circumferential strains are caused by blood pressure wave and conservation of vessel wall volume dictates radial strain to be inverse to that of blood pressure wave, however similar in shape and pattern change [132]. This can be observed for axial strain (e_{zz}) which starts to rise after the start of systole however not completely out of phase with it. On the other hand lateral strain would be more complicated since it is caused by a combination of different factors such as wall shear stress (which will be explained in next chapter), pressure pulse wave, tethering of vessel because of heart contractions and conservation of volume of vessel wall [131] [132].

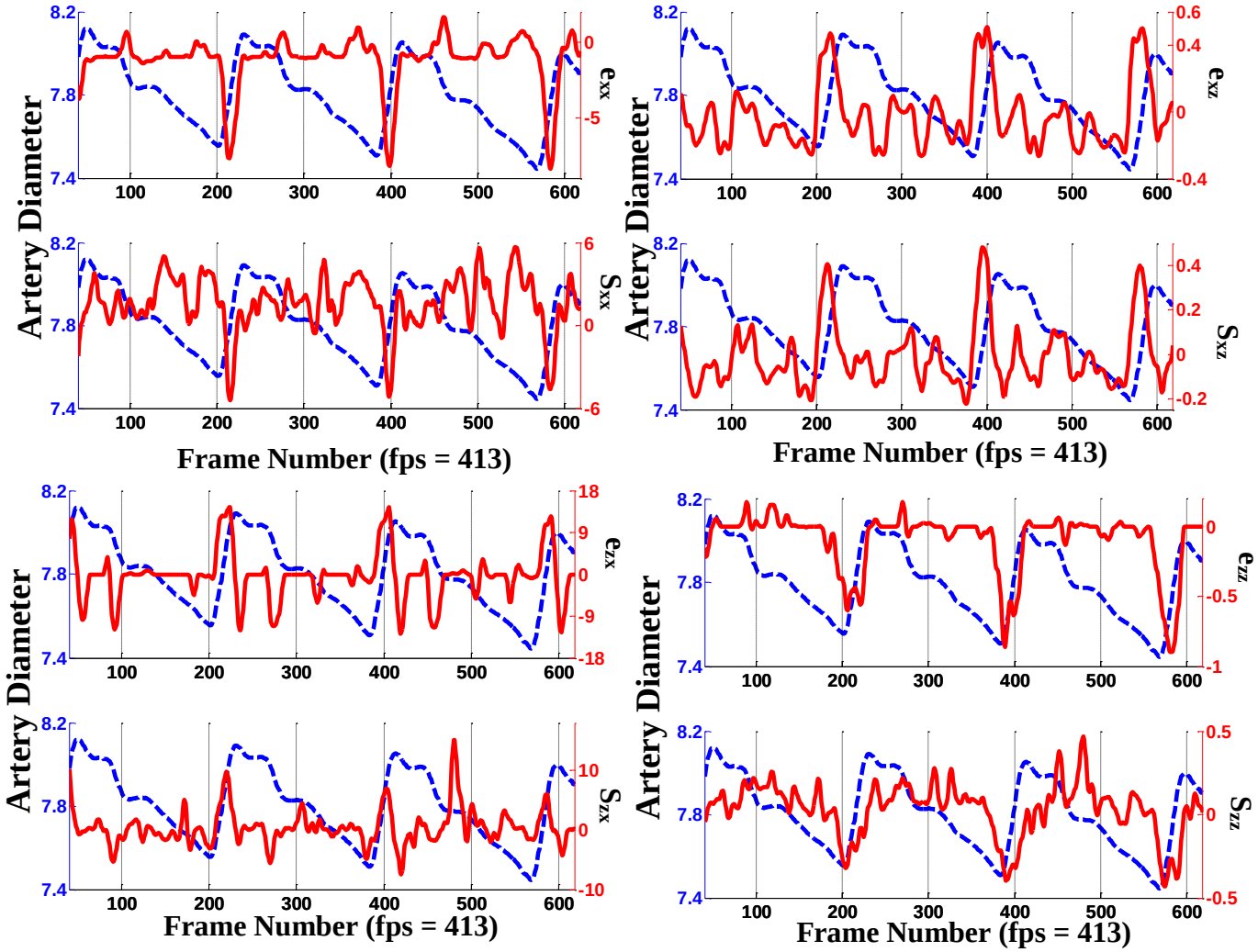

Figure (4.6): Lateral strain (Top Left), Axial Shear Strain (Top Right), Lateral Shear Strain (Bottom Left), Axial Strain (Bottom Right) Blue dotted lines show Carotid artery diameter change during 3 cycles. In each section strain parameter based on affine transformation (above) and parameters based on 2D speckle tracking (below) are shown.

Chapter 5

Other Wall Parameters

5.1 Introduction

Main focus of present research has been on finding and validating a new direct method to measure elastic properties of living tissue with an emphasis on vessel walls. In the meantime, some other elastic characteristics of vessels related to stress/strain such as pulse wave velocity (PWV), wall shear stress (WSS) and wall shear rate (WSR) have been measured. These characteristics are widely used as independent risk factors in cardiovascular diseases. The effort has been to derive these characteristics based on directly estimated strain parameters.

Measurement of pulse wave velocity (PWV) is a widely used diagnostic tool to reveal abnormalities in the arterial tree such as arterial stiffness or changes in blood pressure. However, the gold standard for this measurement (explained in next section) depends highly on different variables and assumptions challenging its accuracy. Besides that, most measurement techniques result an estimate of the average or global PWV along the arterial tree which doesn't provide any local information on the points along the path of measurement sites, in which case the local changes in stiffness may be ignored.

In the course of our study we intended to find out if parameters such as PWV could be measured more accurately and independently based on the results of new direct strain estimation method.

In this chapter we show our approach towards finding different elastic parameters and study the feasibility to obtain satisfactory results.

5.2 Pulse Wave Velocity (PWV)

Pulse wave velocity (PWV) is the subject of interest in many cardiovascular diseases. For example, in the case of decrease in systemic compliance of the arteries, PWV increases which results an increase in systolic blood pressure. Decrease in compliance is one of the earliest signs of abnormality in the vessel wall [133]. Also in atherosclerosis it is known that PWV along the arterial tree is not the same at all locations (local differences) [134] [135].

PWV is the result of dividing the distance between two measurement sites by the time it takes for the foot of the pressure wave to travel from first to second point [136].

As the heart pumps blood out through contraction of left ventricle and sends it to ascending aorta, a pulse wave (pressure wave) travels along the arterial tree. On the other hand at the end of systole and beginning of diastole pressure waves reflect back towards the heart [137]. There are different equations for PWV and therefore different estimation methods. Moens-Korteweg (1878) equation relates PWV to elastic modulus E and thickness of wall h:

$$C_p = \sqrt{\frac{Eh}{2R\rho_b}} \tag{5.1}$$

where C_p is the velocity, R is radius of artery and ρ_b is the mass density of blood [138]. The relation between PWV and arterial wall thickness in Moens-Korteweg equation, implies that C_p can also be a measure of arterial stiffness.

Another equation for estimating PWV locally was introduced by Bramwell-Hill (1922):

$$PWV_{BH} = \sqrt{\frac{\bar{A}}{\rho}\frac{PP}{\Delta A}} \tag{5.2}$$

Where PP is the pulse pressure, $\bar{A}$ is time-averaged cross sectional area of the vessel and ΔA is the difference between area in systole and diastole. The above equation shows how an increase in PWV will cause the increase in pulse and therefore blood pressure.

Bramwell and Hill also simplified Moens-Korteweg equation into:

$$C_p = 3.57/D_p \tag{5.3}$$

Where $D_p = dV/dp/V$ is the distensibility waveform which can be defined as relative change in volume due to change in blood pressure [139] [140] [141].

The gold standard for measuring PWV is the "foot to foot" method which avoids the use of pulse pressure. In this method the time delay between the foot of diameter at two points along the arterial tree is measured simultaneously. These two points are typically chosen along common carotid and femoral arteries for large enough time delay [134]. The estimated PWV from this method is an average and cannot be assigned to all sections of arterial tree. Besides, in this measurement the distance between carotid and femoral arteries is obtained by a measuring tape, i.e. the arterial tree is assumed to be lying along a straight line between these two sites. In practice this is not a true assumption and therefore the result

is not very accurate. On top of that the “foot” of pressure wave is not always clear due wave reflections. The attempt is to choose the foot of the wave as the section with smllest amount of reflections.

During recent years some studies have suggested methods for local measurement of PWV. Noninvasive ultrasound techniques to find PWV either use the measurement on wall pulsation or velocity as these two are interchangeable through derivative of wall pulsation (displacement) [142] [143].

One method is inducing low frequency ultrasound bursts to produce pressure wave. This pressure wave is superimposed by the natural pulse pressure and the transit time at different pressure levels can be determined. Therefore through this noninvasive method pressure and flow dependent velocity can be determined [144] [145].

In 2012 Konofogou et al. studied the feasibility of imaging the local pulse wave in human carotid artery. They found the displacement at different segments of the wall using a normal 1D cross correlation technique [146]. Choosing the wall velocity waveform, they picked the foot of the wave to be the inflection point in which acceleration (second temporal derivative of displacement) reaches its maximum. The time between foot of the wave was measured knowing the distance the pressure wave had to travel. PWV is the ratio of distance to the time delay i.e. the reciprocal of slope of the line showing the distance traveled in time between each foot of the wave [147].

In 2013 Liu et al. measured the length between two sample points on carotid artery wall and the transient time (the time pulse wave takes to reach from point 1 to point 2) between them noninvasively using velocity vector imaging technique [135]. Local PWV was

calculated in a region of carotid artery about 1 cm proximal to the bifurcation. They found PWV to be between 1.13 and 20.9 m/s for different healthy subjects. However, the frame rate they chose (38-50 m/s) was not high enough to be able to record small shifts.

5.3 PWV Estimation Using Affine Transformation Parameters (feasibility study)

In previous section we defined PWV and its importance as in independent indicator of cardiovascular diseases. We also briefly mentioned a few methods for estimating PWV locally. The purpose of this review was to find out if affine transformation parameters could be used to measure PWV. Strain parameters were imaged in time along lateral direction. A specific point on the strain waveform corresponding to foot of the diameter wave was picked and followed in time. Dividing the distance strain waveform travels by the time delay in that distance is expected to result PWV. The estimation method is similar to Konofagou's method [148] however no displacement or velocity estimation was needed.

Before using strain parameters for estimation local PWV we computed global PWV using the conventional wall displacement and velocity profile. Axial displacement at the lower wall was estimated using 2D phase coupled speckle tracking [119]. Figure (5.1) shows diameter, axial displacement and velocity profiles of the lower wall.

Axial velocity of the lower wall is computed, multiplying the displacement by inverse of frame rate. A median filter with size of 0.1 mm by 1.45 mm in axial and lateral directions respectively was used to reduce the noise the noise and outliers in displacements. Since axial velocity follows exactly the same pattern as distension waveform, it can be used for PWV estimation as well. In order to do the calculation, the foot of velocity wave, which is

the time instance with minimum scatterer reflections must be found. Otherwise the superposition of reflections with the PW will result inaccurate velocity measurements [149].

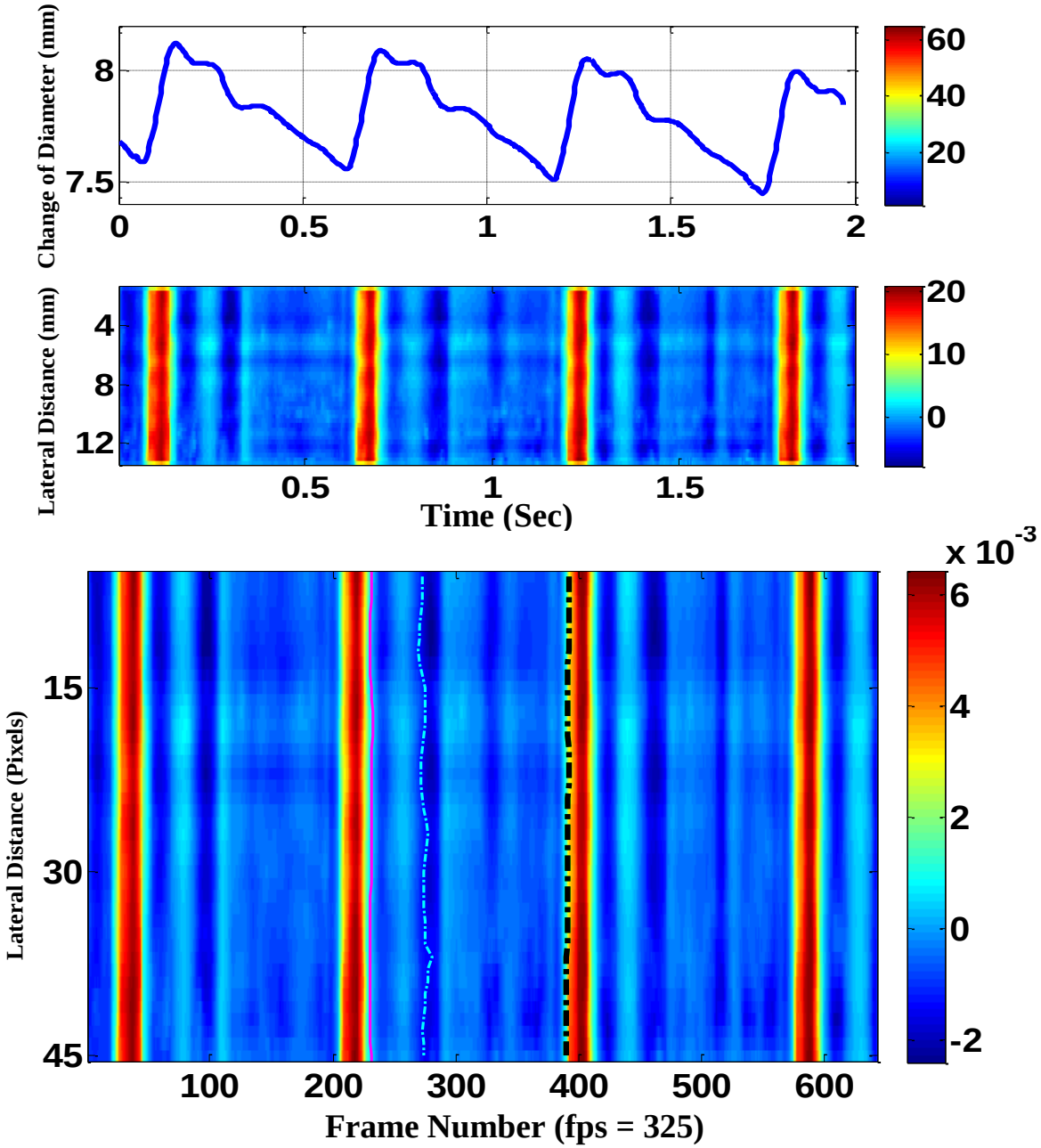

Figure (5.1) Carotid Artery Diameter Change (Top) Axial Displacement on the lower wall in (μm) (Middle) Lower Wall Axial Velocity (m/s) (Bottom)

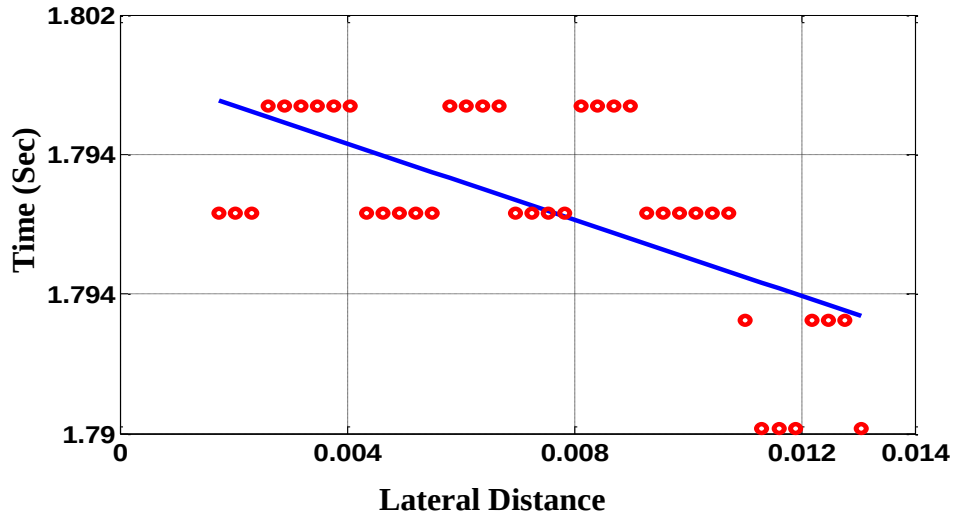

Figure (5.2) Linear Regression for Foot of the Wave and 3rd Cycle

There are different approaches for identifying foot of the wave. We assumed it to be at the inflection point (second order derivative zero) on the distension wave [150]. The time of occurrence of the foot of wave was plotted versus the lateral traveled distance. Linear regression of the resulting points can determine the ratio of lateral distance to time of travel (inverse of slope of regression line).

PWV from the above regression was estimated to be about -1.92 m/s. The negative sign indicates the direction of velocity wave propagation.

PWV at some different points other than the foot of 3rd cycle systole were also calculated for comparison. Table 1 shows these values.

PWV at peak of 2nd systole (v1) (m/sec)	-6.0417
PWV at diastole of 2nd cycle before dicrotic notch (v2) (m/sec)	1.1722
PWV at 20% of systole of 3rd cycle (v3) (m/sec)	-4.005
PWV at foot of systole of 3rd cycle (v4) (m/sec)	-3.40
PWV at foot of systole of 2nd cycle (v5) (m/sec)	-2.30
PWV at foot of systole of 4th cycle (v6) (m/sec)	-2.941

Table (5.1) Table 1: Pulse wave propagation at different stages of 3 heart cycles.

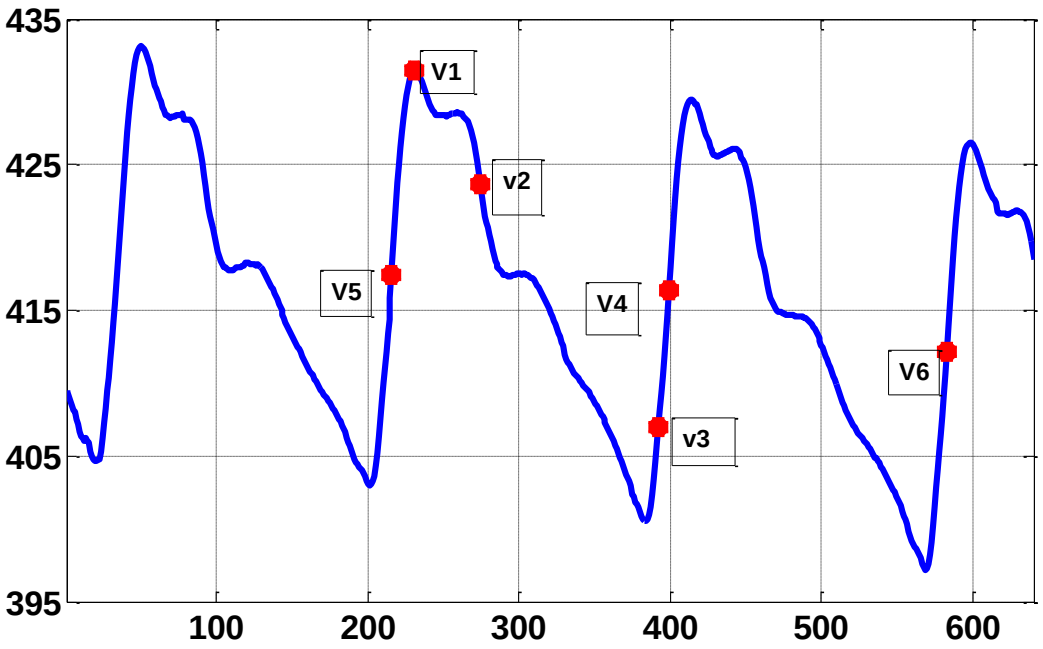

Figure (5.3) Different time instances picked for PWV with regards to change of diameter (heart cycle) in table 1

Performing the same procedure on diameter waveforms will result approximately the same PWV values:

PWV at diastole of 1st cycle after dicrotic notch (m/sec)	-0.1715
PWV at foot of the wave at systole of 2nd cycle (m/sec)	1.39
PWV 20% from the beginning of systole 3rd cycle (m/sec)	2.5424

Table (5.2) Pulse wave propagation at different stages of 3 heart cycles.

From the above calculations PWV is estimated to be 2.76 ± 0.9 m/sec.

After testing velocity and diameter waveforms for PWV estimation, axial strain parameter (e_{xz}). Spatiotemporal profile of strain was plotted and the same procedure was followed to estimate PWV. The measurement was performed at the beginning of second heart cycle, i.e. beginning of systole.

Outliers were removed from e_{xz} by a 5x5 median filter followed by a running average.

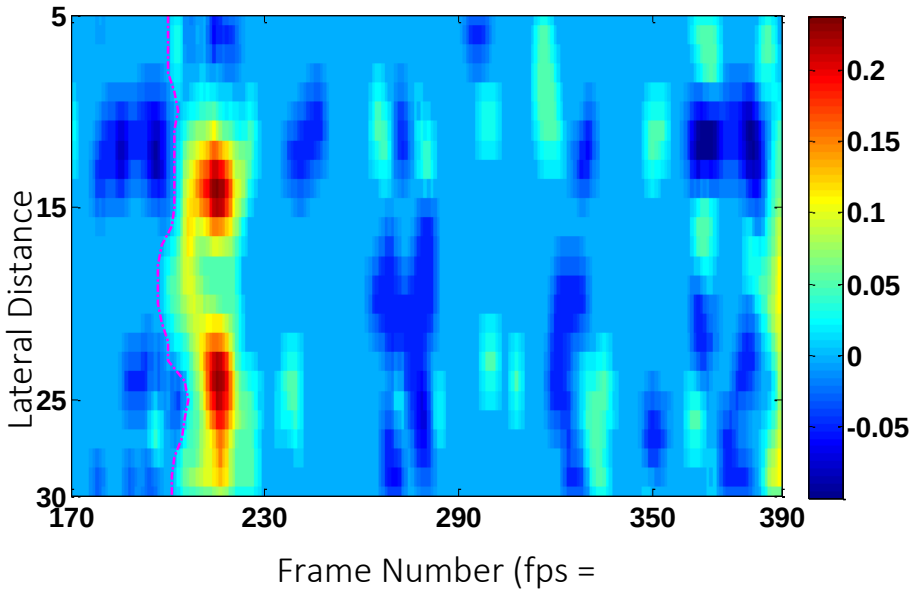

Figure (5.4.a) Profile of Axial Shear Strain (e_{xz}) For One Heart Cycle. The dotted curve indicates the beginning of cycle (beginning of systole).

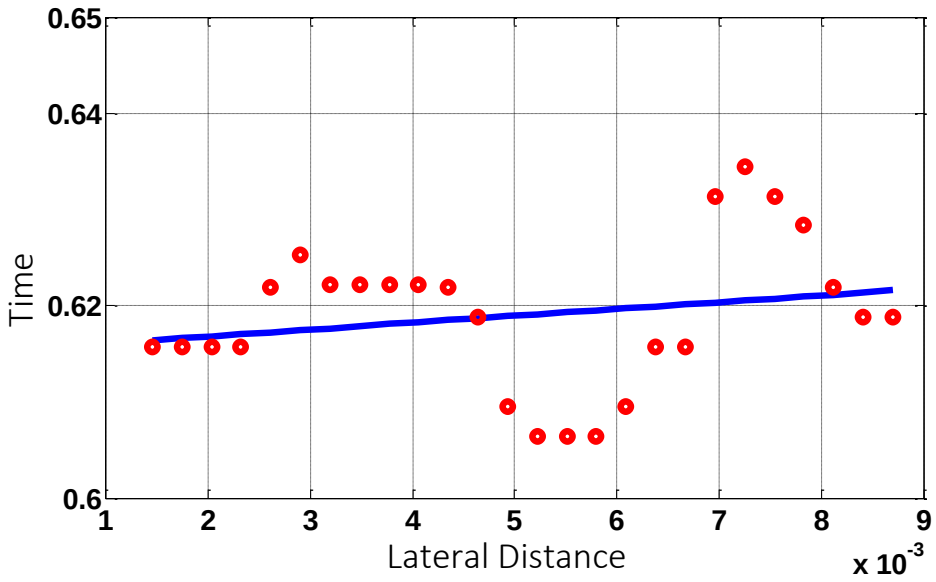

Figure (5.4.b) Linear Regression of the points along the beginning of second systole. Time vs. distance propagation of pulse wave in normal carotid artery.

PWV can be obtained from above linear regression as the inverse of slope of the line. The result from above figure is about 2.5424 m/s which is in agreement with previous results from displacement and diameter waveforms.

It should be noted that beam sweeping affects pulse wave travel time. Neglecting this delay will result underestimating travel velocity [148].

According to [148] frame rates of lower than 1000 Hz do not give accurate results for PWV measurement and frame rates above 1000 Hz don't gain much. Furthermore, the width of the probe sweeps about 1.4 cm laterally which due to large wavelength of pulse wave and speed of the wave may not be enough accurate estimation of local PWV. Therefore, the estimated value can be accounted for as a mean value. However, the above estimation shows, under suitable conditions in terms of frame rate and frame length, i.e. improved data quality, local PWV can be estimated with high accuracy.

5.3 Wall Shear Stress (WSS) and Wall Shear Rate (WSR) Measurements

In an elastic straight tube, non-pulsatile flow velocity is not the same at different points of tube cross section. Flow velocity is largest at the center of lumen and decreases as flow profile becomes closer to the walls of tube/vessel. This kind of flow behavior results a parabolic profile referred to as "laminar flow" which is mostly caused by friction forces between different layers of flow as well as between flow and vessel walls [151]. Different forces drive blood flow in body. One is the pressure gradient force and the other, gravitational forces such as friction between different layers of blood flow. Pressure difference at different points of blood vessel initiates a pressure gradient which is the

driving force of flow. In blood vessels pressure and shear force balance each other. Tangential blood force as a result of blood movement across the wall is called wall shear stress (WSS) and is a function of blood velocity gradient near the wall of vessel. Since magnitude of WSS is proportional to inverse of cubed radius of artery, a small variation in radius (diameter) can largely effect variation of WSS [152]. However, arterial mean shear stress remains constant. Previous reports have already shown the importance of WSS as a contributing factor to development of atherosclerosis [153] [154].

One way of calculating WSS requires the knowledge of diameter of vessel and pressure induced by blood flow at the walls.

$$WSS = \tau_w = {}^{a}/_{2} \cdot \frac{\partial p}{\partial x} \qquad (5.4)$$

Where "*a"* is vessel radius (assuming it remains constant throughout the cycle) and $\frac{\partial p}{\partial x}$ is rate of change of pressure per unit length of blood vessel.

Figure (5.5) shows laminar flow velocity profile in an elastic tube. One characteristic of this type of flow is parallel movement of different layers of flow. Flow tends to be minimum near the walls and maximum at the center of tube cross section.

Other method of calculating WSS involves flow velocity and blood viscosity. Although flow velocity reduces to small values at vessel walls, its resulting gradient is quite large. Gradient of flow velocity close to the walls is called wall shear rate (WSR) and is indicative of speed of deformation of flow.

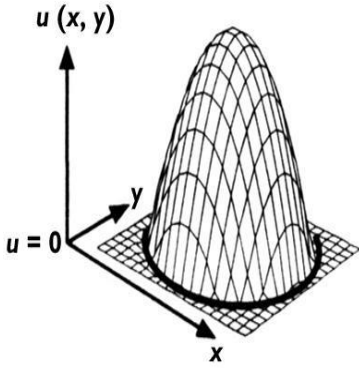

Figure (5.5): Blood velocity profile in a rigid straight vessel. Flow has a paraboloid distribution being maximum at the center of lumen and minimum close to the walls of vessel. [175] [151]

Depending on how fast the velocity changes from walls towards the center, WSR will be different.

$$WSR = \dot{\gamma} = \frac{\partial v}{\partial r} \tag{5.6}$$

where, *v* is flow velocity along the vessel axis (measured close to the wall) and *r* is radial (axial) distance.

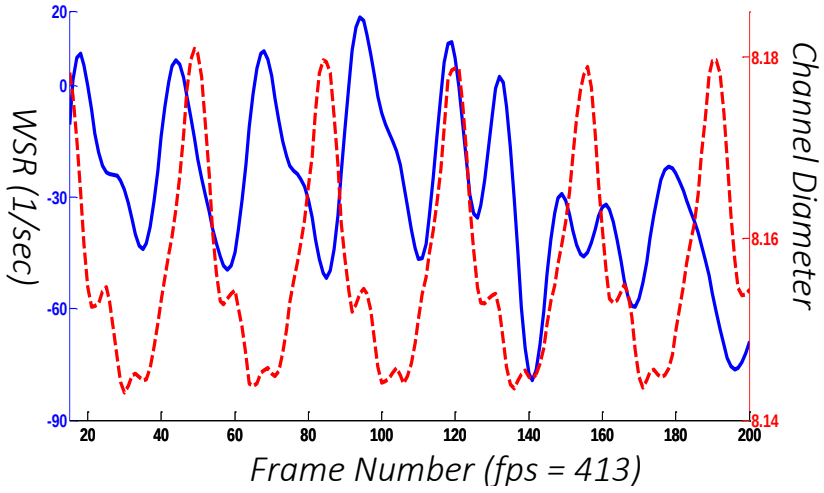

Figure (5.6): Wall Shear Rate (Red) and Channel Diameter (Blue). WSR is leading in phase compared to the change in diameter.

Based on this formula WSS can be redefined as:

$$WSS = \mu \frac{\partial v}{\partial r} = \mu \dot{\gamma} \tag{5.7}$$

where, μ is blood viscosity [155].

The flow velocity is computed by means of 2D phase coupled speckle tracking explained in [119]. The figure below shows how blood viscosity varies in two healthy subjects. In the phantom experiment linear scatterers were added to water to mimic blood and its behavior. Although the resulting flow cannot completely model blood flow behavior, its viscosity can be assumed to be close to that of blood. Based on figure (4), the viscosity of blood mimicking fluid can be assumed close to 3.540×10^{-3} (Pa.s).

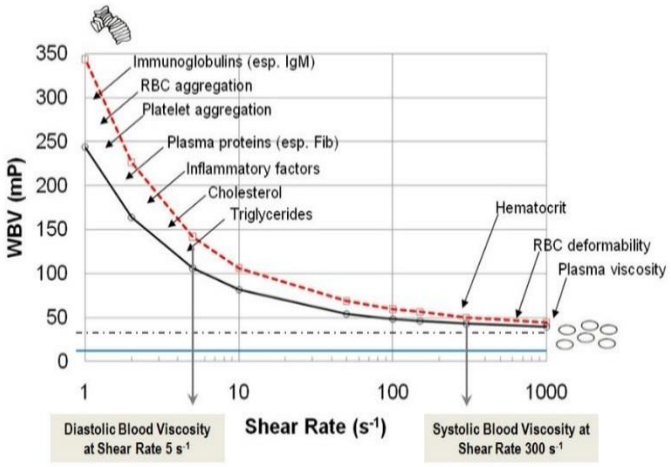

Figure (5.7): Blood viscosity curves of two healthy males at hematocrit 45. The dotted line is a constant viscosity of 35 milipoise (mp) and the blue line shows viscosity of water at 10 mp [175].

Figure (5.8.a) and (5.8.b) show WSS results from equations (5.5) and (5.7) respectively. Based on equation (5.7) WSS can be also be estimated from the flow side of channel instead of wall side. Newton's law of motion dictates that at the boundary of channel wall and blood flow, shear stress at both sides would be equal and in opposite direction to allow for blood to flow. In our simplified model, viscosity is assumed to be constant, however in more complex models it would be a function of pressure wave frequency.

In order to be able to use any of above equations, simplifying assumptions are needed. These assumptions are mainly made because soft tissue configuration is extremely complicated and heterogeneous. They allow for utilizing linear relationships regarding the material properties of tissue and blood.

- At high shear rate (sufficiently large $\dot{\gamma}$) whole blood behaves like Newtonian fluid with a constant coefficient of viscosity [156].
- Normal blood viscosity is assumed to be constant at 37°C in the range between $3x10^{-3}$ to $4x10^{-3}$ (Pa.s)
- $\tau = \mu\dot{\gamma}$,where τ is shear stress, μ is viscosity coefficient and $\dot{\gamma}$ is shear rate.

- Shear rate at the wall can be computed (with the assumption of continuity of flow).

Tissue is linear, elastic and isotropic therefore normal stress and strain can be related to each other as $\delta = E\varepsilon$ where σ is the normal stress, E is elasticity modulus (Young's modulus) and ε is normal strain. Furthermore shear stress and shear strain can be related to each other as $G = \tau/\gamma$ where γ is shear strain and G is shear modulus [157].

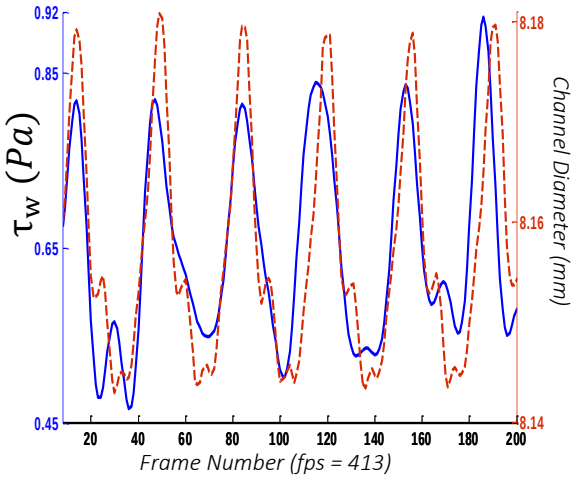

Figure (5.8a): Wall Shear Stress (Blue) and Channel Diameter (red). WSS increases as diameter (flow volume) increases and enforces more pressure on the walls of vessel. WSS is estimated using equation (5)

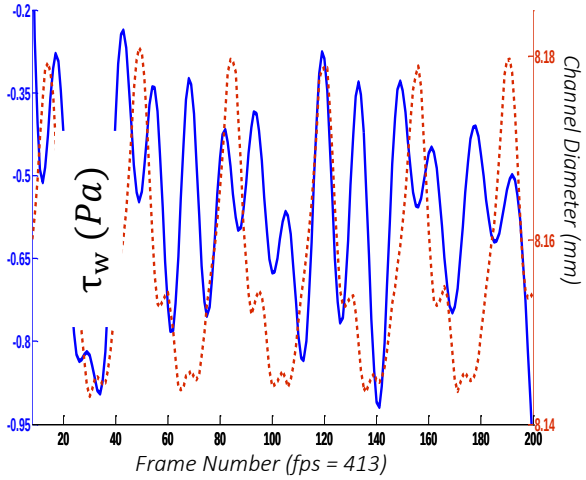

Figure (5.8b): Wall Shear Stress (Blue) and Channel Diameter (red). WSS be situated estimated using equation (7) i.e. WSR data times constant viscosity. WSS follows almost the same pattern as of Figure (1.a), however, results are smaller.

In order to discuss the validity of aforementioned assumptions, a simple schematic of longitudinal view of an elastic tube/vessel with laminar flow is shown in figure (5.9). A

differential element is selected at the boundary of flow and vessel wall and each region covers an equal height of *dh*. Second law of Newton (balance of forces) is applied to this differential element.

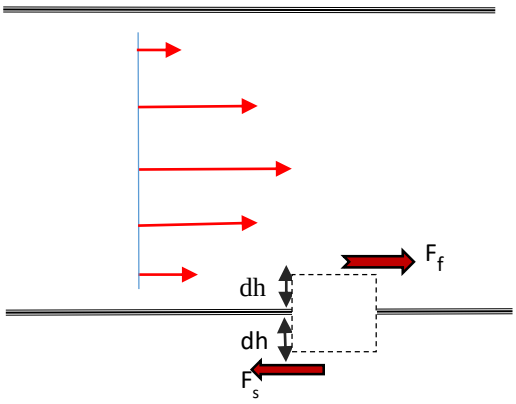

Figure (5.9): Longitudinal view of an elastic tube with laminar flow. The region of interest (ROI) is showed as dashed rectangle.

$$F_s = \tau_s . dA \qquad F_f = \tau_f . dA$$

$$\tau_s = GS_{xr} \qquad \tau_f = \mu \frac{\partial v_x}{\partial r}$$

Where τ_s and τ_f are shear stresses at the tissue and flow side of the element and dA is the area of cross section respectively. According to Newton's second law: $m \frac{d\overline{v}_{f+s}}{dt} = F_f - F_s$ (5.8) where m is the mass contained in the region of interest (ROI) and $d\overline{v}_{f+s}$ is the mean velocity of the element. Writing the above equation in more detail we will have: $\frac{d(\rho_f + \rho_s) dA dh \overline{v}}{dt} = (\tau_f - \tau_s) dA$ where ρ_f and ρ_s are flow and wall tissue density respectively.

Simplifying and rearranging the above equation we will have:

$$(\rho_f + \rho_s) \frac{d(dh\overline{v})}{dt} = (\tau_f - \tau_s)$$

Since this is a differential element $dh \rightarrow 0$ and therefore $\frac{d(dh\overline{v})}{dt} \rightarrow 0$

Eventually $\tau_f = \tau_s$ (5.9)

Therefore, shear stress at flow and tissue side must be equal in magnitude. However, according to figure (5.8) there are some discrepancies. It must be emphasized that the above conclusion is made possible by simplifying assumptions which may not be fully met in practical systems such as our experiment.

Chapter 6

Conclusion and Future Work

6.1 Conclusion

Our goal in this thesis was to introduce a new method to enable direct estimation of strain parameters on common carotid artery wall and to show the feasibility of direct estimation.

Mathematical tools governing the relations in this method were autocorrelation function, affine transformation and scaling property of Fourier transform. Analytic nature of ultrasound signals allowed for utilizing mentioned tools, i.e. to compare the autocorrelation of non-deformed and deformed windows to find normal and shear strains as elements of an affine transformation matrix.

To the best of author's knowledge, never have all four strain parameters been estimated simultaneously and without the use of spatial gradients of displacements.

The proposed method showed good accuracy and satisfactory results in both *in vitro* and *in vivo* studies, however approximation of absolute error was not possible due to lack of ground truth case.

To best our knowledge no group has yet estimated all four strain parameters. Most of studies in this field are made possible with the assumption of an ideal blood vessel, which

is elasticity, incompressibility, cylindrical orthotropicity and regional homogeneity [158]. These studies focus on radial and circumferential strains or lateral and lateral shear strains. Due to incompressibility assumption it is always assumed that shear strains in both directions (axial and lateral shear strains) are one and the same. However, wall tissue has a complicated structure and under large physiological deformations can behave differently. Therefore although this is a valid assumption for most physiological conditions of the vessel wall cannot be generalized to all strain studies [158]. Furthermore, calcifications and stenosis can change the mechanical behavior of the vessel wall and take full incompressibility under question. In our research the incompressibility assumption was relaxed therefore axial and lateral shear strains could have different values. This makes the study of vessel wall mechanical behavior more thorough. Shear values are not necessarily the same in all directions. This would also open a window to atherosclerosis studies to find out small deformations at the onset of disease.

6.2 Future Work

6.2.1 3D estimation of deformation parameters

In order to bring down the number of unknowns in the strain estimation optimization problem and to conform with imaging capabilities of clinical ultrasound machine available for this research few simplifying assumptions were made, among which limiting motion only to two dimensions. In other words, it was assumed that there is no out of plane motion of speckles. However, the random nature of speckle motion makes it quite capable of 3D motion. Due to this simplifying assumption some speckles will not be fully tracked resulting decorrelation and error in displacement and strain estimations. Having the

capability to follow deformation in all directions will lead to more accurate methods for strain estimation which in turn means more accurate diagnoses of arterial stiffness or other abnormalities at the wall of vessels.

6.2.2 Pathological Studies

The *in vivo* used for validation of our method was taken from healthy subjects. In the *in vitro* experiment also the phantom was mimicking a healthy artery without any calcifications or stenosis on the walls. Based on the accuracy of our proposed method we hypothesize that direct strain estimation method is capable of detecting pathological changes in the blood vessel wall. It is known that changes in the vessel walls start long before any clinical indications of atherosclerosis. Therefore, improving the specificity of this method to be capable to detect small changes in any strain values would be of great interest.

6.2.3 Mechanical Behavior Studies

Change of each strain parameter can be interpreted in terms of blood flow and pressure at different sections of the circulation cycle. Yet studies to fully understand relationship between strain parameters and circulation cycle have not been done. Some groups have come up with some hypotheses explaining the behavior of lateral and lateral shear strains [131] [159]. More focused studies need to be done in order to fully explain the behavior of all strain parameters.

6.2.4 Simultaneous study of wall motion and blood flow parameters

Our group among few others have measured blood flow and wall motion simultaneously [160] [161] [162] [163]. Blood flow studies due to low intensity of ultrasound images inside the lumen are more difficult than studies of wall parameters. Theoretically, knowing

all strain parameters of the wall shear rate at the flow side of the wall can be computed. Wall shear stress can also be estimated. Knowing the velocity gradients at the wall of the artery without the need to work with flow parameters can be very helpful in determining the health state of the artery in terms of atherosclerosis and stiffness.

6.2.5 Accuracy Improvement

For this study calculations were stopped as the optimum strain parameters were obtained. However, it is possible to continue the calculations using a recursive method such as a Kalman filtering to combine displacement and strain estimation. In this research in order to be able to conduct the calculations in Lagrangian coordinates displacements were estimated using 2D phase coupled speckle tracking [119] and applied to the wall prior to strain calculations. This allowed for doing all autocorrelation kernels to be centered at the new origin and eliminated the need for moving the origin of coordinates. Lack of a ground truth case study did not make it possible for us to perform an absolute error study. However, we know there are errors in the results due to data quantization, interpolation and computational limitations. Continuing the calculations further than a one-time displacement and strain estimation will substantially reduce the error. This improvement will play substantial role in study of small strain changes which occur prior to full development of atherosclerosis.

References

[1] R. VL and G. AS, "Heart disease and stroke statistics A report from the American Heart Association. Circulation 2011; 123 : e18–e209," Circulation, 2011.

[2] D. e. a. Mozaffarian, "Heart Disease and Stroke Statistics—2015 Update A report from the American Heart Association," *Circulation,* vol. 131, no. 4, pp. e29-e322, 2015.

[3] "CDC, NCHS. Underlying Cause of Death 1999-2013 on CDC WONDER Online Database, released 2015. Data are from the Multiple Cause of Death Files, 1999-2013, as compiled from data provided by the 57 vital statistics jurisdictions through the Vital Statistics," 2015. [Online]. Available: http://wonder.cdc.gov/mcd.html. [Accessed 2015].

[4] D. GA, F. M, M. M and D. SM, " (May 2008). "Stroke". Lancet 371 (9624): . doi:10.1016/S0140-6736(08)60694-7. PMID 18468545," *Stroke. Lancet 371,* p. 1612–23, 2008.

[5] "American Stroke Association," [Online]. Available: http://www.strokeassociation.org/STROKEORG/AboutStroke/TypesofStroke/Types-of-Stroke_UCM_308531_SubHomePage.jsp.

[6] Libby, Peter, P. M. Ridker and A. Maseri, "Inflammation and atherosclerosis," *Circulation,* vol. 9, no. 105, pp. 1135-1143, 2002.

[7] S. Dalager, W.P. Paaske, I.B. Kristensen, J.M. Laurberg, "Artery-related differences in atherosclerosis expression: implications for atherogenesis and dynamics in intima-media thickness," *Stroke,* vol. 38, pp. 2698-2705, 2007.

[8] J.A. Groner, M. Joshi, J.A. Bauer, "Pediatric precursors of adult cardiovascular disease: noninvasive assessment of early vascular changes in children and adolescents," *Pediatrics,* vol. 4, no. 118, pp. 1683-1691, 2006.

[9] C.M. McEniery, I.B. Wilkinson, " Age, hypertension and arterial function," *Clin Exp Pharmacol Physiol ,* vol. 34, pp. 665-671, 2007.

[10] A.M. Malek, S.L. Alper, S. Izumo, " Hemodynamic shear stress and its role in atherosclerosis," *JAMA,* vol. 282, no. 21, pp. 2035-2042, 1999.

[11] A.V. Finn, M. Nakano, J. Narula, F.D. Kolodgie, "Concept of Vulnerable/unstable plaque," *Arterioscl. Throm. Vas,* vol. 30, pp. 1282-1292, 2010.

[12] M. Naghavi and e. al., "Naghavi, Morteza, et al. "From vulnerable plaque to vulnerable patient a call for new definitions and risk assessment strategies: part I," *Circulation,* vol. 14, no. 108, pp. 1664-1672, 2003.

[13] S. Voros, S. Rinehart, Z. Qian, P. Joshi, "Coronary atherosclerosis imaging by coronary CT angiography: current status, correlation with intravascular interrogation and meta-analysis.," *JACC: Cardiovascular Imaging,* vol. 4, no. 5, pp. 537-548, 2011.

[14] H.S. Wang, Wang H, Z.P. Liu,"Agents that induce pseudo-allergic reaction".," *Drug Discov Ther,* vol. 5, no. 5, pp. 211-9, 2011.

[15] R. Safian, Manual of Interventional Cardiology 3rd, Physicians' Press, 2008.

[16] J.E. Van Velzen, J.D. Schuijf, F.R. De Graaf, "Imaging of atherosclerosis: invasive and noninvasive techniques.," *Hellenic J Cardiol ,* vol. 50, no. 4, pp. 245-263, 2009.

[17] A.A.J. de Rotte, W. Koning, M.T.B. Truijman, " Seven-tesla magnetic resonance imaging of atherosclerotic plaque in the significantly stenosed carotid artery: a feasibility study," *Investigative radiology,* vol. 49, no. 11, pp. 749-757, 2014.

[18] A. Bauer, L. Solbiati, N. Weissman, "Ultrasound imaging with SonoVue: low mechanical index real-time imaging," *Academic radiology,* vol. 2, no. 9, pp. S282-S284, 2002.

[19] S. Sokolov, " Über die praktische ausnutzung de beugnung des lichtes an ultraschällwellen.," *Phys. Z.,* vol. 36, p. 142, 1935.

[20] S. Sokolov, "Ultrasonic oscillations and their applications," *Tech. Phys. U.S.S.R.,* vol. 2, p. 522, 1935.

[21] J. M. Reid and J. J. Wild, "Ultrasonic ranging for cancer diagnosis," *Electronics,* vol. 25, pp. 136-138.

[22] J. J. Wild, J. M. Reid, " Further pilot echographic studies on the histologic structure of tumors of the living intact human breast," *The American journal of pathology,* vol. 5, no. 28, p. 839, 1952.

[23] P. Marhofer, V. W.S. Chan, Basics of ultrasound imaging. Atlas of Ultrasound-Guided Procedures in Interventional Pain Management, New York: Springer, 2011, pp. 13-19.

[24] S. Fields, F. Dunn, "Correlation of echographic visualization of tissue with biological composition and physiological state," *J. Acoust. Soc. Am.,* p. 809–811, 1972.

[25] J.V. Geleskie, K.K. Shung, "Further studies on the acoustic impedance of major bovine blood vessel walls," *J. Acoust. Soc. Am. ,* pp. 467-470, 1982.

[26] J. E. Greenleaf, Tissue Characterization with Ultrasound, Boca Raton, FL: CRC Press, 1986, pp. 1-14.

[27] "Ultrasound Image Computation," Ultrasonix, [Online]. Available: http://www.ultrasonix.com/wikisonix/index.php/Ultrasound_Image_Computation#B-Mode_Images.

[28] K. K. Shung, Diagnostic ultrasound: Imaging and blood flow measurements, CRC press, 2005.

[29] H. Azhari, Basics of biomedical ultrasound for engineers, John Wiley & Sons, 2010.

[30] R. H. Ackerman, "A perspective on noninvasive diagnosis of carotid disease," *Neurology,* vol. 5, no. 29, p. 615, 1979.

[31] R.C. Detrano, D. H. O'Leary, "Noninvasive testing for carotid artery stenosis: II. Clinical application of accuracy assessments," *American Journal of Roentgenology,* vol. 1, no. 138, pp. 109-111, 1982.

[32] S. Meairs, J. Beyer, M. Hennerici, Cerebrovascular ultrasound: theory, practice and future developments., Cambridge University Press, 2001.

[33] D.S. Babcock, H. Patriquin, M. LaFortune, M. Dauzat, "Power Doppler sonography: basic principles and clinical applications in children.," *Pediatric radiology,* vol. 26, no. 2, pp. 109-115., 1996.

[34] K.J. Murphy, J.M. Rubin, "Power Doppler: it's a good thing."," *CT and MRI Seminars in Ultrasound,,* vol. 18, no. 1, 1997.

[35] "Echo in context," [Online]. Available: http://echoincontext.mc.duke.edu/doppler01/doppler01_10.asp. [Accessed 25 06 2015].

[36] "1.8.1.1 Pulsed Wave Doppler (PW-Doppler)," Medical Uinversity of Vienna, [Online]. Available: https://123sonography.com/content/1811-pulsed-wave-doppler-pw-doppler. [Accessed 25 06 2015].

[37] JO. Arndt, J. Klauske, F. Mersch, "The diameter of the intact carotid artery in man and its change with pulse pressure.," *Pfluegers Arch ,* vol. 301, pp. 230-240, 1968.

[38] A.M. Dart, B.A. Kingwell, "Pulse pressure—a review of mechanisms and clinical relevance.," *Journal of the American College of Cardiology,* vol. 37, no. 4, pp. 975-984, 2001.

[39] DSI, [Online]. Available: http://www.datasci.com/solutions/cardiovascular/pulse-wave-velocity. [Accessed 26 06 2015].

[40] IB. Wilkinson, H. MacCallum, L. Flint, et al., "The influence of heart rate on augmentation index and central arterial pressure in humans," *Journal of Physiology,* vol. 525, no. 1, p. 263—270, 2000.

[41] S. Svedlund, "Longitudinal Common Carotid Artery wall motion Mechanistic, prognostic and translational studies," Institute of Medicine at Sahlgrenska Academy University of Gothenburg, 2011.

[42] "Carotid Intima-Media Thickness Test," Cedars-Sinai, [Online]. Available: http://cedars-sinai.edu/Patients/Programs-and-Services/Womens-Heart-Center/Services/Carotid-Intima-Media-Thickness-Test.aspx. [Accessed 26 06 2015].

[43] M. Cecelja, P. Chowienczyk, "Role of arterial stiffness in cardiovascular disease.," *JRSM cardiovascular disease,* vol. 1, no. 4, p. 11, 2012.

[44] ZR. Liu, CT. Ting, SX. Zhu, FC. Yin, "Aortic compliance in human hypertension.," *Hypertension,* vol. 14, no. 2, pp. 129-136., 1989.

[45] G. Gamble, "Estimation of arterial stiffness, compliance, and distensibility from M-mode ultrasound measurements of the common carotid artery," *Stroke,* vol. 25, no. 1, pp. 11-16, 1994.

[46] P. R. Hoskins, "Recent developments in vascular ultrasound technology.," *Ultrasound,* 2015.

[47] P. Ghaliounghi, Magic and medical science in ancient Egypt., London, UK: Hodder and Stoughton, 1963.

[48] C. Elsberg, "The edwin smith surgical papyrus and the diagnosis and treatment of injuries to the skull and spine 5000 years ago," *Ann. med. Hint.,* vol. 8, p. 271–279, 1981.

[49] P. N.T. Wells, H.D. Liang, "Medical ultrasound: imaging of soft tissue strain and elasticity," *Journal of The Royal Society Interface ,* vol. 8, no. 64, pp. 1521-1549, 2011.

[50] L. Gao, KJ. Parker, RM. Lerner, S.F. Levinson, " Imaging of the elastic properties of tissue-a review," *Ultrasound in Medicine and Biology,* vol. 22, p. 959–77, 1996.

[51] JF. Greenleaf, M. Fatemi, M. Insana, " Selected Methods for Imaging Elastic Properties of Biological Tissues," *Annual Review of Biomedical Engineering,* vol. 5, p. 57–78, 2000.

[52] J. Ophir, E. Konofagou, T. Krouskop, C. Merritt, R. Righetti, R. Souchon, S. Srinivasan and T. Varghese, "Elastography: Imaging the Elastic Properties of Soft Tissues with Ultrasound," *Medical Ultrasound,* vol. 29, p. 155–17, 2002.

[53] J. Ophir, I. Cespedes, H. Ponnekanti, Y. Yazdi and X. Li, "Elastography: a quantitative method for imaging the elasticity of biological tissues," *Ultrasonic Imaging,* vol. 13, p. 111–134, 1991.

[54] T. Varghese, J. Ophir, I. C´espedes, "Methods for estimation of subsample time delays of digitized echo signals," *Ultrasonic Imaging,* vol. 17, no. 142, 1995.

[55] J. Ophir, I. C´espedes,T. Varghese, "Noise reduction in elastograms using temporal stretching with multicompression averaging," *Ultrasound in medicine & biology,* vol. 22, no. 8, pp. 1043-1052, 1996.

[56] S. Alam and J. Ophir, "Reduction of signal decorrelation from mechanical compression of tissues by temporal stretching: Applications to elastography," *Ultrasound in Medicine & Biology,* vol. 23, no. 1, pp. 95-105, 1997.

[57] S.K. Alam, J. Ophir, E.E. Knofagou, "An adaptive strain estimator for elastography," *IEEE Trans. Ultrason. Ferroelectr. Freq.,* 1998.

[58] S. Srinivasan, F. Kallel, R. Souchon, J. Ophir, "Analysis of an adaptive strain estimation technique for elastography," *Ultrason. Imaging,* vol. 24, no. 109, 2002.

[59] T. Varghese, E.E. Konofagou, J. Ophir, SK. Alam, "Direct strain estimation in elastography using spectral cross-correlation," *Ultrasound Med. Biol,* vol. 26, pp. 1525-37, 2000.

[60] K. Hoyt, F. Forsberg, J. Ophir, "Investigation of parametric spectral estimation techniques for elasticity imaging," *Ultrasound Med. Biol.,* vol. 31, pp. 1109-21, 2005b.

[61] J. Ophir, S. Alam, B. Garra, F. Kallel, E. Konofagou, T. Krouskop and T. Varghese, "Elastography: ultrasonic estimation and imaging of the elastic properties of tissues," *Ultrasonic Imaging,* vol. 213, p. 203–33, 1999.

[62] I. Cespedes, J. Ophir, H. Ponnekanti and N. F. Maklad, "Elastography: elasticity imaging using ultrasound with application to muscle and breast in vivo," *Ultrasonic Imaging,* vol. 15, p. 73–88, 1993.

[63] M. Doyley, J. Bamber, F. Fuechsel and N. Bush, "A freehand elastographic imaging approach for clinical breast imaging: System development and performance evaluation," *Ultrasound in Medicine and Biology,* vol. 27, p. 1347–1357, 2001.

[64] Sumi, Chikayoshi, A. Suzuki and K. Nakayama, "Estimation of shear modulus distribution in soft tissue from strain distribution," *" Biomedical Engineering, IEEE Transactions on,* vol. 42, no. 2, pp. 193-202, 1995.

[65] C. Sumi, "Fine elasticity imaging utilizing the iterative RF-echo phase matching method," *Ultrasonics, Ferroelectrics, and Frequency Control, IEEE Transactions on,* vol. 46, no. 1, pp. 158-166, 1999.

[66] S Wang, WN Lee, J Provost, J Luo, "A composite high-frame rate system for clinical cardiovascular imaging," *IEEE Transactions on Ultrasonics, Ferroelectrics and Frequency Control,* vol. 55, p. 2221–2233, 2008.

[67] Lee, W. N., Ingrassia, C. M., Fung-Kee-Fung, S. D., Costa, K. D., Holmes, J. W., & Konofagou, E. E., "Theoretical Quality Assessment of

Myocardial Elastography with In Vivo Validation," *IEEE Transactions on Ultrasonics, Ferroelectrics and Frequency Control,* vol. 54, 2007.

[68] A. P. Sarvazyan, "A new approach to remote ultrasonic evaluation of viscoelastic properties of tissues for diagnostics and healing monitoring," in *Abstract of ARPA/ONR Medical Ultrasonic Imaging Technology Workshop*, Landsdowne, Virginia, 1995.

[69] K. Nightingale, "Acoustic radiation force impulse (ARFI) imaging: a review," *Current medical imaging reviews,* vol. 7, no. 4, p. 328, 2011.

[70] Hosens, [Online]. Available: http://www.myliverexam.com/en/lexamen-fibroscan.html. [Accessed 28 06 2015].

[71] N. H. Afdhal, "Fibroscan (transient elastography) for the measurement of liver fibrosis.," *Gastroenterology & hepatology,* vol. 8, no. 9, p. 605, 2012.

[72] F. j. Fernandez, W.F. Walker, " A method of imaging viscoelastic parameters with acoustic radiation force," *Phys. Med. Bio.,,* vol. 6, no. 45, pp. 1437-1447, 2000.

[73] J. H. Lumkes Jr, Control strategies for dynamic systems: design and implementation, CRC Press, 2001.

[74] Lubinski, Mark, Stanislav Y. Emelianov, and Matthew O'Donnell, "Speckle tracking methods for ultrasonic elasticity imaging using short-time correlation.," *Ultrasonics, Ferroelectrics, and Frequency Control, IEEE Transactions on,* vol. 46, no. 1, pp. 82-96., 1999.

[75] A. R. Grahn, M. H. Paul and H. U. Wessel, "A Catheter-Tip Ultrasonic Transducer for Measuring Pulsatile Aortic Diameter and Pressure Elastic Modulus," *Biomedizinische Technik/Biomedical Engineering,* vol. 19, no. 1, pp. 31-38, 1974.

[76] B.M. Shapo, J.R. Crowe, A.R. Skovoroda, "Displacement and strain imaging of coronary arteries with intraluminal ultrasound," *IEEE T. Ultrason. Ferr.,* vol. 43, pp. 234-246, 1996.

[77] APG. Hoeks, CJ. Ruissen, P. Hick, "Transcutaneous detection of relative changes in artery diameter.," *Ultrasound in medicine & biology,* vol. 11, no. 1, pp. 51-59, 1985.

[78] D. Dutta, "Non-invasive assessment of elastic modulus of arterial constructs during cell culture using ultrasound elasticity imaging.," *Ultrasound in medicine & biology,* vol. 39, no. 11, pp. 2103-2115, 2013.

[79] Couade, M., Pernot, M., Prada, C., Messas, E., Emmerich, J., Bruneval, P., ... & Tanter, *Ultrasound in medicine & biology,* vol. 36, no. 10, pp. 1662-1676, 2010.

[80] T.V. Balahonova, L.S. Hamchieva, O.A. Pogorelova, "Shear wave elastography of the common carotid artery: The first experience of application.," *Ultrasound in Medicine & Biology,* vol. 5, no. 39, p. s63, 2013.

[81] K. V. Ramnarine, "Shear wave elastography imaging of carotid plaques: feasible, reproducible and of clinical potential.," *Cardiovascular ultrasound ,* vol. 12, no. 1, p. 49, 2014.

[82] G. F. Mitchell, "Arterial stiffness and wave reflection: biomarkers of cardiovascular risk," *Artery research,* vol. 2, no. 3, pp. 56-64, 2009.

[83] R. van der Werff, S. O'Leary, G. Jull, "A Speckle Tracking Application of Ultrasound to EvaluateActivity ofMultilayered Cervical Muscles," *Journal of Rehabilitation Medicine,* vol. 46, no. 7, pp. 662-667., 2014.

[84] M. Peolsson, T. Löfstedt, S. Vogt, H. Stenlund, "Modelling human musculoskeletal functional movements using ultrasound imaging," *BMC Med Imaging,* vol. 10, no. 9, 2010.

[85] R. Seip, "Noninvasive real-time multipoint temperature control for ultrasound phased array treatments," *Ultrasonics, Ferroelectrics, and Frequency Control, IEEE Transactions on,* vol. 43, no. 6, pp. 1063-1073., 1996.

[86] C. Simon, P. VanBaren, E.S. Ebbini, "Two-dimensional temperature estimation using diagnostic ultrasound.'," *Ultrasonics, Ferroelectrics, and Frequency Control, IEEE Transactions on,* vol. 45, no. 4, pp. 1088-1099., 1998.

[87] D. Liu, E. S. Ebbini, " "Real-time 2-D temperature imaging using ultrasound.'," *Biomedical Engineering, IEEE Transactions on ,* vol. 57, no. 1, pp. 12-16, 2010.

[88] J. S. Suri, Advances in diagnostic and therapeutic ultrasound imaging., Artech House, 2008.

[89] C. B. Burckhardt, ""Speckle in ultrasound B-mode scans."," *Sonics and Ultrasonics, IEEE Transactions on,* vol. 25, no. 1, pp. 1-6, 1978.

[90] P.C. Li, a. W.N. Lee, "An efficient speckle tracking algorithm for ultrasonic imaging," *Ultrasonic imaging,* vol. 24, no. 4, pp. 215-228, 2002.

[91] J. Revell, M. Mirmehdi, D. McNally, "Combined ultrasound speckle pattern similarity measures.," *Medical Image Understanding and Analysis. ,* 2004.

[92] R. Wagner, S. Smith, J. Sandrik and H. Lopez, "Statistics of speckle in ultrasound B-scans," *IEEE Transactions on Sonics and Ultrasonics,* vol. 30, no. 3, pp. 156-163, 1983.

[93] Wells, P. NT and H.-D. Liang, "Medical ultrasound: imaging of soft tissue strain and elasticity," *Journal of The Royal Society Interface ,* vol. 8, no. 64, pp. 1521-1549, 2011.

[94] M. Jacob, "Speckle Tracking for the Recovery of Displacement and Velocity Information from Sequences of Ultrasound Images of the Tongue," in *8th International Seminar on Speech Production*, 2008.

[95] D.E. Robinson, F. Chen, L.S. Wilson, "Measurement of velocity of propogation from ultrasonic pulse-echo data, 3-D flow velocity vector estimation with a triple-beam lens transducer – experimental results," *Ultrasound Med. Biol.,* vol. 8, pp. 413-420, 1982.

[96] I. Akiyama, A. Hayama, M. Nakajima, "Movement analysis of soft tissues by speckle patterns' fluctuation," in *JSUM Proc.*, 1986.

[97] G.E. Trahey, J.W. Allison, O.T. Von Ramm, "Angle independent ultrasonic detection of blood flow," *IEEE Trans. Biomed. Eng.,* vol. 34, p. 965–967, 1987.

[98] N. Parajuli, C.B. Compas, B.A. Lin, S. Sampath, "Sparsity and Biomechanics Inspired Integration Sparsity and Biomechanics Inspired Integration Deformation Analysis," in *Functional imaging and modeling of the heart*, Springer, 2015, pp. 57-64.

[99] MJ. Ledesma-Carbayo, J. Kybic, M. Desco, "Spatio-temporal nonrigid registration for ultrasound cardiac motion estimation."," *Medical Imaging, IEEE Transactions on,* vol. 24, no. 9, pp. 1113-1126, 2005.

[100] MÁJ Ledesma-Carbayo, J. Kybic, M. Desco, "Cardiac motion analysis from ultrasound sequences using non-rigid registration.," in *Medical Image Computing and Computer-Assisted Intervention–MICCAI 2001*, Berlin Heidelberg, 2001.

[101] Woo, J., Hong, B. W., Hu, C. H., Shung, K. K., Kuo, C. C. J., & Slomka, P. J., "Non-Rigid Ultrasound Image Registration Based on Intensity and Local Phase Information," *Journal of Signal Processing Systems,* vol. 54, no. 1-3, pp. 33-43, 2009.

[102] B. Heyde, "Elastic image registration versus speckle tracking for 2-d myocardial motion estimation: A direct comparison in vivo," *Medical Imaging, IEEE Transactions on,* vol. 32, no. 2, pp. 449-459., 2013.

[103] "EchoPAC* Clinical Workstation Software," GE Healthcare, [Online]. Available: http://www3.gehealthcare.com/en/products/categories/ultrasound/vivid/echopac#tabs/tabB3B07BFEE4834E098DB49C26B4ED96C9. [Accessed 4 7 2015].

[104] "GE EchoPAC PC BT11 Software Only," Davis Medical Electronics INC., [Online]. Available: http://www.davismedical.com/Products/GE-EchoPAC-PC-BT11-Software-Only__GEN-ULT-H45561HY.aspx. [Accessed 4 7 2015].

[105] R. Seip, E. S. Ebbini, "Non-invasive Estimation of Tissue Temperature Response to Heating Fields using Diagnostic Ultrasound," *IEEE Transactions on Biomedical Engineering,* vol. 42, no. 8, pp. 828 -839, 1995.

[106] R. Seip, P. VanBaren, C. Cain, "Noninvasive Realtime Multipoint Temperature Control For Ultrasound Phased Array Treatments," *IEEE Transactions on Ultrasound, Ferroelectrics, and Frequency Control,* 1996.

[107] A. P. Hoeks, " "Non-invasive study of the local mechanical arterial characteristics in humans."," in *The arterial system in hypertension.*, Springer Netherlands, 1993, pp. 119-134.

[108] L. Capineri, M. Scabia, L. Masotti, "Vector doppler: spatial sampling analysis and presentation techniques for real time systems.," *Journal of Electronic Imaging,,* vol. 12, pp. 489-498, 2003.

[109] M. Tanter, J. Bercoff, L. Sandrin, "Ultrafast compound imaging for 2d motion vector estimation: Application to transient elastography," *IEEE Trans. Ultrason., Ferroelect., Freq. Contr.,,* vol. 49, pp. 1363-1374, 2002.

[110] L. Chen, "A quality-guided displacement tracking algorithm for ultrasonic elasticity imaging.," *Medical image analysis,* vol. 13, no. 2, pp. 286-296, 2009.

[111] J. Modersitzki, FAIR: flexible algorithms for image registration. Vol. 6. SIAM, 2009.

[112] E. S. Ebbini, "Phase-coupled two-dimensional speckle tracking algorithm," *Ultrasonics, Ferroelectrics, and Frequency Control, IEEE Transactions on ,* vol. 53, no. 5, pp. 972-990, 2006.

[113] O. Byer, F. Lazebnik, D.L. Smeltzer, "Chapter 12. Affine transformations," in *Methods for Euclidean geometry.* , MAA, 2010.

[114] "Wikipedia," [Online]. Available: http://upload.wikimedia.org/wikipedia/commons/thumb/2/23/2D_geometric_strain.svg/525px-2D_geometric_strain.svg.png.

[115] E. L. Allgower and K. Georg, Introduction to Numerical Cotinuation Methods, Colorado State University, 1990.

[116] A. F. Bower, Applied mechanics of solids, 2009: CRC press.

[117] A. V. Oppenheim and a. A. S. Willsky., Signals and systems, Prentice Hall, 1997.

[118] T. Varghesee, E.E Konofagou, "Power spectral strain estimators in elastography," *Ultrasound in Medicine & Biology,* vol. 25, no. 7, pp. 1115-1129, 1999.

[119] E. Ebbini, "Phase-coupled two-dimensional speckle tracking algorithm," *Ultrasonics, Ferroelectrics and Frequency Control, IEEE Transactions on,* vol. 53, no. 5, pp. 972-990, 2006.

[120] J. M. Sanches, A. F. Laine, J. S. Suri , Ultrasound Imaging., Springer, 2012.

[121] J. Luo and a. E. E. Konofagou, "A fast normalized cross-correlation calculation method for motion estimation," *Ultrasonics, Ferroelectrics,*

and Frequency Control, IEEE Transactions on , vol. 57, no. 6, pp. 1347-1357, 2010.

[122] R. Righetti, J. Ophir and a. P. Ktonas, "Axial resolution in elastography," *Ultrasound in medicine & biology ,* vol. 28, no. 1, pp. 101-113, 2002.

[123] "CAROTID ARTERY HEMODYNAMICS IN PATIENTS WITH ROTARY BLOOD PUMP CARDIAC ASSIST," [Online]. Available: http://www.numerik.math.tugraz.at/biomech/cfd/selected_studies/carotid.html.

[124] D. Liu and E. S. Ebbini., "Real-time 2-D temperature imaging using ultrasound," *Biomedical Engineering, IEEE Transactions on,* vol. 57, no. 1, pp. 12-16, 2010.

[125] Y. Wan, D. Liu and E. S. Ebbini., "Simultaneous imaging of tissue motion and blood flow velocity using 2d phase-coupled speckle tracking.," in *Proc. IEEE Ultrason. Symp.,*, 2010.

[126] J. H. Lumkes Jr, Control strategies for dynamic systems: design and implementation., CRC Press, 2001.

[127] Liu J., Insana M., Sridhar M., "Viscoelasticity imaging using ultrasound: parameters and error analysis," *Physics in medicine and biology ,* vol. 52, no. 9, pp. 2425-2443, 2007.

[128] I. Michael, "Insana Lab: RF Ultrasound Data Downloads," [Online]. Available: http://ultrasonics.bioen.illinois.edu/data_phantom.asp.

[129] S.C. Cowin, S.B. Doty, "Incompressible Elasticity," in *Tissue mechanics.* , Springer Science & Business Media,, 2007, p. 536.

[130] M. Sridhar, J. Liu, M.F. Insana, "Elasticity imaging of polymeric media," *Journal of biomechanical engineering,* vol. 129, no. 2, pp. 259-272, 2007.

[131] M. Cinthio, A. Ahlgren, T. J. P. H. Jonas Bergkvist and K. Lindstrom, "Longitudinal movements and resulting shear strain of the arterial

wall," *Am J Physiol Heart Circ Physiol July 2006,* vol. 291, no. 1, pp. H394-H402, 2006.

[132] E. Widman and e. al., "Ultrasound speckle tracking strain estimation of in vivo carotid artery plaque with in vitro sonomicrometry validation," *Ultrasound in medicine & biology,* vol. 41, no. 1, pp. 77-88, 2015.

[133] Cavalcante J. L., Lima J. A., Redheuil A., & Al-Mallah M. H., " Aortic stiffness: current understanding and future directions.," *Journal of the American College of Cardiology,* vol. 57, no. 14, pp. 1511-1522, 2011.

[134] S. I. Rabben, "An ultrasound-based method for determining pulse wave velocity in superficial arteries," *Journal of biomechanics ,* vol. 37, no. 10, pp. 1615-1622, 2004.

[135] Liu, C., Zhu, Q., Zheng, Y., He, Y., Xu, H., Su, J., ... & Liu, C., "Pulse Wave Velocity Measurement with Velocity Vector Imaging," in *Proceedings of the 2012 International Conference on Communication, Electronics and Automation Engineering. Springer Berlin Heidelberg*, berlin, 2013.

[136] W. W. Nichols and M. F. O'rourke, McDonald's Blood Flow in Arteries, 5th ed., New York, NY: Hodder Arnold, 2005.

[137] "DSI," [Online]. Available: http://www.datasci.com/solutions/cardiovascular/pulse-wave-velocity.

[138] O. M. Nichols WW, McDonald's blood flow in arteries. 3rd ed., London: Edward Arnold, 1990.

[139] A.P.G. Hoeks, P.J. Brands, R.S. Reneman, "Assessment of the arterial distension waveform using Doppler signal processing.," *Journal of Hypertension,* vol. 10, pp. S19-S22., 1992.

[140] X. Zhang, J. F. Greenleaf, "An anisotropic model for frequency analysis of arterial walls with the wave propagation approach.," *Applied acoustics ,* vol. 68, no. 9, pp. 953-969, 2007.

[141] H. A. Bramwell JC, "The velocity of the pulse wave in man," *Proceedings of the Royal Society of London. Series B,* vol. 93, no. 652, pp. 298-306, 1922.

[142] M. Benthin, "Calculation of pulse-wave velocity using cross correlation—effects of reflexes in the arterial tree," *Ultrasound in medicine & biology,* vol. 17, no. 5, pp. 461-469, 1991.

[143] Brands, P. J., Willigers, J. M., Ledoux, L. A., Reneman, R. S., & Hoeks, A. P., "A noninvasive method to estimate pulse wave velocity in arteries locally by means of ultrasound," *Ultrasound in medicine & biology,* vol. 24, no. 9, pp. 1325-1335, 1998.

[144] X. Zhang, J. F. Greenleaf, " Noninvasive method for estimation of complex elastic modulus of arterial vessels.," *Ultrasonics, Ferroelectrics, and Frequency Control, IEEE Transactions on,* vol. 52, no. 4, pp. 642-652., 2005.

[145] X. Zhang, J.F. Greenleaf, "Measurement of wave velocity in arterial walls with ultrasound transducers," *Ultrasound in medicine & biology,* vol. 32, no. 11, pp. 1655-1660., 2006.

[146] J. Luo, E.E. Konofagou, "A fast normalized cross-correlation calculation method for motion estimation," *Ultrasonics, Ferroelectrics, and Frequency Control, IEEE Transactions on ,* vol. 57, no. 6, pp. 1347-1357, 2010.

[147] J. Vappou, J. Luo, E.E. Konofagou, "Pulse wave imaging of the human carotid artery: an in vivo feasibility study," *Ultrasonics, Ferroelectrics, and Frequency Control, IEEE Transactions on,* vol. 59, no. 1, pp. 174-181, 2012.

[148] J. Luo, R. Li and E. Konofagou, " Pulse wave imaging of the human carotid artery: an in vivo feasibility study," *Ultrasonics, Ferroelectrics and Frequency Control, IEEE Transactions on,,* vol. 59, no. 1, pp. 174-181, 2012.

[149] J. M. Meinders, "Assessment of local pulse wave velocity in arteries using 2D distension waveforms," *Ultrasonic imaging ,* vol. 23, no. 4, pp. 199-215, 2001.

[150] E. Hermeling, "Measurement of local pulse wave velocity: effects of signal processing on precision," *Ultrasound in medicine & biology,* vol. 33, no. 5, pp. 774-781, 2007.

[151] A.M. Shaaban, A.J. Duerinckx, "Wall shear stress and early atherosclerosis: a review.," *American Journal of Roentgenology,* vol. 174, no. 6, pp. 1657-1665., 2000.

[152] G.S. Kassab, Y.C.B Fung, "The pattern of coronary arteriolar bifurcations and the uniform shear hypothesis," *Annals of biomedical engineering,* vol. 23, no. 1, pp. 13-20, 1995.

[153] CL. Asbury, JW. Ruberti, EI. Bluth, RA. Peattie, "Experimental investigation of steady flow in rigid models of abdominal aortic aneurysms," *Annals of biomedical engineering ,* vol. 23, no. 1, pp. 29-39, 1995.

[154] R. M. Nerem, " Vascular fluid mechanics, the arterial wall, and atherosclerosis.," *Journal of biomechanical engineering ,* vol. 114, no. 3, pp. 274-282, 1992.

[155] P. J. Brands, "A noninvasive method to estimate wall shear rate using ultrasound," *Ultrasound in medicine & biology,* vol. 21, no. 2, pp. 171-185, 1995.

[156] Fung. Y. C., Biomechanics: mechanical properties of living tissues, 2nd edn, New York, NY: Springer, 1993.

[157] M.L. Palmeri, M.H. Wang, J.J. Dahl, K.D. Frinkley, "Acoustic radiation force-based elasticity imaging methods.," *Interface Focus,* 2011.

[158] T.R. Canfield, P.B. Dobrin"Mechanics of blood vessels."," in *Biomedical Engineering Handbook 1*, 1995.

[159] Cinthio M., Jansson T., Persson H. W., Lindström K., & Ahlgren Å. R. "7C-2 Non-Invasive Measurements of Longitudinal Strain of the Arterial Wall.," in *Ultrasonics Symposium IEEE*, 2007.

[160] Grayson, W. L., Fröhlich, M., Yeager, K., Bhumiratana, S., Chan, M. E., Cannizzaro, C., ... & Vunjak-Novakovic, G. "Imaging vascular mechanics using ultrasound: Phantom and in vivo results.," in *Biomedical Imaging: From Nano to Macro, 2010 IEEE International Symposium on.*, 2010.

[161] H. Hasegawa, H. Kanai, "Simultaneous imaging of artery-wall strain and blood flow by high frame rate acquisition of RF signals.," *Ultrasonics, Ferroelectrics, and Frequency Control, IEEE Transactions on ,* vol. 55, no. 12, pp. 2626-2639, 2008.

[162] Nohtomi Y., asaaki Takeuchi M., Nagasawa K., Arimura K. I., Miyata K., Kuwata K., ... & Okamatsu S. "Simultaneous assessment of wall motion and coronary flow velocity in the left anterior descending coronary artery during dipyridamole stress echocardiography.," *Journal of the American Society of Echocardiography ,* vol. 16, no. 5, 2003.

[163] Lowenstein, J., Tiano, C., Marquez, G., Presti, C., & Quiroz, C. "Simultaneous analysis of wall motion and coronary flow reserve of the left anterior descending coronary artery by transthoracic Doppler echocardiography during dipyridamole stress echocardiography.," *Journal of the American Society of Echocardiography,* vol. 16, no. 6, pp. 607-613, 2003.

[164] "VASCULAR LABORATORY MARKERS OF CARDIOVASCULAR RISK," Institute for Advanced Medical Education (IAME), [Online]. Available: http://iame.com/vascular-laboratory-markers-of-cardiovascular-risk.html. [Accessed 25 06 2015].

[165] "Vascular Disease," Wallace H. Coulter Labratory, [Online]. Available: https://www.google.com/url?sa=i&rct=j&q=&esrc=s&source=images&cd=&cad=rja&uact=8&ved=0CAcQjRw&url=http%3A%2F%2Fbme.cc

ny.cuny.edu%2Ffaculty%2Fjtarbell%2F%3Fpage_id%3D39&ei=axiLVYqKKo3GogTFqYPoCA&bvm=bv.96440147,d.cGU&psig=AFQjCNGjzgMTc8xnh6jAjXhqd7-IZz4S4A. [Accessed 24 06 2015].

[166] Chenevert, Thomas L., Andrei R. Skovoroda, and Stanislav Y. Emelianov. "Elasticity reconstructive imaging via stimulated echo MRI," *Magnetic Resonance in Medicine,* vol. 39, p. 482–490, 1998.

[167] G. Sorensen, J. Jensen, J. Udesen, I. Holfort and J. Jensen, "Pulse wave velocity in the carotid artery vol., no., pp.1386-1389,," in *Ultrasonics Symposium, 2008. IUS 2008. IEEE,*, 2008.

[168] T. Shiina, "Ultrasound elastography: Development of novel technologies and standardization," *Japanese Journal of Applied Physics,* vol. 53, no. 7s, 2014.

[169] V. Sboros, M. X. Tang, "The assessment of microvascular flow and tissue perfusion using ultrasound imaging," *Proceedings of the Institution of Mechanical Engineers Part H: Journal of Engineering in Medicine ,* vol. 224, no. 2, pp. 273-290., 2010.

[170] Muthupillai, R., Lomas, D. J., Rossman, P. J., Greenleaf, J. F., Manduca, A., & Ehman, R. L. "Magnetic resonance elastography by direct visualization of propagating acoustic strain waves," *Science,* vol. 269, p. 1854–7, 1995.

[171] "QLAB - Microvascular Imaging (MVI)," Philips, [Online]. Available: http://www.healthcare.philips.com/main/products/ultrasound/technologies/qlab/vascular/qlab_mv_imaging.wpd. [Accessed 20 06 2015].

[172] C. Martinoli, F. Pretolesi, G. Crespi, S. Bianchi, "Power Doppler sonography: clinical applications.," *European journal of radiology,* vol. 27, pp. S133-S140., 1998.

[173] Y. Majdouline, J. Ohayon, Z. Keshavarz-Motamed…, "Endovascular shear strain elastography for the detection and characterization of the severity of atherosclerotic plaques: In vitro validation and in vivo

evaluation.," *Ultrasound in medicine & biology ,* vol. 40, no. 5, pp. 890-903, 2014.

[174] AM. Mahmoud, D. Dutta, L. Lavery, "Noninvasive Detection of Lipids in Atherosclerotic Plaque Using Ultrasound Thermal Strain Imaging: In Vivo Animal Study," *Journal of the American College of Cardiology,* vol. 62, no. 19, pp. 1804-1809., 2013.

[175] [Online]. Available: http://www.bloodflowonline.com/content/blood-viscosity.

[176] H. H. G. Hansdn, "Noninvasive Vascular Ultrasound Elastography Dissertation," Thesis Medical UltraSound Imaging Centre, Radboud University Nijmegen, Roermond, The Netherlands, 2012.

[177] "Fibroscan for Fatty Liver Cirrhosis and Fibrosis," MeDINDIA, [Online]. Available: http://www.medindia.net/patients/patientinfo/fibroscan-for-fatty-liver-cirrhosis-and-fibrosis.htm. [Accessed 28 06 2015].

[178] "Doppler imaging of blood flow and tissue movement," NTNU, [Online]. Available: http://www.ntnu.edu/isb/ultrasound/bloodflow. [Accessed 20 06 2015].

[179] C. Lewa and J. d. Certaines, "MR imaging of viscoelastic properties," *Journal of Magnetic Resonance Imaging,* p. 242–244, 1995.

[180] "CAROTID DUPLEX PROTOCOL," Vascular Medicine, [Online]. Available: http://www.angiologist.com/wp-content/uploads/2012/02/Vertebral-artery-duplex.jpg. [Accessed 25 06 2015].

[181] "CardioVascular Sales," Mindray Probes, [Online]. Available: http://www.cvsales.com/cvs/PartsProbes/MindrayProbes.aspx. [Accessed 25 06 2015].

[182] "BP+Education," USCOM, [Online]. Available: http://www.uscom.com.au/education/augmentation-index.html. [Accessed 26 06 205].

[183] "Advanced Applications," Toshiba, [Online]. Available: http://medical.toshiba.com/products/ul/general/aplio-platinum/imaging-technologies/advanced-applications.php. [Accessed 20 06 2015].

[184] J. J. Wild, " Application of echo-ranging techniques to the determination of structure of biological tissues.," *Classic Papers In Modern Diagnostic Radiology,* vol. 162, 2005.

[185] V. Gibbs, D. Cole, A. Sassano, "Ultrasound Physics and Technology: How, why and when," *Elsevier Health Sciences,* 2011.